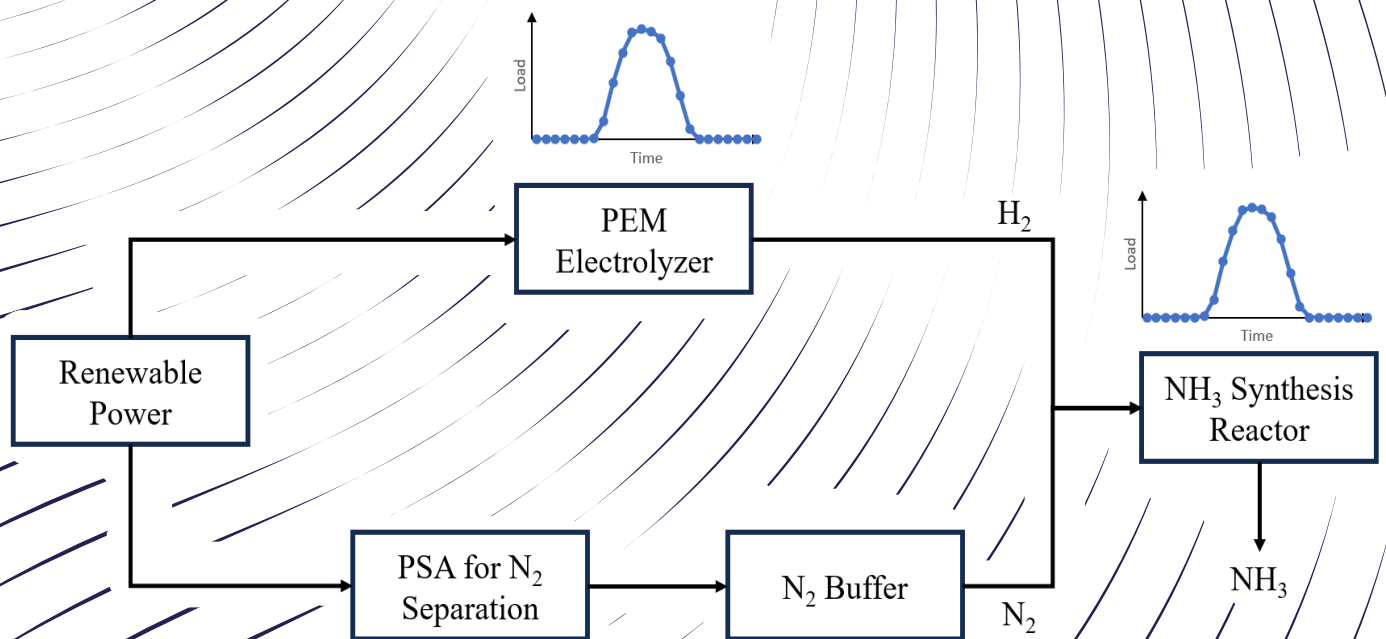


Dynamic Modelling and Control of Sorption-Enhanced Green Ammonia Synthesis Integrated with PEM Electrolysis

Elizaveta Taranets

Thermal Energy and Process Engineering, TEPE4-1007, 2025-05

Master's Thesis





AALBORG UNIVERSITY
STUDENT REPORT

AAU Energy
Aalborg University
<http://www.aau.dk>

Title:

Dynamic Modelling and Control of Sorption-Enhanced Green Ammonia Synthesis Integrated with PEM Electrolysis

Theme:

Optimisation, Analysis and Control of Thermal Energy and Processing Systems

Project Period:

Spring Semester 2025

Project Group:

TEPE4-1007

Participants:

Elizaveta Taranets

Supervisors:

Vincenzo Liso

Tianbao Gu

Number of Pages: 65

Date of Completion:

May 28th - 2025

Abstract:

With the growth of renewable energy, storing and transporting its intermittent supply remains a major challenge. The Power-to-X (PtX) concept offers a pathway by converting renewable electricity into valuable products, enabling long-term energy storage. Ammonia (NH_3), a carbon-free hydrogen carrier, has gained attention as a key product in Power-to-Ammonia (PtA) systems. Green NH_3 synthesis provides a sustainable alternative to the CO_2 -intensive Haber-Bosch process. However, conventional reactors operating at high temperature and pressure are not suited for dynamic conditions. This study addresses the challenge of adapting NH_3 synthesis process to fluctuating renewable power by investigating a novel sorption-enhanced NH_3 reactor designed for flexible operation under mild conditions. A Computational Fluid Dynamics (CFD) model of the absorption-integrated NH_3 synthesis reactor was developed. Then a steady-state Functional Mock-up Unit (FMU) using a response surface method was developed based on the CFD model data, enabling its integration with other PtA plant components in MATLAB/Simulink. The integrated model was used to explore operational feasibility and NH_3 reactor control strategies for managing fluctuating H_2 supply. Among the scenarios tested, employing two reactors operating in parallel during peak H_2 production, demonstrated the highest effective NH_3 output (33.1 kg/day) and lowest specific energy consumption (17 kWh/kg). The results demonstrate that integrating flexible, absorption-enhanced NH_3 reactors with intermittent renewable energy can be technically feasible. While the economic analysis showed the high capital cost of reactors and electrolyzers, making such systems less economically competitive.

Summary

Along with the development of renewable energy, storage and transport of the intermittent renewable energy is becoming the key challenge limiting its further advance. Power-to-X (PtX) technologies, which offer solutions to convert renewable electricity into storable fuels and chemicals, are essential for addressing the intermittency of wind and solar power. Power-to-Ammonia (PtA) offers a promising pathway, with green ammonia (NH_3), synthesised using hydrogen from water electrolysis and nitrogen from air separation, serving as a promising carbon-free hydrogen carrier. Ammonia has been produced industrially for over a century via Haber-Bosch process, supported by a well-established transport and distribution infrastructure. However, the conventional Haber-Bosch process used for ammonia synthesis is highly energy-intensive, inflexible, and reliant on fossil-derived hydrogen, making it unsuitable to dynamic renewable power inputs.

This study aims to investigate PtA systems as a sustainable alternative to conventional Haber-Bosch process, focusing on the integration challenges posed by fluctuating renewable energy and the need for novel, flexible reactor designs to enable efficient, decentralised ammonia production. More specifically, the feasibility and performance of a decentralised PtA system that integrates a highly dynamic Polymer Electrolyte Membrane (PEM) electrolyzer with a novel sorption-enhanced NH_3 synthesis reactor designed for operation under milder and flexible conditions. The work aims to assess both the operational viability and the techno-economic performance of the system, while exploring control strategies to effectively manage variable hydrogen input and maintain stable ammonia production.

The modelling approach involves developing a Computational Fluid Dynamics (CFD) model of the sorption-integrated NH_3 synthesis reactor, validated against experimental data for synthesis and absorption processes. This NH_3 reactor CFD model was then implemented for development of a steady-state Functional Mock-up Unit (FMU) using a response surface method, allowing for integration of the developed CFD NH_3 reactor model into system-level model developed in MATLAB/Simulink. Although this reactor modelling approach, does not capture full transient dynamics or sorbent saturation, a dynamic reactor response was approximated from CFD analysis. The reactor FMU was then integrated with a PEM electrolyzer model, and other plant components such as heat exchangers compressors, and buffer tanks to form the complete system model.

In order to determine the best operating point for the PtA process performance, the optimal reactor operating ranges for inlet mass flow and N_2/H_2 ratio were first determined based on CFD simulation results of the NH_3 reactor. Then these ranges were implemented for development of the NH_3 reactor control strategies. Four reactor control strategies for operating the integrated PtA system under variable renewable energy were proposed and compared, including fully dynamic and partially dynamic approaches. The strategies include: Strategy 1 - operating a single reactor across the entire hydrogen profile, Strategy 2 - operating two reactors in parallel during peak hydrogen production, Strategy 3 - operating the reactor at steady-state condition through H_2 buffering, Strategy 4 - adaptive N_2/H_2

ratio control. Among them, Strategy 2 achieved the highest daily NH_3 output (33.1 kg/day), and the lowest specific energy consumption (17 kWh/kg) compared to other control strategies.

In addition, techno-economic analysis for a system scaled to produce 300 kg/day showed that the PEM electrolyzer accounts for nearly 90% of the total system energy consumption, primarily due to the energy-intensive nature of water splitting. The absorption-integrated reactor is the largest contributor to capital costs (70-86% for most strategies), attributed to its complex construction, catalyst, and sorbent loading, and the need to scale with hydrogen production. Based on a multi-objective optimization, Strategy 2 presents the most Pareto-optimal solution minimizing Levelized Cost of Ammonia (LCOA), power consumption, and capital cost, achieving an LCOA of 1.8 €/kg.

This study demonstrates that effective control strategies are essential for enabling efficient, cost-effective green ammonia production under intermittent renewable energy supply. The proposed system shows strong potential for decentralised, carbon-neutral operation, while key challenges remain, including high capital costs, electrolysis energy demand, and the need for sorbent regeneration. The developed system-level model provides a valuable information for system optimisation and further technology development toward viable Power-to-Ammonia systems.

Preface

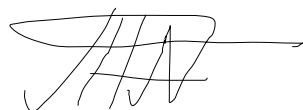
Reading Guide

The citations have been done using the IEEE method where citations will be numbered as [1] shown in the order of appearance. The citations follow their references in the bibliography located at the end of the thesis. Chapters, sections, figures, tables and equations are labeled and these will also be references when mentioned in the text. The numbering of these labels is in chronological order and chapter-wise. Throughout the report, some symbols and abbreviations may have different subscripts, however, these differences can be found in the Nomenclature.

The following software has been used in this project:

- Mathworks MATLAB
- Ansys Workbench, DesignXplorer
- Microsoft Excel
- Overleaf Latex
- Microsoft Power Point
- Engineering Equation Solver (EES)

Elizaveta Taranets
etaran23@student.aau.dk

Signature: 

The content of this report is freely available, but publication (with reference) may only be pursued due to agreement with the author.

By accepting the request from the fellow student who uploads the study group's project report in Digital Exam System, you confirm that all group members have participated in the project work, and thereby all members are collectively liable for the contents of the report. Furthermore, all group members confirm that the report does not include plagiarism.

Nomenclature

Standard SI-Units will be used

Symbol	Explanation	Unit
A	Pre-exponential factor	$\frac{\text{kmol}}{\text{m}^3 \cdot \text{h}}$
A	Area	m^2
a_j	Activity	$[-]$
C	Concentration	$\frac{\text{mol}}{\text{m}^3}$
C_2	Inertial loss coefficient	$[-]$
C_{cap}	Capital cost coefficient	$[\text{€}]$
C_p	Specific heat capacity	$\frac{\text{J}}{\text{kg} \cdot \text{K}}$
D	Diffusivity	$\frac{\text{m}^2}{\text{s}}$
d	Diameter	$[\text{m}]$
E	Total energy	$\frac{\text{J}}{\text{kg}}$
E^0	Standard potential	$[\text{V}]$
E_a	Activation energy	$\frac{\text{J}}{\text{mol}}$
$e^{(a)}$	Approximated error	$[\%]$
$e^{(ext)}$	Extrapolated error	$[\%]$
F	Faraday's constant	$\frac{\text{C}}{\text{mol}}$
f	Fugacity	$[\text{atm}]$
f_p	Pressure coefficient	$[-]$
H_{vap}	Vaporization enthalpy	$\frac{\text{J}}{\text{kg}}$
h	Cell size	$[\text{m}]$
h_j	Specific enthalpy	$\frac{\text{J}}{\text{kg}}$
I	Electrical current	$[\text{A}]$
i	Current density	$\frac{\text{A}}{\text{cm}^2}$
J_j	Diffusive flux	$\frac{\text{kg}}{\text{m}^2 \cdot \text{s}}$
K	Equilibrium constant	$[-]$
k	Rate constant	$\frac{\text{kmol}}{\text{m}^3 \cdot \text{s}}$
k_{eff}	Effective thermal conductivity	$\frac{\text{W}}{\text{m} \cdot \text{K}}$
K_{Darcy}	Membrane permeability to water	cm^2
\dot{m}	Mass flow rate	$\frac{\text{kg}}{\text{s}}$
M_i	Mass of species i	$[\text{kg}]$
M_{mem}	Equivalent weight of dry membrane	$\frac{\text{kg}}{\text{mol}}$
MW	Molecular weight	$[\frac{\text{g}}{\text{mol}}]$
N	Number of cells	$[-]$
\dot{N}	Molar flow rate	$\frac{\text{mol}}{\text{s}}$
n_d	Electro-osmotic drag coefficient	$[-]$
P	Pressure	$[\text{Pa}]$

Standard SI-Units will be used

Symbol	Explanation	Unit
p_{GCI}	Apparent order	[-]
Q	Energy	[W]
R	Universal gas constant	$\frac{\text{J}}{\text{mol}\cdot\text{K}}$
r	Refinement factor	[-]
R_{abs}	Sorption reaction rate	$\frac{\text{mol}}{\text{g}_{\text{MnCl}_2}\cdot\text{min}}$
R_{NH_3}	Synthesis reaction rate	$\frac{\text{kmol}}{\text{m}^3\cdot\text{h}}$
S	Source term	[-]
S_m	Mass source term	$\frac{\text{kg}}{\text{m}^3\cdot\text{s}}$
S_h	Energy source term	$\frac{\text{W}}{\text{m}^3}$
T	Temperature	[K]
t	Time	[s]
U	Overall heat transfer coefficient	$\frac{\text{W}}{\text{m}^2\cdot\text{K}}$
v	Velocity	$\frac{\text{m}}{\text{s}}$
V	Volume	m^3
W	Specific energy consumption	$\frac{\text{kWh}}{\text{kg}}$
w	Width of the channels	[m]
$W_{cat/sorb}$	Weight of the catalyst/sorbent material	[kg]
x_j	Mass fraction	[-]
X_a	Sorption capacity index	[-]
y_j	Mole fraction	[-]
z	Number of electrons	[-]

Greek Letters

Symbol	Explanation	Unit
α	Correction factor	[-]
α	Charge transfer coefficient	[-]
α_p	Permeability	[m ²]
Γ_ϕ	Diffusion coefficient	[-]
γ	Porosity	[-]
γ_j	Activity coefficient	[-]
η	Efficiency	[-]
λ	Membrane water content	[-]
ϵ	Void fraction	[-]
μ	Dynamic viscosity	$\frac{\text{kg}}{\text{m.s}}$
ρ	Density	$\frac{\text{kg}}{\text{m}^3}$
σ	Conductivity	[S/cm]
$\bar{\tau}$	Viscous stress tensor	[-]
τ	Time delay	[s]
ϕ	Scalar	[-]

Subscripts

Symbol	Explanation
0	Standard condition
1, 2	Index
<i>abs</i>	Absorption
<i>act</i>	Activation
<i>an</i>	Anode
<i>cat</i>	Cathode
<i>cm</i>	Coarse mesh/medium mesh
<i>cold</i>	Cold
<i>comp</i>	Compressor
<i>cons</i>	Consumed
<i>domain</i>	Domain
<i>eff</i>	Effective
<i>eq</i>	Equilibrium
<i>el</i>	Electrode
<i>ext</i>	Extrapolated
<i>f</i>	Fluid
<i>fine</i>	Fine
<i>fix</i>	Fixed
<i>gen</i>	Generation
<i>h</i>	Heat
HEX	Heat exchanger
<i>hot</i>	Hot
<i>i</i>	Index direction
<i>in</i>	Inlet
<i>j</i>	Index species
<i>m</i>	Mass
<i>max</i>	Maximum
<i>medium</i>	Medium
<i>mem</i>	Membrane
<i>mf</i>	Medium mesh/fine mesh
<i>min</i>	Minimum
<i>momentum</i>	Momentum
<i>ohm</i>	Ohmic
<i>out</i>	Outlet
<i>p</i>	Particle
<i>poly</i>	Polytropic
<i>ref</i>	Reference
<i>rxn</i>	Reaction
<i>s</i>	Solid
<i>sorbent</i>	Sorbent
<i>stack</i>	Stack
<i>total</i>	Total

Abbreviations

Abbreviation	Explanation
CASU	Cryogenic Air Separation Unit
CEPCI	Chemical Engineering Plant Cost Index
CFD	Computational Fluid Dynamics
DOE	Design Of Experiment
FCCD	Face-Centred Central Composite Design
FMI	Functional Mock-up Interface
FMU	Functional Mock-up Unit
GCI	Grid Convergence Index
GHSV	Gas Hourly Space Velocity
LCOA	Levelized Cost of Ammonia
LHV	Lower Heating Value
MA	Moist Air
MAE	Mean Absolute Error
MEA	Membrane Electrode Assembly
MOFs	Metal Organic Frameworks
NPC	Net Present Cost
PEM	Polymer Electrolyte Membrane
PID	Proportional-Integral-Derivative
PSA	Pressure swing Adsorption
PtA	Power-to-Ammonia
PtX	Power-to-X
RMSE	Root Mean Square Error
RSM	Response Surface Model
SMR	Steam Methane Reforming
SOEC	Solid Oxide Electrolyzer Cell
UDE	User Defined Expression
UDS	User Defined Scalar

Contents

1	Introduction	1
1.1	Motivation	1
1.2	Power-to-Ammonia Systems	2
1.2.1	Electrolyzer Technologies for Green Hydrogen Production	2
1.2.2	N ₂ Separation Technologies	3
1.2.3	NH ₃ Synthesis and Separation Methods	4
1.3	State of the Art	4
2	Project Objective	7
3	Methodology	8
3.1	Power-to-Ammonia Process Description	8
3.2	NH ₃ Reactor Model	8
3.2.1	Kinetic Models for NH ₃ Synthesis and Absorption	10
3.2.2	Incorporation of the Kinetic Models into CFD Framework	13
3.2.3	Functional Mock-up Interface Implementation	15
3.3	PEM Electrolyzer Model	17
3.3.1	Anode Side Model	17
3.3.2	Cathode Side Model	19
3.3.3	Membrane Model	19
3.3.4	Electrolyzer Voltage	21
3.3.5	PEM Electrolyzer Model Summary	22
3.4	Other Components of the Plant	24
3.4.1	Heat Exchangers	24
3.4.2	Compressors	24
3.4.3	Buffer Tank	25
3.5	Economic Model	25
4	Validation of the NH₃ Reactor Model	27
4.1	Validation of the NH ₃ Synthesis Process	27
4.2	Validation of the NH ₃ Sorption Process	29
5	Results and Discussion	31
5.1	Reactor Performance Analysis	31
5.1.1	Transient Reactor Operation Analysis	31
5.1.2	Reactor Dynamic Behaviour Analysis	32
5.1.3	Optimal Reactor Operating Range	33
5.2	NH ₃ Reactor Control Strategies Comparison	38
5.2.1	Effect of Control Strategies on NH ₃ Production Dynamics	38
5.2.2	Comparison of the Reactor Control Strategies	42
5.3	Techno-Economic Analysis and Optimization	44
5.3.1	System Upscaling and Resource Distribution Analysis	44
5.3.2	System Design Optimization	46
5.4	Discussion of the Feasibility of Decentralized Green NH ₃ Production	48

6 Conclusion and Future Work	52
Bibliography	54
A Meshing and GCI	60
B User Defined Expressions in Ansys Fluent	64

Chapter 1

Introduction

1.1 Motivation

Concerns over fossil fuel depletion and the urgent need to reduce greenhouse gas emissions are driving the global transition toward renewable energy sources. A global target for the energy sector is to achieve carbon-neutral energy production, with 90% of electricity generated from renewable sources by 2050 [1]. To meet this goal, a shift toward such energy carriers as hydrogen (H_2), ammonia (NH_3), and biofuels is necessary, as it will reduce the reliance on fossil fuels while promoting sustainable economic growth [2]. However, the nature of renewable energy generation is inherently variable due to its dependence on the weather conditions, which makes the continuous and reliable distribution of the generated electricity challenging [3]. Thus, to balance the gap between intermittent generation and stable demand, energy storage solutions are required. Although battery storage is a commonly applied solution for managing the fluctuations of renewable power, it has its limitations such as low energy density, limited lifespan, and high cost [4]. The Power-to-X (PtX) route offers a promising way to address these challenges by converting renewable electricity into other energy carriers ("X") such as hydrogen, ammonia, and methanol, thereby providing means for large-scale, long-term energy storage [5].

Hydrogen plays an important role in PtX systems, as it can be used directly as a fuel or further processed into other fuels or chemicals ("X") to improve storage or utilization characteristics, such as volumetric energy density [5]. However, despite its high energy content, hydrogen's extremely low boiling point ($-253\text{ }^{\circ}\text{C}$) poses significant storage and transportation challenges, necessitating either high-pressure gaseous storage or cryogenic liquid storage - both of which require expensive, specialized infrastructure [6, 7]. Consequently, alternative hydrogen carriers such as methanol, methane, and ammonia are being explored to circumvent these challenges. Among these, ammonia stands out as a particularly promising carbon-free hydrogen carrier, which offers high volumetric hydrogen content (17.6 wt%) [8, 9]. Ammonia production already plays a vital role in human development as a key component of synthetic fertilizers. Moreover, ammonia synthesis technology has been well-established for almost over a century, with already existing infrastructure for ammonia distribution and transportation, making it a less expensive option for hydrogen storage [10]. However, the majority of ammonia is currently being produced through the Haber-Bosch process, which relies on hydrogen derived from fossil methane through steam reforming [9]. Consequently, this process is one of the largest contributors to CO_2 emissions in the chemical industry, emitting 1.2% CO_2 globally [9]. In contrast, green ammonia can be produced from renewable energy sources utilizing hydrogen produced through water electrolysis, offering a more sustainable alternative with the potential for zero carbon emissions [10, 11]. However, to achieve substantial green ammonia production rates, maintaining intense operating conditions is required ($400\text{--}500\text{ }^{\circ}\text{C}$, $>100\text{ bar}$), making its integration with renewable energy sources challenging [9, 11]. This

drawback necessitates the need for investigation of novel reactor configurations that will be compatible with renewable energy sources and explore its integration into a Power-to-Ammonia system.

1.2 Power-to-Ammonia Systems

Power-to-Ammonia systems provide a path to store and convert electrical energy generated by renewable sources into ammonia, which can then be utilized either directly as a fertilizer or in other sectors such as plastics production, carbon capture, refrigeration, and pharmaceuticals [5]. The produced ammonia can also be decomposed back into hydrogen and nitrogen to produce hydrogen for use in fuel cells or used directly in direct ammonia fuel cells, providing Power-to-Ammonia-to-Power pathway [3, 12]. A typical Power-to-Ammonia (PtA) system consists of the three main units: hydrogen production via water electrolysis, nitrogen separation from air, and an ammonia synthesis reactor (Figure 1.1). Due to the intermittent nature of renewable power, all components within a PtA system must be highly dynamic and capable of rapid response, or auxiliary components such as batteries and gas buffer tanks must be added to balance demand and supply.

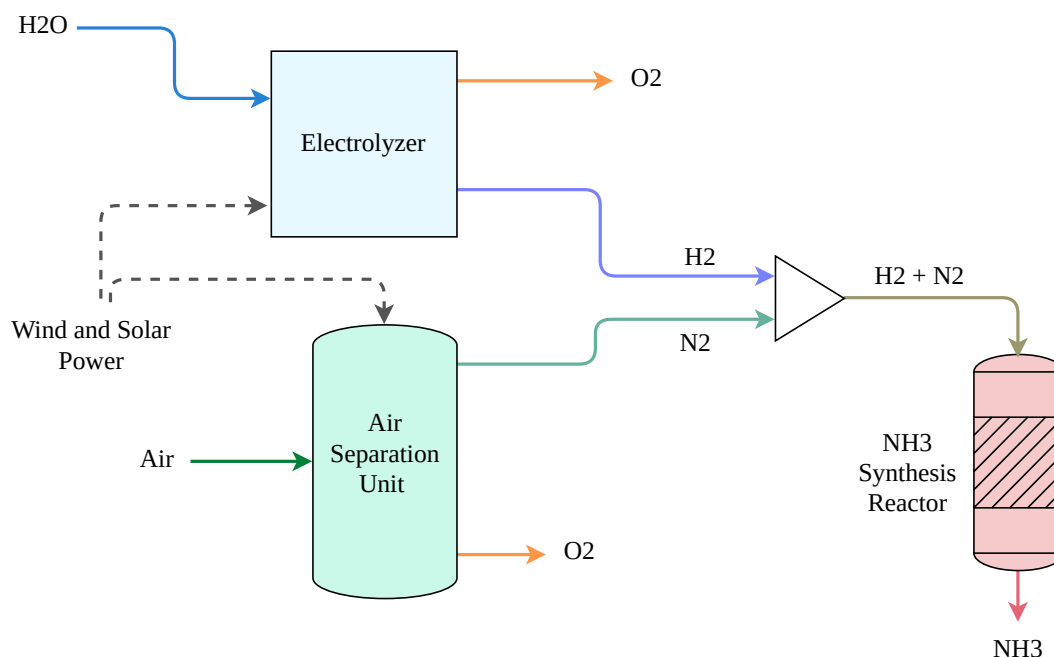


Figure 1.1: Flow sheet of the main components a Power-to-Ammonia system

1.2.1 Electrolyzer Technologies for Green Hydrogen Production

Electrolysis plays an important role in Power-to-X systems, acting as a "bridge" between Power and product (X), converting electrical energy into chemical [12]. In water electrolysis, water molecules are decomposed into hydrogen and oxygen through an electrochemical reaction driven by electrical current [13]. Several electrolyzer technologies are employed for hydrogen production, including polymer electrolyte membrane (PEM)

electrolyzers, alkaline electrolyzers, and solid oxide electrolyzers (SOEC). Alkaline electrolyzers are the most mature technology, having typically low costs due to the absence of expensive noble metals and high efficiencies (63–70%) [14]. However, this type of electrolyzers is less effective under dynamic operation and fluctuating power inputs, which are crucial for green ammonia production [15]. In contrast, PEM electrolyzers are well suited for dynamic operation due to its fast dynamic response, wide operating range, and short start-up and shut-down times [16]. Moreover, PEM electrolyzers have a compact design, making them advantageous for decentralized applications [14]. However, PEM technology requires high-purity water to avoid membrane poisoning and relies on expensive noble metal catalysts (e.g., platinum, iridium), which increases its cost relative to alkaline electrolyzers [16]. SOEC is another emerging technology that allows for reversible operation for both hydrogen production and electricity generation. They offer the highest efficiency (74-81%) compared to the other electrolyzer types [14]. Nevertheless, this comes with a trade-off requiring high operating temperatures, resulting in a complex thermal management of the system. Unlike alkaline and PEM electrolyzers, SOEC technology is still at an early stage has not yet been fully commercialized [17]. The main characteristics of above-mentioned electrolyzer types are summarized in the Table 1.1.

Table 1.1: Main Characteristics of Different Electrolyzer Types

Parameter	Alkaline	PEM	SOEC	Source
Operating Pressure, bar	1-30	30-80	1	[14]
Operating Temperature, °C	60-80	50-80	650-1000	[14, 16]
Electrical efficiency, % (LHV)	63-70	56-60	71-81	[14]
Stack Lifetime, h	60000-90000	30000-90000	10000-30000	[14, 16]
System response	Seconds	Milliseconds	Seconds	[16]
Cold start-up time, min	< 60	< 20	< 60	[16]
Development Status	Mature	Commercial	R&D	[16, 17]

1.2.2 N₂ Separation Technologies

Together with hydrogen, nitrogen is a critical reactant required for ammonia synthesis. Nitrogen is the main component of air and is abundantly available. Moreover, its production is the least energy and cost intensive process in the ammonia synthesis system [5, 18]. Nitrogen separation methods can be categorized as cryogenic and non-cryogenic [19]. Selective membrane separation is the cheapest and easiest method of N₂ production, however, this method yields relatively low gas purity and low production rates, which makes this method unsuitable for NH₃ production plants, as the presence of O₂ in the feeding gas leads to catalyst deactivation [19]. Another non-cryogenic method for N₂ extraction is pressure swing adsorption (PSA), which can operate at a wide load range and yield higher N₂ production rates and purities than membrane separation [18]. In contrast, cryogenic air separation units (CASUs) are the most efficient and cost-effective for large-scale nitrogen production, achieving nitrogen purities exceeding 99.999% [5]. Most of the cryogenic units are designed to operate under steady-state conditions due to the kinetic complexity of the process [20]. On the other hand, non-cryogenic methods offer more flexibility for dynamic operation, having a wide load range, and shorter start-up times compared to cryogenic technologies [5, 19]. The main performance characteristics of the N₂ separation methods are summarized in the Table 1.2.

Table 1.2: Main Characteristics of N₂ Separation Methods [18]

Parameter	Membrane	PSA	Cryogenic distillation
Nitrogen purity	≥ 95 wt%	≥ 99.8 wt%	≥ 99.999 wt%
Load range, %	30-100	30-100	60-100
Capacity range, Nm ³ /h	3-3000	25-800	250-50000
Power requirements, KWh/kg	-	0.11	0.119

1.2.3 NH₃ Synthesis and Separation Methods

Ammonia is synthesized through an exothermic reaction between hydrogen and nitrogen over an iron-based catalyst. Operating at 400–500 °C and pressures above 100 bar, this process is limited by thermodynamic constraints, yielding low single-pass conversions (<20%) and necessitating the recycling of unreacted gases [2]. For efficient recycling, the gas mixture must be cooled to condense and separate ammonia and then repressurized before recirculation [21]. These steps significantly contribute to the overall energy consumption of the plant and make it incompatible with renewable energy sources. Moreover, conventional ammonia synthesis reactors are designed for steady-state operation with limited flexibility, which further complicates its integration with renewable energy sources. Their start-up can take up to several days due to the strict requirements for high purity of the reactants and the need of catalyst reactivation [5, 22].

Wind- and solar-driven ammonia plants are expected to operate at a much smaller scale than the current conventional plants [23]. Moreover, an ammonia synthesis plant powered by renewable energy can be more expensive than a conventional fossil-fuel-powered plant due to differences in scale; however, this cost can be reduced by significantly lowering the operating pressure of the NH₃ reactors [24]. In its turn, reducing the pressure necessitates highly efficient separation technologies that conventional cryogenic methods cannot achieve. Recent advances in absorption technologies, particularly using solid sorbents like metal organic frameworks (MOFs), zeolites, and ionic liquids, offer a promising alternative [25, 26]. These methods offer efficient ammonia separation at lower pressures by passing the gas mixture through an absorbent bed, where ammonia is selectively captured and later released through heating and depressurization [21]. Moreover, integrating an absorption bed directly within the catalytic reactor can further enhance the yield by continuously removing ammonia and shifting the reaction equilibrium toward higher production, thereby improving overall process efficiency [27]. However, despite its advantages, sorption-based methods of NH₃ separation are currently only implemented at lab-scale plants and face significant challenges [18]. For instance, NH₃ desorption process is quite challenging due to NH₃ dissociation at high temperatures [28]. Moreover, all sorbents have finite sorption capacities and need to be regenerated frequently, which makes its control and operation of such reactors more complex.

1.3 State of the Art

Most small-scale green ammonia production models are still based on conventional Haber–Bosch reactor configurations: three-bed reactors with inter-bed cooling and ammonia condensation for separation [22, 29]. Reese et al. [23] used a steady-state model

to analyze a wind-powered, small-scale Haber–Bosch plant, identifying three key limitations: catalytic reaction rates, condensation efficiency, and unreacted gas recycling. Lower NH_3 yields at reduced temperatures and pressures for such small scale reactors highlight the need for optimization. In the study by Sun et al. [29] a dynamic model incorporating a PEM electrolyzer, PSA unit, and three-bed reactor was developed. The results showed that fast-responding units (electrolyzer and PSA) require Proportional-Integral-Derivative (PID) control strategies and buffer tanks to balance slower reactor dynamics [29]. Similarly, Fahr et al. [22] proposed a load-flexible Haber–Bosch plant model operating between 10–100% load. The study [22] showed that maintaining constant temperatures while varying pressure reduced loop mass flow by a factor of ten, resulting in uneven gas distribution and requiring advanced control strategies.

Sorption-enhanced ammonia synthesis has emerged as a promising strategy for intensifying the Haber-Bosch process under mild conditions [28]. Ammonia absorption technologies enable ammonia synthesis reactors to operate at significantly lower pressures while ensuring more effective product separation, which is particularly beneficial for integration with renewable energy sources like wind and solar [24]. Several studies have demonstrated that replacing traditional condensers with metal halides such as calcium chloride (CaCl_2), magnesium chloride (MgCl_2), and manganese chloride (MnCl_2) can significantly reduce operating pressure while maintaining high production rates [27, 30, 31]. For instance, in the study by Malmali et al. [31] it was reported that using CaCl_2 as a sorbent reduces the NH_3 reactor operating pressure by a factor of 12, compared to the conventional reactors, while sustaining high reaction rates and reducing the reverse reaction. Compared to CaCl_2 and MgCl_2 , MnCl_2 performs better at low NH_3 partial pressures and is less prone to decomposition under high temperatures [27]. Studies by Smith et al. [27] and [32] investigated the absorption kinetics of NH_3 into $\text{MnCl}_2/\text{SiO}_2$ in the layered configuration with metal based catalysts like Ru-based and Fe-based promoted with cobalt. A three-stage NH_3 absorption model into $\text{MnCl}_2/\text{SiO}_2$ was developed in [27]. It was also shown that this layered configuration allows to achieve single-pass conversions above equilibrium [27]. Even though NH_3 absorption shows promising results in small-scale laboratory applications, the modelling of absorption process is quite challenging due to complex mechanisms involved in the reaction such as chemisorption, heat and mass transfer [33].

Recent developments in sorption-integrated green ammonia synthesis processes aim to improve energy efficiency and operational flexibility, particularly for small scale production and under intermittent renewable energy supply. Rouwenhorst et al. [18] reviewed advancements in decentralized, islanded ammonia economy systems, focusing on production capacities in the 1–10 MW range. A conceptual power-to-ammonia-to-power system integrating renewable electricity, short-term battery storage, water electrolysis, PSA, and ammonia synthesis using a ruthenium-based catalyst was proposed [18]. In their system model, ammonia was separated and stored via absorption in a supported $\text{CaCl}_2/\text{SiO}_2$, and later used in a SOFC-H for electricity generation [18]. This system enables synthesis under mild conditions (275 °C, 8 bar) with an estimated energy consumption of 8.7–10.3 kWh/kg of NH_3 , while the waste heat from the SOFC is utilized for NH_3 desorption, enhancing the overall efficiency [18]. The study by Palys et al. [34] developed a dynamic model of a sorption-enhanced ammonia synthesis process powered by wind energy. The system

incorporates hydrogen from electrolysis and ammonia absorption in $\text{MgCl}_2/\text{SiO}_2$, allowing to reduce the operating pressure. The catalyst-sorbent integrated design significantly reduces capital costs, making it suitable for small-scale applications (100–10000 kg/h) [34]. Despite higher overall energy consumption, the study concluded that capital cost reductions could make the process economically viable, especially considering that electrolysis dominates the energy demand in wind-to-ammonia systems [34]. Asgharian et al. [35] developed a steady-state green ammonia production model with embedded transient sub-models to assess the technical and economic feasibility of a process incorporating an alkaline electrolyzer and MgCl_2 for the ammonia absorption. The model featured a sequence of catalyst and sorption beds, with a temperature control strategy to avoid premature equilibrium due to the drop in GHSV as ammonia is removed [35]. The results showed a 46.2% reduction in power consumption compared to conventional green Haber-Bosch processes and up to a 19% cost reduction, based on the electricity prices in Denmark in 2023 [35]. Another study by Palys et al. [36] proposed the Ammonia-Based Sustainable Energy for Agriculture (ABSEA) system, which replaces conventional batteries with hydrogen and ammonia for energy storage. A small-scale sorbent-enhanced synthesis paired with PEM electrolysis unit was designed for agricultural use in Minnesota, supplying ammonia for fertilizer, tractor fuel, and grain drying needs [36]. A combined design-scheduling optimization framework was applied to account for time-varying renewable electricity supply and fluctuating demands for ammonia and power [36]. Results showed that the integrated chemical-energy system was more economically viable than alternatives such as battery-only storage or steady-state chemical production [36].

Despite growing interest and significant advances in green ammonia production systems, several critical research gaps remain: particularly regarding the dynamic behaviour of absorption-integrated ammonia synthesis reactors operating under mild conditions and subject to highly variable power inputs from renewable sources. Current literature highlights the need for comprehensive dynamic system-level models that can capture the fluctuating operation of green ammonia plants powered by intermittent renewable energy [29, 35]. For instance, the transient behaviour of sorption-enhanced reactors and their integration with dynamic models of other system components, such as electrolyzers, remain insufficiently investigated [35]. Additionally, the flexible operation of green ammonia plants under renewable energy supply requires the development of advanced control strategies. While basic PID control can regulate certain operational parameters, more robust methods must be investigated [29]. A specific gap exists in the coupling of high-fidelity models of novel ammonia reactors with PEM electrolyzers, where system responsiveness, load-following capability, and control complexity pose new challenges. Furthermore, to the author's knowledge, no existing models couple NH_3 reactor CFD models with PEM electrolyzer model to simulate sorption-enhanced green ammonia synthesis reactors and investigate control strategies within a PtA framework. This project addresses these gaps by developing a dynamic, high-fidelity FMU-based system-level model of a Power-to-Ammonia process that integrates a novel absorption-enhanced reactor with a highly dynamic PEM electrolyzer. The model explores operational feasibility under variable renewable energy profile and assess control strategies to ensure stable and efficient green ammonia production under mild conditions. This work aims to improve understanding of the system's dynamic performance and contribute to the development of flexible, carbon-neutral ammonia synthesis technologies.

Chapter 2

Project Objective

This project aims to:

1. *Develop a dynamic, high-fidelity system-level model of a Power-to-Ammonia process;*
2. *Assess and optimize different control strategies for managing the fluctuating hydrogen supply from the electrolyzer to the ammonia synthesis reactor;*
3. *Explore the operational and economic feasibility and analyse the dynamic performance of the integrated PtA system under variable renewable energy profiles.*

Investigation Approach

The problem statement is investigated through the following steps:

1. Development of the NH_3 synthesis sorption-integrated reactor utilizing CFD framework and its implementation as an FMU-based model into MATLAB/Simulink framework;
2. Integration of the developed NH_3 reactor model into the PtA system model and analysis of the dynamic performance of the system;
3. Assessment and comparison of the proposed control strategies and evaluation of their techno-economic feasibility.

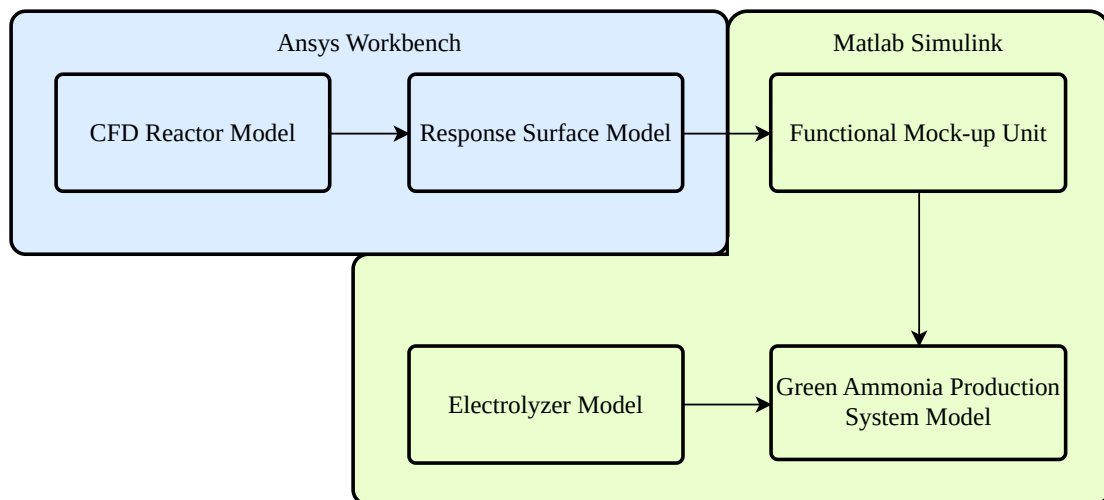


Figure 2.1: System modelling approach

Chapter 3

Methodology

This chapter describes the modelling approach including the kinetic model of NH_3 synthesis and absorption, their implementation into the CFD framework, modelling of the PEM electrolyzer, other components of the plant, and the PtA system model integrating all the components.

3.1 Power-to-Ammonia Process Description

The Power-to-Ammonia plant, designed for direct ammonia (NH_3) use as a fertilizer for agricultural needs, is illustrated in Figure 3.1. The system includes a sorption-integrated ammonia synthesis reactor, a PEM electrolyzer, and a nitrogen separation unit. Hydrogen is produced via PEM electrolysis powered by renewable energy (e.g., solar). Pure demineralized water is fed into the anode side of the electrolyzer. The PEM electrolysis subsystem consists of a water supply tank, a recirculation loop, where excess water is returned to the tank and oxygen is separated and vented, an electrolyzer stack, consisting of individual cells, a dehumidifier to remove water vapour from the produced H_2 , and a hydrogen buffer tank. Nitrogen (N_2) is produced through pressure swing adsorption (PSA) from air. Pressurized air is fed into a two-bed adsorption system operating alternately: while one bed adsorbs oxygen (O_2), the other regenerates by releasing it at lower pressure, producing high-purity nitrogen. Nitrogen separation is assumed to be 99.999% efficient. The produced N_2 is then stored in a buffer tank to balance pressure and composition fluctuations before being compressed to the reactor's operating pressure. It is assumed that there is always enough N_2 supplied to the reactor to maintain the specified N_2/H_2 ratio. Hydrogen and nitrogen are then mixed, preheated, and fed into the ammonia synthesis unit. The ammonia production subsystem consists of two reactors operating alternately: one in the NH_3 production and absorption phase, and the other in the desorption phase. Desorption is performed by increasing temperature and decreasing pressure, releasing the stored ammonia.

3.2 NH_3 Reactor Model

The proposed reactor is a multi-tubular packed bed reactor with external cooling as shown in the Figure 3.2. This design allows for better heat transfer, and more uniform flow distribution. The reactor tubes are packed with a sequence of catalyst and sorbent materials, the main geometry characteristics of the reactor are stated in the Table 3.1. To reduce the computational costs and simplify the reactor model only one layer of catalyst and sorbent in sequence was modelled through CFD as presented in the Figure 3.3. This geometry was then implemented into the CFD software ANSYS Workbench for CFD modelling, which is described in the Section 3.2.2.

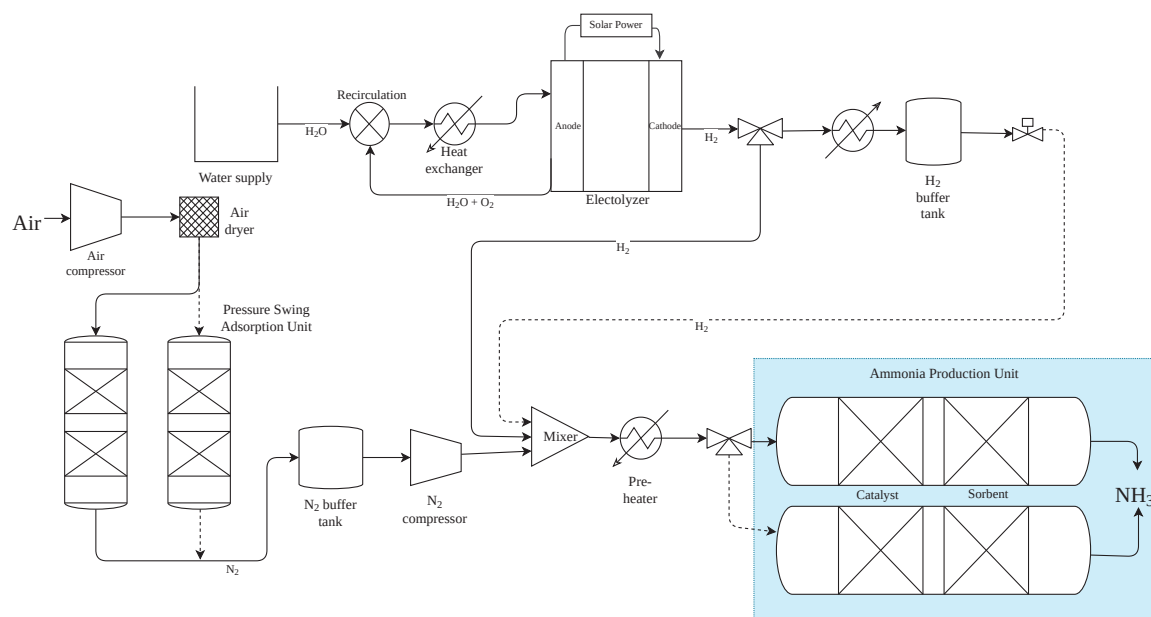


Figure 3.1: Process diagram

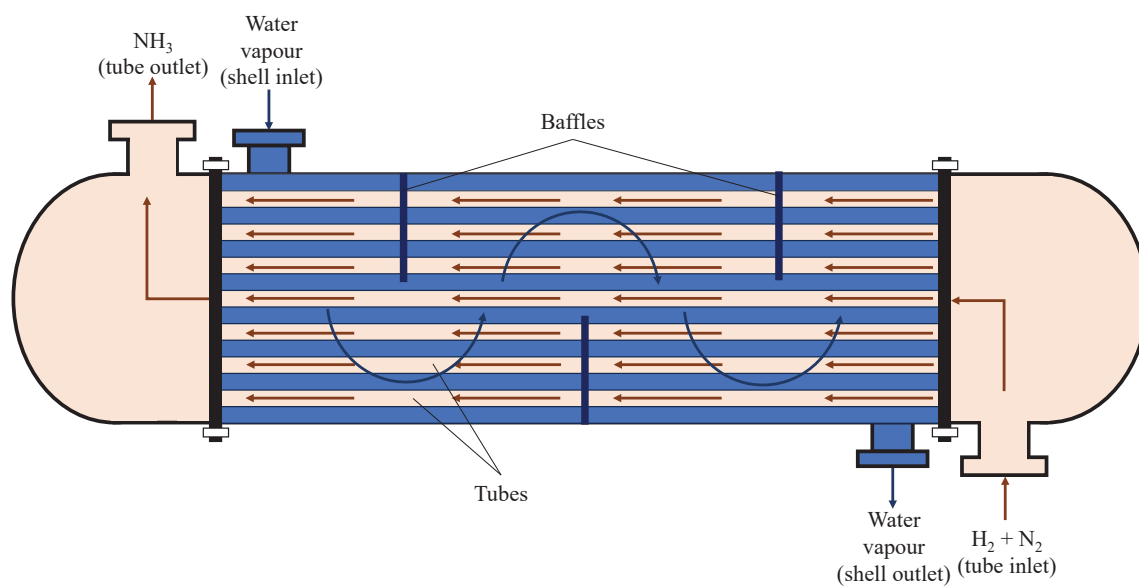


Figure 3.2: Multi-tubular packed bed reactor scheme

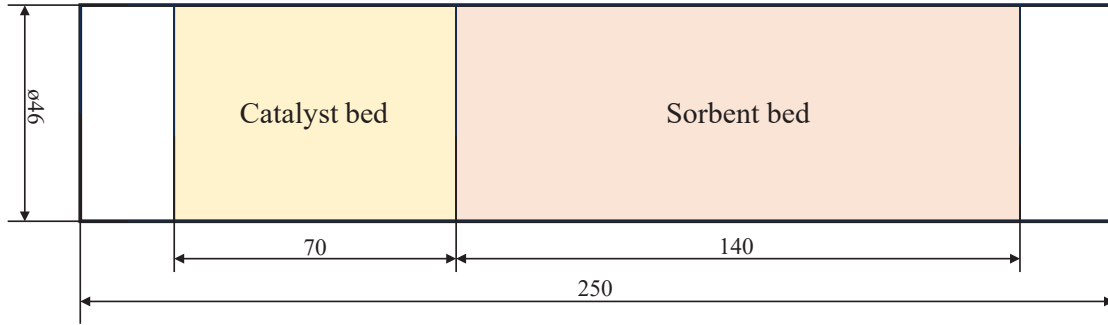


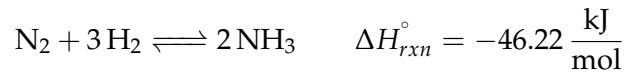
Figure 3.3: Simplified reactor geometry

Table 3.1: Reactor design parameters for the base case design

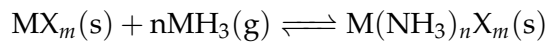
Parameter	Value	Unit
Tube diameter	0.046	m
Shell diameter	0.47	m
Number of tubes	38	-
Number of layers	14	-
Catalyst/Sorbent bed ratio	0.5	-
Total reactor length	2.52	m

3.2.1 Kinetic Models for NH₃ Synthesis and Absorption

Two chemical processes take place inside the reactor: ammonia synthesis and ammonia absorption. Global exothermic ammonia synthesis reaction is written as:



Ammonia absorption into metal halides can be generally written as:



where M is metal and X is halides.

Kinetic Model for Ammonia Synthesis

Conventionally, ammonia is synthesised over a promoted iron-based catalyst [37]. The reaction rate expression was first developed by Temkin and is determined as Equation 3.1 [38]:

$$R_{\text{NH}_3} = 2 \cdot k \cdot \left(K_a^2 \cdot a_{\text{N}_2} \cdot \left(\frac{a_{\text{H}_2}^3}{a_{\text{NH}_3}^2} \right)^\alpha - \left(\frac{a_{\text{NH}_3}^2}{a_{\text{H}_2}^3} \right)^{1-\alpha} \right) \left[\frac{\text{kmol}}{\text{m}^3 \text{h}} \right] \quad (3.1)$$

where k [kmol/(m³h)] is the rate constant, K_a is the equilibrium constant, a_j is the activity of each component and correction factor α is chosen to be 0.5 [39]. Equation 3.1 includes the assumption that nitrogen chemisorption is a rate determining step [37].

The rate constant is based on the Arrhenius Equation 3.2 [39]:

$$k = A \cdot \exp\left(-\frac{E_a}{RT}\right) \quad (3.2)$$

where $A = 8.849 \cdot 10^{14} [\text{kmol}/(\text{m}^3\text{h})]$ is pre-exponential factor, $E_a = 170560 [\text{kJ}/\text{kmol}]$ is activation energy, and $R [\text{J}/(\text{mol} \cdot \text{K})]$ is a universal gas constant.

Equilibrium constant for this reaction, applicable for a wide range of operating temperatures and pressures is written as Equation 3.3 [40]:

$$\log_{10} K_a = -2.691122 \cdot \log_{10} T - 5.519265 \cdot 10^{-5} T + 1.848863 \cdot 10^{-7} T^2 + 2001.6 T^{-1} + 2.6899 \quad (3.3)$$

The effective concentrations of the each j th species (N_2 , H_2 , NH_3) in the mixture is determined by the activity a_j 3.4:

$$a_j = \frac{f_j}{f_j^0} \quad (3.4)$$

where $f_j [\text{atm}]$ is the fugacity of each species in the solution, the reference fugacity for pure species $f_j^0 [\text{atm}]$ is assumed to be 1 atm. The fugacity of each species in the mixture is defined as 3.5:

$$f_j = x_j \cdot \gamma_j \cdot P \quad (3.5)$$

where x_j is the molar fraction for each of the species, γ_j is the activity coefficient for each of the species, P is total pressure of the gas mixture.

Activity coefficients for species N_2 , H_2 , and NH_3 in the mixture are defined as 3.6-3.8, where $T [\text{K}]$ is temperature and $P [\text{atm}]$ is pressure [39, 41].

$$\gamma_{\text{N}_2} = 0.93431737 + 0.3101804 \cdot 10^{-3} \cdot T + 0.2958961 \cdot 10^{-3} \cdot P - 0.2707279 \cdot 10^{-6} \cdot T^2 + 0.4775207 \cdot 10^{-6} \cdot P^2 \quad (3.6)$$

$$\gamma_{\text{H}_2} = \exp(e^{-3.8402 \cdot T^{0.125} + 0.541} \cdot P - e^{-0.1263 \cdot T^{0.5} - 15.980} \cdot P^2 + 300 \cdot e^{-0.0119 \cdot T - 5.941} \cdot e^{-P/300}) \quad (3.7)$$

$$\gamma_{\text{NH}_3} = 0.1438996 + 0.2028538 \cdot 10^{-2} \cdot T - 0.4487672 \cdot 10^{-3} \cdot P - 0.1142945 \cdot 10^{-5} \cdot T^2 + 0.2761216 \cdot 10^{-6} \cdot P^2 \quad (3.8)$$

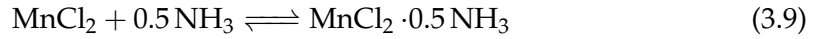
Kinetic Model for Ammonia Absorption

The next step after NH_3 synthesis is NH_3 absorption into a metal halide. Among conventionally used sorbents for NH_3 manganese(II) chloride supported on silica gel

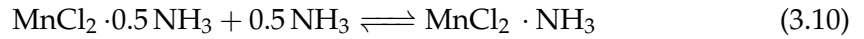
(MnCl₂/SiO₂) was chosen in this study due to its superior thermal stability and absorption capacities under the selected operating conditions.

Sorption process of NH₃ into MnCl₂/SiO₂ takes place in three steps [27]:

1. Adsorption of NH₃ on the surface of MnCl₂ - a rapid physical process occurring independently of the temperature;
2. Absorption of 0.5 molar equivalent of NH₃ (3.9);



3. Absorption of 1 molar equivalent of NH₃ (3.10).



As NH₃ sorption process is predominantly chemical interaction, reaction kinetics for all three steps is written as follows (3.11) [27]:

$$R_{abs} = R_{abs}^I + R_{abs}^{II} + R_{abs}^{III} \left[\frac{\text{mol}}{g_{\text{MnCl}_2} \text{min}} \right] \quad (3.11)$$

This reaction rate expression depends on the local partial pressures of NH₃ and is based on the stable operation of the sorbent, i.e. after first 4 cycles of operation, when the sorbent degrades rapidly [27]. Moreover, desorption process follows a different rate expression and is not accounted for by Equation 3.11. The rate of the adsorption step is described as 3.12:

$$R_{abs}^I = 3 \cdot 10^{-4} (P_{\text{NH}_3} - 0.05) (1 - X_{A1}) \left[\frac{\text{mol}}{g_{\text{MnCl}_2} \text{min}} \right] \quad (3.12)$$

where P_{NH_3} [bar] is NH₃ partial pressure, and X_{A1} is the adsorption capacity, which was experimentally found to be 13 % of a molar equivalent of MnCl₂ [27].

Reaction rates for each of the absorption steps are written as 3.13 and 3.14 respectively:

$$R_{abs}^{II} = 2 \cdot 10^{-2} (P_{\text{NH}_3} - P_{eq1})^4 (1 - X_{A2})^4 \left[\frac{\text{mol}}{g_{\text{MnCl}_2} \text{min}} \right] \quad (3.13)$$

$$R_{abs}^{III} = 2.5 \cdot 10^{-2} (P_{\text{NH}_3} - P_{eq2})^4 (1 - X_{A3})^6 \left[\frac{\text{mol}}{g_{\text{MnCl}_2} \text{min}} \right] \quad (3.14)$$

where P_{eq1} and P_{eq2} are equilibrium pressures for each of the steps, X_{A2} and X_{A3} are absorption capacities, which were experimentally determined to be 35 % of a molar equivalent of MnCl₂ for each absorption stage [27].

Equilibrium constant for the absorption stages in terms of partial pressures is expressed as 3.15 and 3.16 respectively:

$$K_1 = \frac{1}{P_{eq1}^{0.5}} \quad (3.15)$$

$$K_2 = \frac{1}{P_{eq}^{0.5}} \quad (3.16)$$

Equilibrium constants for each of the absorption stages can be also derived from Van't Hoff's equation as 3.17 and 3.18 respectively [27]:

$$\ln(K_1) = \frac{42100}{R} \left(\frac{1}{T} - \frac{1}{650} \right) \quad (3.17)$$

$$\ln(K_2) = \frac{42100}{R} \left(\frac{1}{T} - \frac{1}{610} \right) \quad (3.18)$$

3.2.2 Incorporation of the Kinetic Models into CFD Framework

The kinetics of NH_3 synthesis and absorption, described in the Section 3.2.1, are then implemented into the CFD software Ansys Fluent. To solve the CFD problem the reactor geometry (Figure 3.3) was meshed, as described in the Appendix A. The CFD model was developed previously in [42]. Assumptions made in the CFD reactor model are stated as follows:

- The mixture only consists of three species: N_2 , H_2 , NH_3 , all intermediate species are neglected [43];
- Each species is treated as ideal gas and the mixture properties are defined by ideal gas law [44];
- Only the global reaction is taken into account in the catalyst bed and no wall reactions take place [43];
- Thermal equilibrium is assumed between the solid and gas phases;
- Porosities in the catalyst and absorbent beds are fixed;
- Gravitational forces are neglected;
- The reactor is assumed to have a uniform cross-sectional area;
- Porous zones for catalyst and sorbent are assumed to be homogeneous and sorbent expansion during operation is not taken into account.

The general transport equation solved in ANSYS Fluent for porous media incorporates transient, convective, diffusive, and source terms. It is expressed using a generic scalar ϕ as shown in Equation 3.19:

$$\frac{\partial(\rho_f \phi \gamma)}{\partial t} + \nabla \cdot (\rho_f \vec{v} \phi) = \nabla \cdot (\gamma \Gamma_\phi \nabla \phi) + \gamma S_\phi \quad (3.19)$$

Here, ρ_f denotes fluid density, t represents time, \vec{v} is the fluid velocity vector, γ is the porosity, Γ_ϕ stands for the diffusion coefficient, and S_ϕ refers to the source term associated with the scalar transport [45].

For simulations with a homogeneous porous medium with uniformly distributed resistance, the momentum source term can be written as follows (Equation 3.20) [45]:

$$S_{momentum,i} = - \left(\frac{\mu_f}{\alpha_p} v_i + C_2 \cdot \frac{1}{2} \cdot \rho_f \cdot |v| \cdot v_i \right) \quad (3.20)$$

This equation takes into account both viscous and inertial resistance of the flow within the porous structure, where μ_f is the dynamic viscosity, α_p the permeability, and C_2 an inertial resistance coefficient.

In simulations involving fluid flow and heat transfer, the energy equation plays a key role in describing mechanisms such as convection, conduction, and viscous heating. For this model, it is used to account for the thermal transport occurring within the reactor. It is assumed that the solid and fluid phases within the porous region are in thermal equilibrium, and the energy balance to be written as in Equation 3.21 [45]:

$$\frac{\partial}{\partial t} (\gamma \rho_f E_f + (1 - \gamma) \rho_s E_s) + \nabla \cdot (\vec{v} (\rho_f E_f + p)) = \nabla \cdot (k_{eff} \nabla T - \sum_j h_j J_j + \bar{\tau} \vec{v}) + S_f^h \quad (3.21)$$

In this equation, E_f and E_s are the total energies of the fluid and solid phases respectively, S_f^h represents a volumetric heat source term, k_{eff} is the effective thermal conductivity, h_j is the specific enthalpy of species j , J_j is the diffusive flux of species, and $\bar{\tau}_{eff}$ is the viscous stress tensor.

The catalyst and sorbent beds are modelled as porous zones. The reaction kinetics are implemented as mass source terms for NH_3 synthesis and absorption for each respective part in the geometry. As both of the processes are exothermic, heat generation by the reactions is implemented in the energy source term. The source terms are specified as User-Defined Expressions (UDE) in Ansys Fluent (Appendix B) [46].

Accurate boundary conditions and solution strategies are key for reliable CFD results. At the inlet velocity, temperature, and species mole fractions are specified. An outflow condition is set at the outlet, allowing internal flow to determine the pressure field. The reactor walls have fixed temperature, equal to the inlet temperature. A transient laminar flow model is used to capture time-dependent behaviour. Pressure-velocity coupling is solved with the Coupled Algorithm for enhanced stability and convergence. Second-order upwind schemes are applied for spatial discretization of momentum, energy, and species equations. This approach balances accuracy and computational efficiency by using up-stream values and accounting for flow direction [47]. For time integration, a second-order implicit scheme is used. It is unconditionally stable and well-suited for stiff problems, where flow and reaction timescales differ significantly [47]. The scheme improves accuracy and avoids instability from large time-steps [47]. The summary of implemented CFD boundary conditions and solution methods is stated in the Table 3.2.

Table 3.2: Summary of CFD Methods

Settings	Description
Models	Transient laminar flow model
Boundary conditions	Velocity inlet Outflow outlet Zero-slip fixed temperature wall condition
Solution Algorithm	Coupled Algorithm
Spatial Discretization Scheme	2nd order Upwind
Temporal Discretization Scheme	2nd order Implicit
Solver	Anslys Fluent 2024 R2

3.2.3 Functional Mock-up Interface Implementation

To integrate the reactor model developed in ANSYS Workbench with the electrolyzer model built in MATLAB/Simulink, a coupling interface is required. The Functional Mock-up Interface (FMI) is a standard that enables data exchange and co-simulation between different software environments that support it [48]. In this work, FMI for Model Exchange is used. FMI for Model Exchange only includes the model algorithm and does not provide a numerical solver [48]. In this approach, the ODE solver must be provided by the importing software, and the FMI is evaluated at specific time points rather than continuously. The reactor model was developed in ANSYS Workbench, and the solution was obtained using the ANSYS Fluent solver. According to the FMI standard, ANSYS Fluent only supports FMI for Co-Simulation (import only), meaning it can import external models into its environment but does not allow exporting Fluent models for use in other software [48]. However, ANSYS Workbench's System Coupling DesignXplorer allows for model export using FMI for Model Exchange, based on a response surface model (RSM) [45].

To implement the CFD-based reactor model into MATLAB/Simulink, a response surface model was developed. Prior to development of a highly accurate response surface model, design of experiments (DoE) approach was used to determine the number of points, that involve the different combinations of the input parameters, to balance the accuracy and minimize the number of simulation runs. This involves running the Fluent simulation across a predefined range of input parameters and recording the output variables. From this dataset, a continuous mathematical relationship (response surface) is built between the inputs and outputs. This model does not capture time-dependent behaviour, only accounting for the outputs at the last time point of the simulation. However, there is a steady operation stage of the NH_3 synthesis-absorption reactor, outputting time-independent NH_3 production rate. The response surface defines a continuous function and enables fast computation within the parameter space it was trained on. The accuracy and computational efficiency of this exported model strongly depend on the DoE method used and the type of response surface chosen.

To develop the response surface, key input parameters that define the reactor's operational range were identified. A Face-Centred Central Composite Design (FCCD) scheme was selected for the DoE. This method ensures good coverage of the design space while minimizing the number of required simulations. Five input variables (mass flow, H_2 and

NH₃ mole fractions, temperature, pressure) and eight output variables (H₂ conversion, H₂ and NH₃ mass fractions, effective NH₃ production, NH₃ absorbed fraction, total mixture outlet mass flow, outlet temperature, pressure drop) were considered (Figure 3.4). A genetic aggregation method was applied for model fitting, as this method provides more accurate fitting for complex input-output relationships. While more advanced models such as neural networks or sparse grids could provide more accurate results, they were not used, as they cannot be exported as an FMU [45]. The main limitation of this approach is that the resulting FMU model assumes steady-state behaviour and does not account for the transient dynamics or sorbent saturation. Moreover, this model is only valid within the parameter range used for training and may not produce accurate results outside this range.

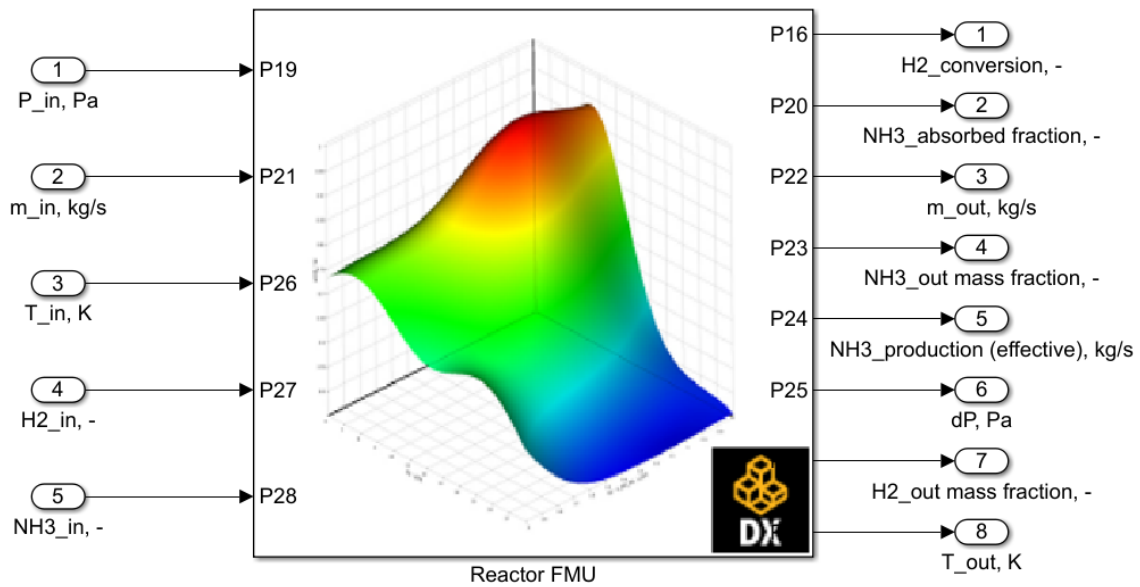


Figure 3.4: Reactor FMU model in MATLAB/Simulink environment

As the FMU model is based on the response surface fittings, the accuracy of the model needs to be evaluated. If the model is poorly fitted the results produced by such model can be not physically accurate. The quality of the fitted model can be evaluated by the two main statistical parameters: coefficient of determination (R^2) and root mean square error (RMSE), which are presented in the Table 3.3. A large difference in R^2 and RMSE for learning points and cross-validation points indicates overfitting. Figure 3.5 compares the values observed from the CFD simulation and the values predicted by the response surface model for each of the output parameters. It can be observed that all of the points lie closely to the perfect prediction line, which indicates that the response surface accurately predicts the output parameters with minor deviations from the values obtained from the CFD model.

Table 3.3: Goodness of fit

Variable	R^2		RMSE	
	Learning Points	Cross-Validation	Learning Points	Cross-Validation
H ₂ conversion	1	0.852	$6.8 \cdot 10^{-6}$	0.018
NH ₃ absorbed fraction	1	0.995	$9.8 \cdot 10^{-8}$	0.023
m_{out}	1	1	$1.18 \cdot 10^{-12}$	$5.98 \cdot 10^{-8}$
NH ₃ mass fraction	1	0.987	$5.45 \cdot 10^{-8}$	0.0012
NH ₃ production	1	0.971	$5.05 \cdot 10^{-11}$	$5.9 \cdot 10^{-8}$
dP	1	0.999	0.00083	0.017
H ₂ mass fraction	0.999	0.996	0.001	0.003
T_{out}	0.999	0.999	0.038	0.253

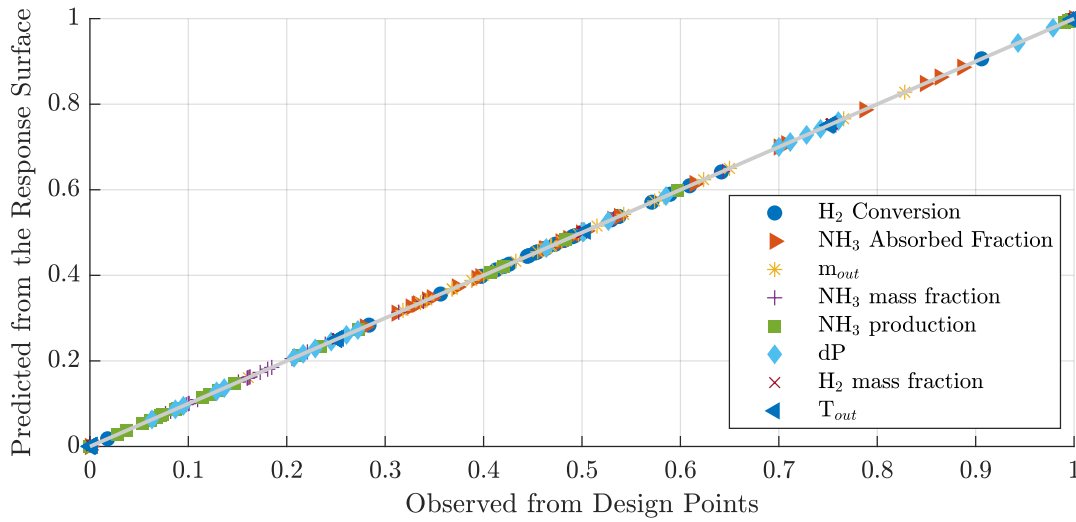
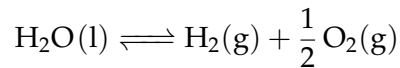


Figure 3.5: FMU fitting parameters for the reactor model

3.3 PEM Electrolyzer Model

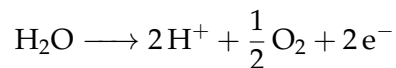
In the PtA system hydrogen, required for NH₃ synthesis reaction, is produced by water electrolysis. Water electrolysis involves an electrochemical reaction where water is split into H₂ and O₂ under the electrical current. Overall water electrolysis reaction:



The implemented electrolyzer model is based on the model developed in [49]. The schematic view of the electrolyzer cell is presented on the Figure 3.6.

3.3.1 Anode Side Model

On the anode side of the electrolyzer water is oxidized, releasing electrons and the reaction taking place is:



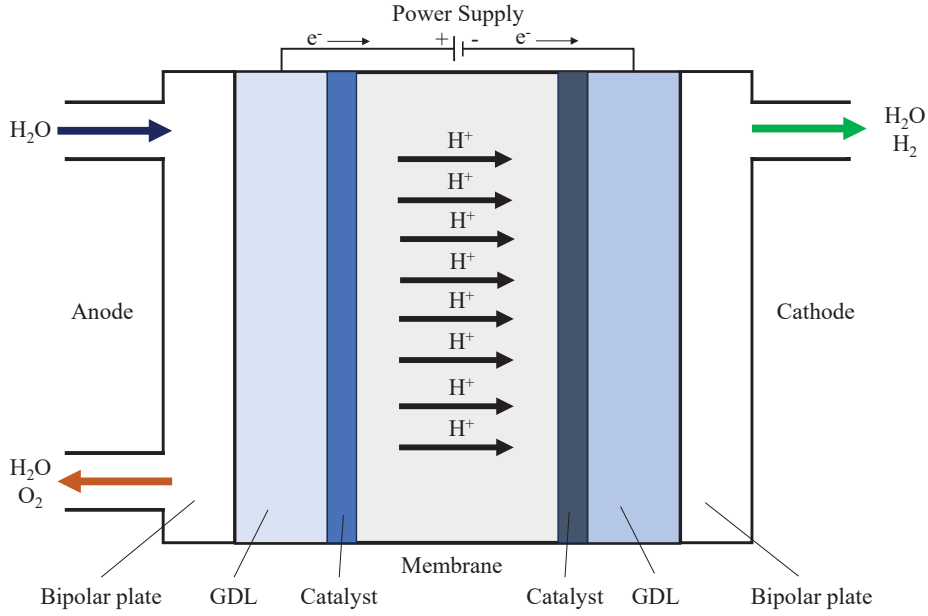


Figure 3.6: PEM electrolyzer: schematic view (inspired by [13])

Due to the electrochemical reaction occurring at the anode, four moles of O_2 are produced for every four electrons transferred. Therefore, molar flow rate of O_2 according to the Faraday's law is written as Equation 3.22 [13]:

$$\dot{N}_{an,O_2}^{gen} = \frac{I}{4F} \left[\frac{mol}{s} \right] \quad (3.22)$$

where $I[A]$ is the current, $F[C/mol]$ is Faraday's constant.

In the anode reaction, two moles of water are consumed for each electron, and the molar flow rate of the H_2O consumed in the reaction is described as Equation 3.23 [13]:

$$\dot{N}_{an,H_2O}^{cons} = \frac{I}{2F} \left[\frac{mol}{s} \right] \quad (3.23)$$

Mole balance of O_2 accumulation at the anode side can be written as Equation 3.24 [13]:

$$\frac{dN_{an,O_2}}{dt} = \dot{N}_{an,O_2}^{in} - \dot{N}_{an,H_2O,l}^{out} + \dot{N}_{an,O_2}^{gen} \left[\frac{mol}{s} \right] \quad (3.24)$$

where anode inlet molar flow rate of O_2 is $\dot{N}_{an,O_2}^{in} = 0 [mol/s]$, and $\dot{N}_{an,H_2O,l}^{out} [mol/s]$ is the molar flow rate of unconsumed H_2O .

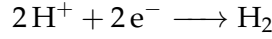
Water accumulation on the anode side, taking the H_2O flow through the membrane into account, can be expressed as Equation 3.25 [13]:

$$\frac{dN_{an,H_2O}}{dt} = \dot{N}_{an,H_2O}^{in} - \dot{N}_{an,H_2O,l}^{out} - \dot{N}_{an,H_2O}^{cons} - \dot{N}_{H_2O}^{mem} \left[\frac{mol}{s} \right] \quad (3.25)$$

where $\dot{N}_{an,H_2O}^{in} [mol/s]$ is the molar flow rate of H_2O supplied to the anode, and $\dot{N}_{H_2O}^{mem} [mol/s]$ is the molar flow rate of H_2O through the membrane.

3.3.2 Cathode Side Model

Hydrogen is generated on the cathode side through the reduction reaction:



Hydrogen production on the cathode side, according to the Faraday's law, is expressed as 3.26 [13]:

$$\dot{N}_{H_2}^{gen} = \frac{I}{2F} \left[\frac{mol}{s} \right] \quad (3.26)$$

Then, H_2 accumulation in the electrolyzer, according to the mole balance on the cathode, is written as Equation 3.27 [13]:

$$\frac{dN_{H_2}}{dt} = \dot{N}_{H_2}^{in} - \dot{N}_{H_2}^{out} + \dot{N}_{H_2}^{gen} \left[\frac{mol}{s} \right] \quad (3.27)$$

where inlet H_2 molar flow rate $\dot{N}_{H_2}^{in} = 0 [mol/s]$, and molar flow rate of H_2 at the outlet $\dot{N}_{H_2}^{out} = \dot{N}_{H_2}^{gen} [mol/s]$.

As some of the H_2O is transferred through the membrane to the cathode side, mole balance of the H_2O accumulation is expressed as Equation 3.28 [13]:

$$\frac{dN_{cat,H_2O}}{dt} = \dot{N}_{H_2O}^{in} - \dot{N}_{H_2O}^{out} + \dot{N}_{H_2O}^{mem} \left[\frac{mol}{s} \right] \quad (3.28)$$

where $\dot{N}_{H_2O}^{in} [mol/s]$ is the molar flow rate of H_2O at the inlet, $\dot{N}_{H_2O}^{out} [mol/s]$ is the molar flow rate of H_2O at the cathode outlet, $\dot{N}_{H_2O}^{mem} [mol/s]$ is the molar flow rate of H_2O transferred through the membrane.

3.3.3 Membrane Model

The membrane electrode assembly (MEA) is modelled as custom Simscape block, interfaced with a thermal liquid network for water supply and two moist air networks for hydrogen and oxygen flows [49].

The net water flow, passing through the membrane is influenced by three phenomena: diffusion, electro-osmotic drag and hydraulic pressure [13]. Then, the molar balance of the water flow through membrane is expressed as Equation 3.29 [13]:

$$\dot{N}_{H_2O}^{mem} = \dot{N}_{H_2O}^{diff} + \dot{N}_{H_2O}^{eod} - \dot{N}_{H_2O}^{pe} \quad (3.29)$$

where $\dot{N}_{H_2O}^{diff} [mol/s]$ is the molar flow rate of H_2O due to diffusion, $\dot{N}_{H_2O}^{eod} [mol/s]$ is the molar flow rate of H_2O due to electro-osmotic drag, and $\dot{N}_{H_2O}^{pe} [mol/s]$ is the molar flow rate of H_2O due to hydraulic pressure. The diffusion mechanism involves water transport

driven by concentration gradients across the membrane [13]. In contrast, electro-osmotic drag occurs when water molecules are carried along by hydrogen protons [13]. Additionally, hydraulic pressure differences between the anode and cathode also drive water movement through the membrane [13].

Molar flow rate of H_2O through the membrane due to diffusion, assuming linear water concentration gradient, can be written as Equation 3.30 [13]:

$$\dot{N}_{H_2O}^{diff} = \frac{A_{cell} D_{H_2O,mem}}{\delta_{mem}} (C_{H_2O,mem,an} - C_{H_2O,mem,cat}) \left[\frac{mol}{s} \right] \quad (3.30)$$

where A_{cell} [m^2] is the active area of the cell, $D_{H_2O,mem}$ [m^2/s] is the water diffusion coefficient, δ_{mem} [m] is the membrane thickness.

Water diffusion coefficient $D_{H_2O,mem}$ can be described as a function of stack temperature (T_{stack} [K]) (Equation 3.31) [49]

$$D_{H_2O,mem} = 1.25 \cdot 10^{-10} \cdot \exp \left(2416 \left(\frac{1}{303.15} - \frac{1}{T_{stack}} \right) \right) \left[\frac{m^2}{s} \right] \quad (3.31)$$

Water concentrations of the electrolyte-electrode interfaces for anode ($C_{H_2O,mem,an}$) and cathode $C_{H_2O,mem,cat}$ sides are expressed as Equation 3.32 and Equation 3.33 respectively [49].

$$C_{H_2O,mem,an} = \frac{\rho_{mem}}{M_{mem}} \cdot \lambda_{an} \left[\frac{mol}{L} \right] \quad (3.32)$$

$$C_{H_2O,mem,cat} = \frac{\rho_{mem}}{M_{mem}} \cdot \lambda_{cat} \left[\frac{mol}{L} \right] \quad (3.33)$$

Here $\rho_{mem} = 2000$ [kg/m^3] is density of the dry membrane, $M_{mem} = 1.1$ [kg/mol] is the equivalent weight of the dry membrane, λ is the water content in the membrane [49].

The water content in the membrane can be described Equation 3.34 [50]:

$$\lambda(a) = \begin{cases} 0.043 + 17.81a, & \text{if } a < 0 \\ 0.043 + 17.81a - 39.85a^2 + 36a^3, & \text{if } 0 \leq a \leq 1 \\ 14.003 + 1.4(a - 1), & \text{if } a > 1 \end{cases} \quad (3.34)$$

where a represents the activity of the species (H_2O).

Electro-osmotic drag refers to the amount of water moved with each mole of hydrogen ions through the membrane. The molar flow rate of H_2O due to electro-osmotic drag is written as Equation 3.35 [13]:

$$\dot{N}_{eod} = \frac{n_{d,H_2O} I}{F} \left[\frac{mol}{s} \right] \quad (3.35)$$

Where electro-osmotic drag coefficient n_{d,H_2O} is described as Equation 3.36 [50]:

$$n_{d,H_2O} = \begin{cases} 0.0029\lambda^2 + 0.05\lambda - 3.4 \cdot 10^{-19}, & \lambda \geq 0 \\ 0.05\lambda - 3.4 \cdot 10^{-19}, & \lambda < 0 \end{cases} \quad (3.36)$$

The molar flow rate of water due to the pressure difference between anode and cathode is written as Equation 3.37 [49]:

$$\dot{N}_{H_2O}^{pe} = \begin{cases} A_{cell} \frac{(p_{an} - p_{cat}) \cdot K_{Darcy} \cdot p_{an} \cdot y_{H_2O,an}}{RT_{stack} \mu_{H_2O} \sigma_{mem}} \left[\frac{mol}{s} \right], & \text{if } p_{an} > p_{cat} \\ A_{cell} \frac{(p_{an} - p_{cat}) \cdot K_{Darcy} \cdot p_{cat} \cdot y_{H_2O,cat}}{RT_{stack} \mu_{H_2O} \sigma_{mem}} \left[\frac{mol}{s} \right] \end{cases} \quad (3.37)$$

where p_{an} [Pa] and p_{cat} [Pa] are anode and cathode pressures, $K_{Darcy} = 1.58 \cdot 10^{-14}$ [cm²] is membrane permeability to water, $y_{H_2O,an}$ and $y_{H_2O,cat}$ are water vapour mole fractions at the anode and cathode catalyst layers respectively, and μ_{H_2O} [Pa · s] is the dynamic viscosity of water [49].

3.3.4 Electrolyzer Voltage

Electrolyzer voltage consists of the open circuit voltage (V_{oc}), activation overpotential (V_{act}), ohmic overpotential (V_{ohm}), and concentration overpotential (V_{conc}) [13]:

$$V = V_{oc} + V_{act} + V_{ohm} + V_{conc} \quad [V] \quad (3.38)$$

Open circuit voltage can be described by the Nernst equation in terms of partial pressures (Equation 3.39) [13]:

$$V_{oc} = E^0 + \frac{RT_{stack}}{zF} \ln \left(\frac{p_{H_2}}{p_{cat}} \sqrt{\frac{p_{O_2}}{p_{an}}} \right) \quad [V] \quad (3.39)$$

where $z = 2$ is the number of transferred electrons, p_{H_2} [Pa] is the partial pressure of H₂, $p_{cat} = 101.325$ [Pa] is the cathode pressure, p_{O_2} [Pa] is the partial pressure of O₂ at the anode, and $p_{an} = 101.325$ [Pa].

Reversible cell voltage E^0 is defined as Equation 3.40:

$$E^0 = \frac{\Delta G_R^0}{zF} \quad [V] \quad (3.40)$$

where $\Delta G_R^0 = -237.14$ [kJ/mol] is the Gibbs free energy of the reaction.

Activation overpotential describes the extra voltage, required to overcome the energy barrier of the electrochemical reactions, occurring at the electrodes. Activation overpotential for an electrode (anode or cathode) can be defined by Butler-Volmer Equation 3.41 [13]:

$$V_{act} = \frac{RT_{stack}}{\alpha F} \operatorname{arcsinh} \left(\frac{i}{2i_0} \right) \quad [V] \quad (3.41)$$

where α is the charge transfer coefficient, i [A/cm^2] is the current density, and $i_0 = 0.0001$ [A/cm^2] is the exchange current density.

Total activation overpotential is the sum of the activation overpotentials at anode and cathode:

$$V_{act} = V_{act}^{an} + V_{act}^{cat} \text{ [V]} \quad (3.42)$$

Ohmic overpotential is the voltage loss due to the resistance to the flow of ions through the membrane and electrons through the electrodes and other cell components. Ohmic overpotential is defined as Equation 3.43 [13]:

$$V_{ohm}^{mem} = \frac{\delta_{mem}}{\sigma_{mem}} i \text{ [V]} \quad (3.43)$$

where σ_{mem} [S/cm] is the membrane conductivity, which is expressed as [13]:

$$\sigma_{mem} = \frac{F^2 C_{H^+} D_{H^+}}{RT} \quad (3.44)$$

where membrane concentration of H^+ $C_{H^+} = 1000$ [mol/m^3], diffusivity of the H^+ $D_{H^+} = 3 \cdot 10^{-9}$ [m^2/s] for $T_{stack} = 80^\circ C$ [13].

Concentration overpotential represents the voltage loss due to concentration gradients at high current densities. Concentration overpotential can be expressed as Equation 3.45 [13]:

$$V_{con} = \frac{RT}{4F} \ln \left(\frac{C_{an/mem,O_2}}{C_{an/mem,O_2,0}} \right) + \frac{RT}{2F} \ln \left(\frac{C_{cat/mem,H_2}}{C_{cat/mem,H_2,0}} \right) \quad (3.45)$$

where C_i is the gas concentration at the electrode/electrolyte interface at the operating conditions, and $C_{i,0}$ is the gas concentration electrode/electrolyte interface at the standard conditions.

3.3.5 PEM Electrolyzer Model Summary

The polarization curve for the electrolyzer is presented in Figure 3.7. It illustrates the performance of the PEM electrolyzer, showing the cell voltage and power density as functions of current density. As current density increases, the cell voltage also increases, since more electrical power is required to drive the electrochemical reaction. At low current densities, activation losses dominate, leading to a sharp increase in cell voltage. As current density continues to rise, ohmic losses, occurring primarily due to membrane resistance, become the main contributor to voltage increase, which is reflected in the linear portion of the curve. The electrical power consumed by the electrolyzer is the product of cell voltage and current. Power density thus indicates the amount of electrical power required per unit of active area to sustain hydrogen production at a given current density. As the cell voltage typically increases with current density, the power density also increases. A lower cell voltage at a given current density corresponds to lower power consumption and higher efficiency. However, beyond a certain current density, energy losses in the system become significant, leading to decreased efficiency.

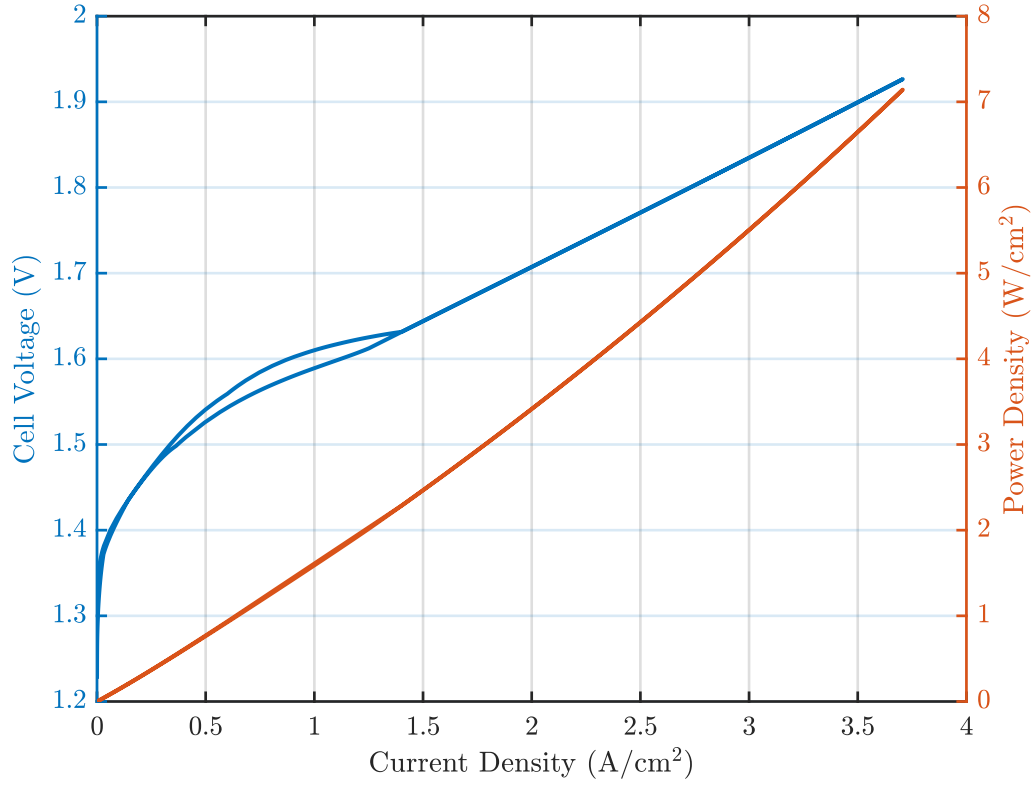


Figure 3.7: PEM electrolyzer i-V and power density curves

The PEM electrolysis system model is developed by using MATLAB/Simulink software. The generated H_2 , O_2 , and transferred H_2O are implemented into the moist air networks via Controlled Trace Gas Source (MA) and Controlled Moisture Source (MA) blocks [49]. Excess heat is directed through thermal port H to the Thermal Mass block [49]. The cathode pressure is maintained at 3 MPa, the temperature of recirculating water is maintained at 80 °C [49]. The main parameters of the electrolyzer stack are presented in the Table 3.4. The PEM electrolysis system model in MATLAB/Simulink is presented in the Figure 3.8.

Table 3.4: Parameters of the electrolyzer stack [49]

Parameter	Value	Unit
Number of cells, N	50	-
Stack area, A_{cell}	280	cm^2
Membrane thickness, δ_{mem}	125	μm
Anode GDL thickness, δ_{el}^{an}	25	μm
Cathode GDL thickness, δ_{el}^{cat}	250	μm
Number of channels, n	8	-
Channel width, w	1	cm
Exchange current density, i_o	0.0001	A/cm^2
Charge transfer coefficient, α	0.7	-

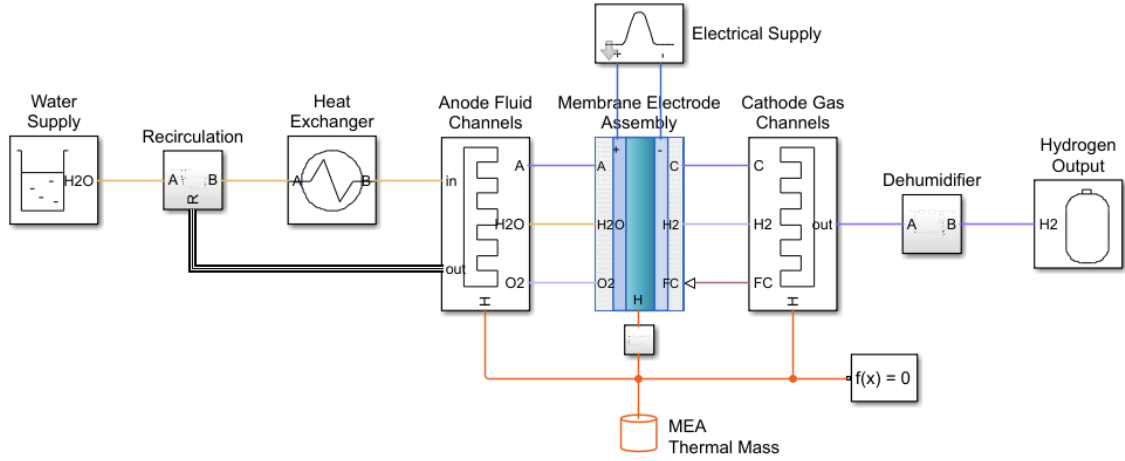


Figure 3.8: PEM electrolysis system model in MATLAB/Simulink [49].

3.4 Other Components of the Plant

3.4.1 Heat Exchangers

All the heat exchangers in the system are assumed to have counter-current flow configuration. The heat balance for the heat exchanger is written as 3.46:

$$Q_{HEX} = \dot{m}_{hot} \cdot C p_{hot} (T_{in,hot} - T_{out,hot}) = \dot{m}_{cold} \cdot C p_{cold} (T_{out,cold} - T_{in,cold}) = U A_{HEX} \Delta T_{ln} \text{ [kW]} \quad (3.46)$$

where subscripts *hot* and *cold* denote hot and cold streams respectively, $U[\text{kW}/(\text{m}^2\text{K})]$ is the overall heat transfer coefficient, $A_{HEX}[\text{m}^2]$ is the heat transfer area, $\Delta T_{ln}[\text{K}]$ is the logarithmic mean temperature difference expressed as 3.47:

$$\Delta T_{ln} = \frac{(T_{in,hot} - T_{out,cold}) - (T_{out,hot} - T_{in,cold})}{\ln\left(\frac{T_{in,hot} - T_{out,cold}}{T_{out,hot} - T_{in,cold}}\right)} \text{ [K]} \quad (3.47)$$

3.4.2 Compressors

All the compressors in the system are assumed to be polytropic. The outlet temperature of a compressor is described as 3.48:

$$T_{out} = T_{in} \left(\frac{P_{out}}{P_{in}} \right)^{\frac{n-1}{n}} \text{ [K]} \quad (3.48)$$

where $T_{in}[\text{K}]$ is the temperature of the gas at the compressor inlet, $P_1[\text{Pa}]$ and $P_2[\text{Pa}]$ is the initial and final pressures of the compressor respectively, n is the polytropic coefficient, which is expressed as 3.49:

$$\frac{n-1}{n} = \frac{1}{\eta_{poly}} \frac{k-1}{k} \quad (3.49)$$

where η_{poly} is the polytropic efficiency taken as 70% [34], and k is the heat capacity ratio at the inlet conditions.

Power requirement for the compressor is given as 3.50:

$$W_{comp} = \dot{N} \frac{n}{n-1} \frac{RT}{\eta_{comp}} \left(\left(\frac{P_2}{P_1} \right)^{\frac{n-1}{n}} - 1 \right) [kW] \quad (3.50)$$

where $\dot{N} [mol/s]$ is the molar flow rate of gas, η_{comp} is the compressor efficiency, which is assumed to be 75% [34].

3.4.3 Buffer Tank

Mass balance in the tank is expressed as Equation 3.51:

$$\frac{dM_i}{dt} = \dot{m}_{in,i} - \dot{m}_{out,i} \left[\frac{kg}{s} \right] \quad (3.51)$$

where subscript i denotes species (H_2 or N_2), $M_i [kg]$ is the mass, and $\dot{m}_{in,i}$ and $\dot{m}_{out,i}$ are the inlet and outlet flow rates of the species in the tank respectively.

3.5 Economic Model

Net present cost (NPC) of the system can be defined as Equation 3.52 [34]:

$$NPC = \sum C_j^{cap} + C^{op} \quad (3.52)$$

where C_j^{cap} is the capital cost for each plant component j and C^{op} is the operational cost of the plant. It is assumed that the system is fully powered by electricity, then the operational cost C^{op} is a function of electricity consumption of the system and the electricity price.

Capital cost for each unit j of the plant can be written as Equation 3.53 [34]:

$$C_j^{cap} = C_{j,fix}^{cap} + C_{j,ref}^{cap} \left(\frac{\chi_j}{\chi_{j,ref}} \right)^{\beta_j} \quad (3.53)$$

where $C_{j,fix}$, $C_{j,ref}$, $\chi_{j,ref}$ and β_j are the cost correlation parameters presented in the Table 3.5. The cost correlation parameters $C_{j,fix}$ and $C_{j,ref}$ for each unit were scaled from 2015 prices to 2025 prices with the chemical engineering plant cost index (CEPCI) from CEPCI 2015 = 556.3 to CEPCI 2025 = 746.1 [51]. The capital cost for the PEM electrolyzer and electrolyzer price per kWh was estimated based on the data provided in [52].

Capital cost of the reactor as a function of the reactor volume (V_{reac}) can be estimated as Equation 3.54:

$$C_{reac}^{cap} = C_{fix}^{cap} + C_{ref}^{cap} \left(\frac{V_{reac}}{20} \right)^{0.52} f_p + 20W_{cat} + 0.31 \cdot 0.5W_{sorb} + 54 \cdot 0.5W_{sorb} \quad (3.54)$$

where C_{fix}^{cap} , C_{ref}^{cap} are cost correlation factors presented in the Table 3.5, 20 [€/kg] is the price of the NH_3 synthesis catalyst [2], W_{cat} is the weight of the catalyst required, as the sorbent used in the reactor is 50 wt% $MnCl_2/SiO_2$ the price of the sorbent was estimated

according to the composition of the sorbent and respective price of each sorbent species (0.31 €/kg for MnCl_2 and 54 €/kg for SiO_2), and W_{sorb} is the weight of the sorbent required, f_p is a pressure multiplier which takes into account increase in the wall thickness of the vessel with increased pressure (P [bar]) which is expressed as Equation 3.55 [34]:

$$f_p = 0.125 \left(\frac{P}{10} \right) + 0.875 \quad (3.55)$$

Table 3.5: Parameters for capital cost correlation [34]

Unit	Basis	$C_{j,fix}$	$C_{j,ref}$	$\chi_{j,ref}$	β_j
Reactor	Volume, m ³	77223.679	309819.6	20	0.52
Compressor	Rated Power, kW	8554.719	8889971	1000	0.9
Heat exchanger	Area, m ²	33062.833	240457	100	0.71

Chapter 4

Validation of the NH₃ Reactor Model

This chapter presents the validation of the models for NH₃ synthesis and absorption processes, implemented in the CFD reactor model, based on the experimental data from literature.

4.1 Validation of the NH₃ Synthesis Process

To validate the implemented NH₃ synthesis kinetic model, the molar fractions of NH₃ (y_{NH_3}) along the reactor length from the CFD model were compared with the experimental data reported in [53]. The CFD simulation conditions were set to match the experimental conditions, using the same inlet temperatures, pressures, and feed ratios, as presented in the Table 4.1. The absorption bed was disabled for this comparison. The gas hourly space velocity (GHSV) of the CFD reactor was also matched to that of the experimental reactor for each case.

Table 4.1: Inlet conditions used in CFD simulations for NH₃ synthesis model validation

Case	Temperature, °C	Pressure, barg	H ₂ /N ₂ , vol.
1	300	10	3
2	300	45	3
3	350	10	3
4	350	45	3
5	300	10	1
6	300	45	1
7	350	10	1
8	350	45	1

Figure 4.1 presents the NH₃ molar fraction along the normalized reactor length for the feed ratio of 3 and 1 for the specified temperatures and pressures. From the Figure 4.1 it can be seen that the CFD model shows strong agreement with the experimental data, showing the increasing trend in y_{NH_3} along the reactor length for all 8 cases. As expected, higher temperatures and pressures result in higher y_{NH_3} according to Le Chatelier's principle. However, for some cases the CFD model tends to under- or over-predict the NH₃ molar fraction distribution. The discrepancies are more notable at higher pressure (45 barg) as the reaction is more sensitive to the kinetic and transport limitations, than at lower pressures. Moreover, the experimental data may include such uncertainties as variations in feed composition, reactor packing, or temperature control, and calibration issues of the measuring devices which may affect the accuracy of the measurements.

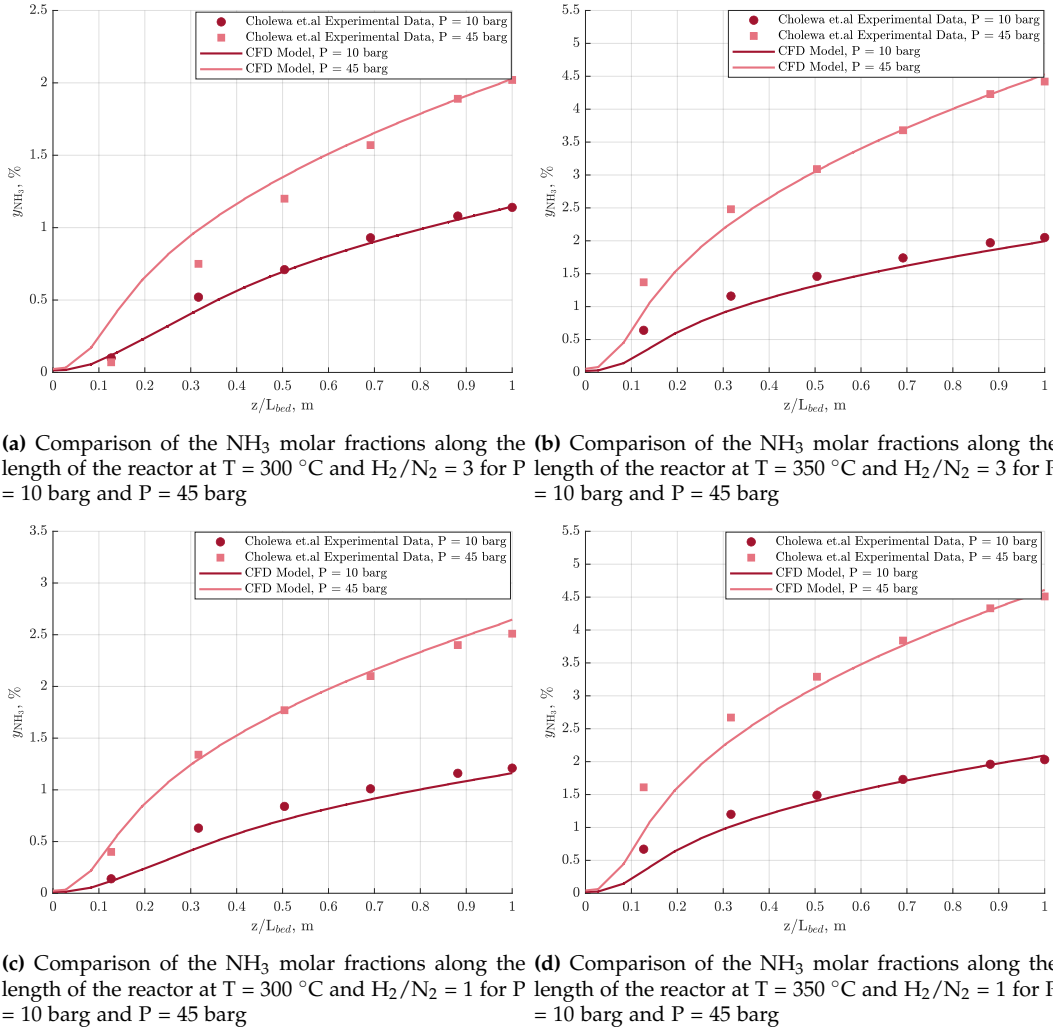


Figure 4.1: NH_3 molar fractions along the length of the reactor for all 8 cases, comparing the CFD model results with the experimental data from [53]

To evaluate the agreement between the CFD results and experimental data, statistical metrics such as R^2 , root mean square error (RMSE), and mean absolute error (MAE) were evaluated. The performance metrics for each case are presented in Table 4.2. A high R^2 and low RMSE and MAE values indicate a strong agreement between the simulation and experimental results. Most data sets exhibit high R^2 values (e.g., 0.99 for Case 1 and 0.99 for Case 6), indicating strong correlation between simulation and experiment. Correspondingly low RMSE and MAE values suggest small deviations in predicted NH_3 molar fractions. However, Cases 7 and 8 show comparatively lower R^2 (0.88 and 0.89) and higher error values, indicating reduced accuracy under the specified conditions, which can be attributed to the kinetic limitations which are not captured by the NH_3 synthesis reaction rate expression at the specified conditions, assumptions made in the CFD model, and experimental uncertainties. Overall, CFD results are consistent with literature data, supporting the accuracy of the implemented kinetic model for NH_3 synthesis.

Table 4.2: Quality metrics between experimental and simulation datasets

Case	R ²	RMSE	MAE
1	0.98691	0.041	0.03079
2	0.93801	0.16856	0.12758
3	0.98923	0.18442	0.1633
4	0.96055	0.20924	0.13646
5	0.9072	0.11137	0.09729
6	0.98965	0.07328	0.06112
7	0.88166	0.16155	0.11735
8	0.89756	0.32102	0.23029

4.2 Validation of the NH₃ Sorption Process

To validate the implemented NH₃ sorption kinetic model, the NH₃ removed over time from the CFD model was compared to the experimental data reported in [27]. The CFD simulation conditions for the sorption bed were set to match the conditions from the experiment as shown in the Table 4.3. In the experiment by [27], before absorption the NH₃ was produced by the 5%Ru/10%Cs/CeO₂ catalyst at 330 °C and 20 barg, while in the CFD model the reaction rate for the conventional Fe-based catalyst at a different temperature condition was implemented. However, as stated in [27], the partial pressure of NH₃ before it enters the sorbent bed is around 1 bar, which matches with the partial pressure of NH₃ before entering the sorbent bed in the CFD model. Moreover, for the better agreement with the experimental results the first 3 minutes of the data were removed for all cases as the NH₃ sorption kinetic model does not account for dispersion [27].

Table 4.3: Inlet conditions used in CFD simulations for NH₃ absorption model validation

Case	Temperature, °C	Pressure, barg	H ₂ /N ₂ , vol.
1	280	20	3
2	300	20	3
3	320	20	3
4	340	20	3

Figure 4.2 presents the rate of NH₃ removal by the sorbent over time, normalized to the sorbent amount. As the time progresses, the rate of absorption of NH₃ gradually declines as the sorption capacity of the sorbent material reduces causing the sorbent to absorb less NH₃ which is observed in both experimental data and CFD model for all 4 cases. However, some discrepancies between the experimental and the model data are observed which can be attributed to the complexity of the actual NH₃ absorption process, which cannot be captured in the kinetic model. For instance, the rate of absorption can be affected by the diffusion of ammonia through the absorbent material in individual particles. Moreover, the CFD model assumes homogenous structure of the sorbent, while in the experiment inhomogeneous structures might be present, resulting in faster saturation of certain particles, which makes it is difficult to capture in the model. Overall, the CFD model shows consistent results with the experimental data, capturing the main trends relatively accurately, which supports its applicability and justifies the assumptions made.

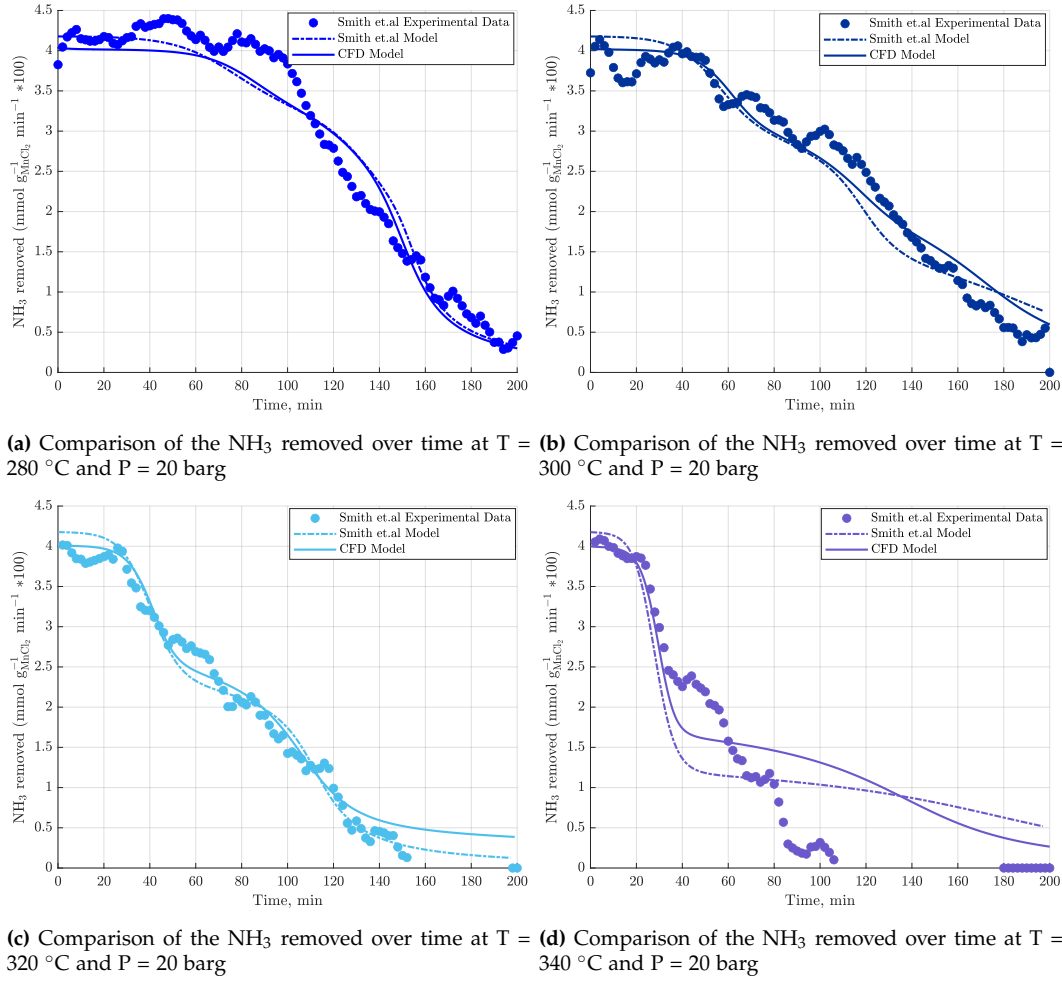


Figure 4.2: NH_3 removed by the sorbent over time for all 4 cases, comparing the CFD model results with the experimental data from [27]

Chapter 5

Results and Discussion

This chapter presents the results obtained from various modelling approaches used in this study. CFD simulations are used to analyze the dynamic performance of the sorption-enhanced ammonia synthesis reactor. FMU model results are presented to evaluate the influence of key inlet parameters on reactor performance. MATLAB/Simulink simulations are used to compare different control strategies for system operation under variable renewable energy input. Finally, results from the techno-economic model are provided to assess and optimize the system's cost-effectiveness and scalability.

5.1 Reactor Performance Analysis

5.1.1 Transient Reactor Operation Analysis

Since the absorption process is transient and the sorbent material loses its capacity over time, determining the optimal time for the reactor operation is essential to maintain efficient operation, as this parameter determines how long the reactor can be operated before the sorbent material requires regeneration. This time-based NH_3 synthesis reactor performance analysis is necessary, as the FMU-based NH_3 reactor model does not account for transient dynamics of the absorption process, and only shows the result at the fixed point in time.

Figure 5.1a shows how the effective NH_3 production rate changes in time. Here, effective NH_3 production rate denotes the amount of NH_3 that was absorbed into the sorbent bed. It can be seen, that over time the effective NH_3 production declines, as sorbent loses its capacity. From the Figure 5.1a the reactor operation can be divided into three stages, which are indicated by the different shades in the figure:

1. 0-60 s: start-up of the reactor, transient behaviour;
2. 60-1800 s: steady operation with highly efficient absorption (> 95%);
3. 1800-3600 s: sorbent capacity decline.

Based on this, the optimal reactor operation time is determined to be 30 minutes. Operating the reactor in the third region of the graph is inefficient as the sorbent capacity is rapidly declining and less portion of the produced NH_3 is being absorbed. Therefore, this optimal operation time is implemented into the FMU-based Simulink reactor model to approximate the need for scheduling for the sorbent regeneration. In the response surface-based FMU model developed in ANSYS, the simulation time was fixed to 30 minutes. Consequently, all output values obtained from the FMU shown below represent reactor performance at the 30-minute mark.

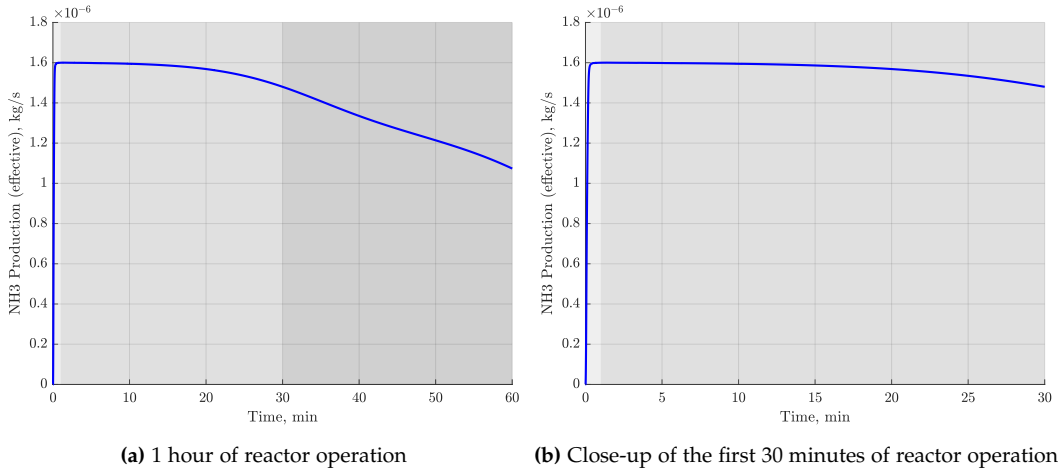


Figure 5.1: Effective NH_3 production rate over time

5.1.2 Reactor Dynamic Behaviour Analysis

As described in Section 3.2.3, the reactor model implemented into the Simulink framework does not capture time-dependent behaviour, while the electrolyzer operates dynamically. To accurately couple these two systems, it is essential to understand how the reactor responds to changes in inlet conditions. Therefore, the effective NH_3 production rate response of the reactor to a step change in the inlet mass flow rate was analysed. Specifically, after reaching steady state, the inlet mass flow was increased by 20%, and the resulting transient behaviour was studied [54]. This analysis allows the reactor dynamics to be approximated using a transfer function of the form shown in Equation 5.1 [54]:

$$G(s) = \frac{K_{plant}}{(T_{plant}s + 1)^n} e^{-\tau s} \quad (5.1)$$

where K_{plant} is the proportional gain, T_{plant} is the time constant, which represents the reactor response time, τ is the time delay and n is the order of the transfer function.

Figure 5.2 presents the NH_3 production rate response to the step change in the inlet mass flow for two cases: reactor with in-situ NH_3 absorption (Figure 5.2a) and reactor without in-situ NH_3 absorption (Figure 5.2b). From the Figure 5.2a it can be determined that the reactor with NH_3 absorption responds fast to the changes in the mass flow and does not have a visible delay. However, there is a noticeable overshoot which is attributed to the mass transfer effects and the time required for the CFD solver to adjust to the new parameters. Figure 5.2b presents the NH_3 production response to the step change in the inlet mass flow at time 3 minutes for the reactor without integrated absorption. The reactor responds much slower in this case with a clear delay, taking more time for the reactor to adjust to the new flow condition.

The response of both reactors can be approximated by a first-order transfer function. The transfer function fitting parameters for the both cases are presented in the Table 5.1. From the fitted parameters it can be seen that absorption allows for a faster response of the reactor in NH_3 production due to the active equilibrium shift occurring due to the

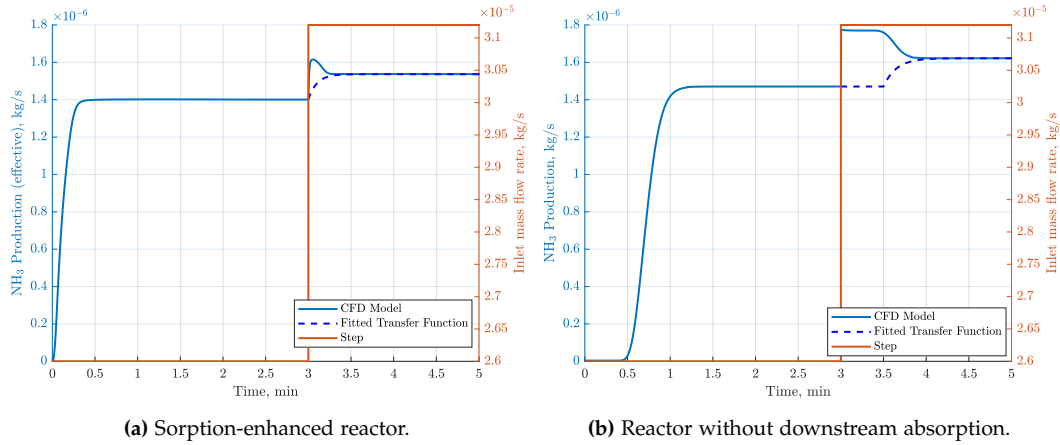


Figure 5.2: The response of NH_3 production to the 20% step change in the inlet mass flow.

NH_3 absorption downstream of the catalyst bed, which promotes a more rapid ammonia production. While for the case without absorption, there is no force that will actively push the equilibrium towards the product side, resulting in a slower response by the reactor. Overall, the reactor with absorption responds almost immediately to the changes in the mass flow, which makes it more suitable for dynamic operation under variable inlet conditions. This response time of the effective NH_3 production rate to the changes in the mass flow is then implemented for the FMU reactor model in MATLAB/Simulink using a first-order transfer function.

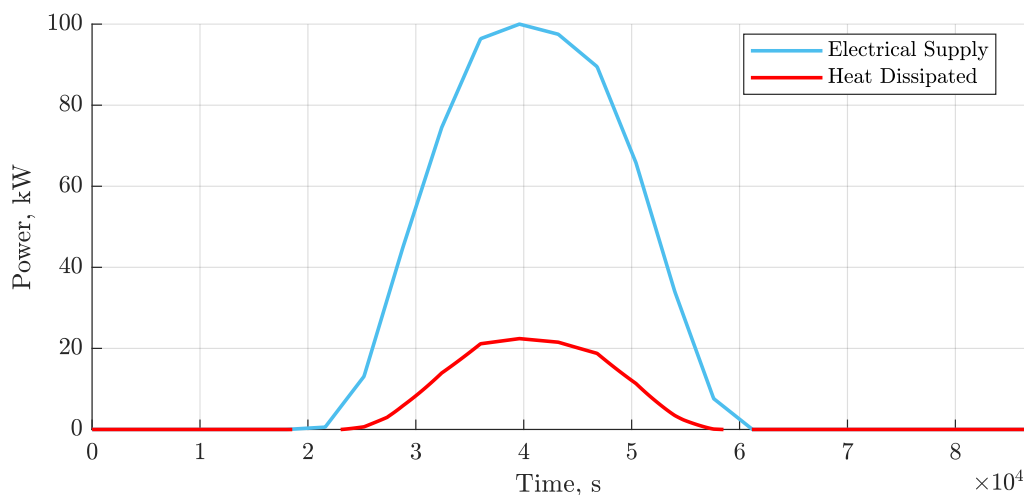
Table 5.1: Transfer function fitting parameters.

Parameter	Absorption integrated reactor	Reactor without absorption
K_{plant}	1	1
T_{plant}, s	6	9
τ, s	0	30

5.1.3 Optimal Reactor Operating Range

The performance characteristics of the NH_3 synthesis reactor strongly depend on the inlet conditions of the reactor namely inlet mass flow (\dot{m}_{in}), inlet pressure, inlet temperature, and N_2/H_2 ratio. In this work, the inlet pressures and temperatures were fixed to 30 bar and 300 °C to match the operating conditions of the PEM electrolyzer model.

Figure 5.3 presents the H_2 production profile from a single electrolyzer stack and the corresponding electrical power input as a function of time over 24 hours of electrolyzer stack operation for a clear sunny day. From the Figure 5.3a it can be observed that the power supplied to the electrolyzer varies over time, depending on solar panel power generation. According to Faraday's law, H_2 production is directly proportional to the electrical current supplied to the electrolyzer. Therefore, as more power is provided, greater amounts of H_2 are generated, while low power supply yields less H_2 production (Figure 5.3b). Since H_2 production is dependent on fluctuating renewable power inputs, total mixture inlet mass flow rate into the NH_3 reactor is also variable over time, making \dot{m}_{in} a crucial parameter for investigation for efficient NH_3 reactor operation.



(a) Power supply and heat dissipated in the PEM electrolyzer.

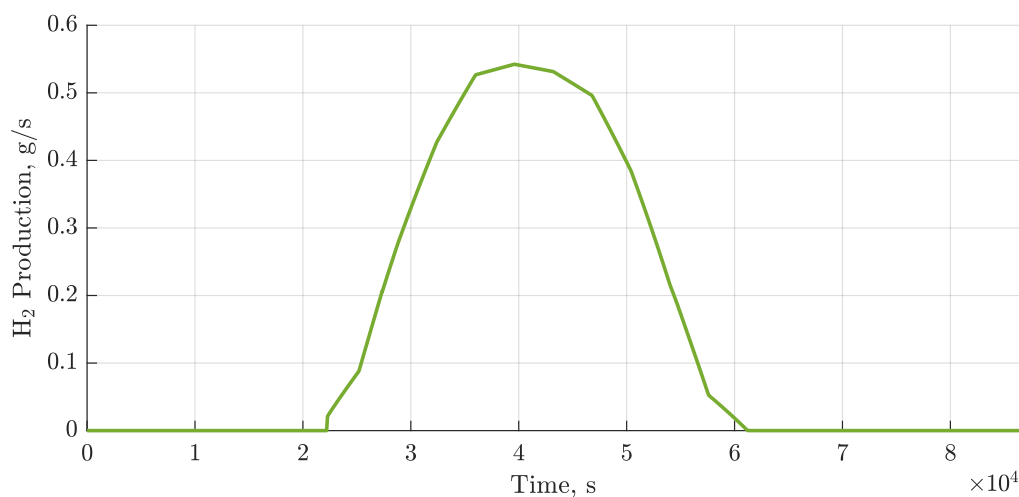
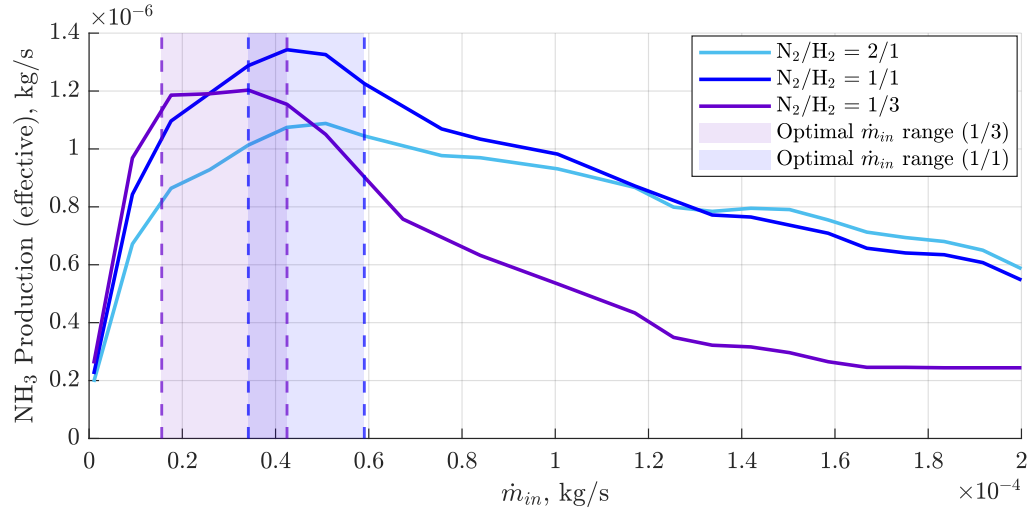
(b) H₂ production by the electrolyzer over time.**Figure 5.3:** PEM electrolyzer performance characteristics for a single stack.

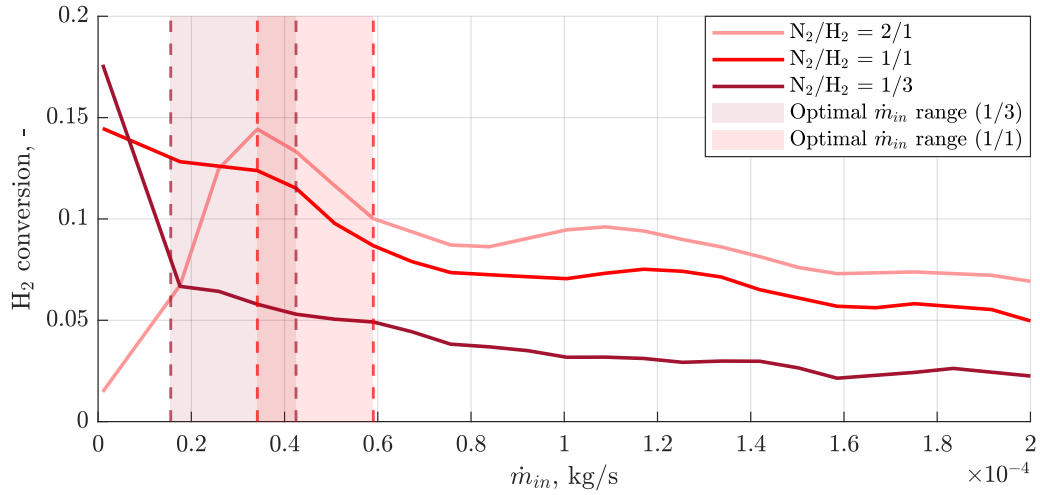
Figure 5.4 illustrates the influence of the inlet mass flow rate and N_2/H_2 ratio on three key reactor performance metrics: NH_3 production, H_2 conversion, and NH_3 absorbed fraction, recorded after 30 minutes of reactor operation. As shown in Figures 5.4b and 5.4c, lower inlet mass flow rates result in higher H_2 conversion and increased NH_3 absorption efficiency, due to the longer residence time of the reactants within the beds, allowing for more complete reaction and absorption. In contrast, higher flow rates reduce the residence time of the reactants in the bed, thereby limiting reaction efficiency and decreasing both H_2 conversion and NH_3 absorbed fraction. However, the trend for NH_3 production (Figure 5.4a) shows a peak for a certain flow rate. At low flow rates, the limited supply of reactants restricts the overall production of NH_3 , even though the hydrogen conversion remains high due to longer residence time. As the inlet flow rate increases, the availability of reactants improves, resulting in a higher NH_3 production rate. However, beyond a certain point, further increase in the flow rate reduces the residence time to such extent that the lower conversion outweighs the benefit of additional reactants and in-situ absorp-

tion, resulting declining NH_3 production rate. Additionally, the benefit of in-situ NH_3 absorption in shifting the reaction equilibrium toward product formation, is declining at high flow rates due to reduced NH_3 formation, leading to higher NH_3 partial pressure downstream of the catalyst bed and less efficient NH_3 absorption, reducing the driving force for absorption.

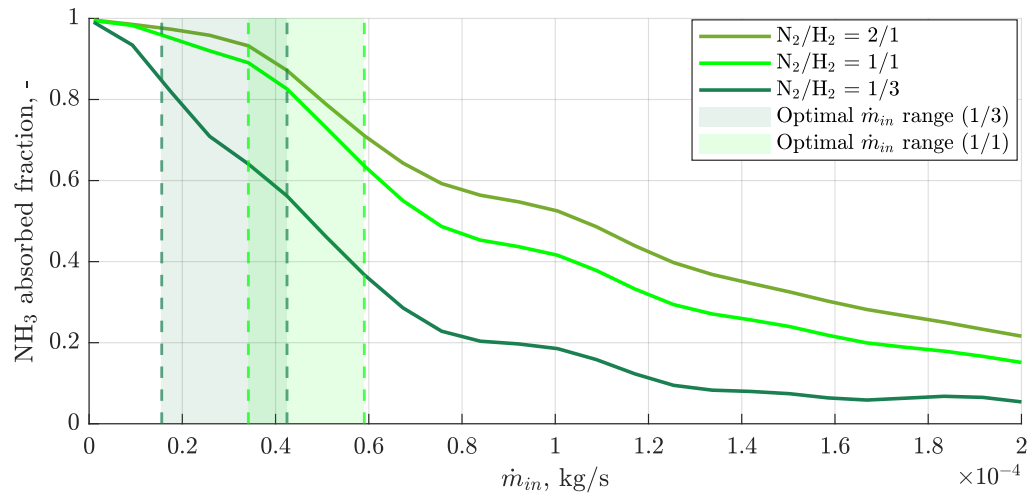
Moreover, from the Figure 5.4, it can be seen that N_2/H_2 ratio also has a significant impact on the reactor performance. Operating with over-stoichiometric ratios ($\text{N}_2/\text{H}_2 > 1/3$) generally enhances both H_2 conversion and NH_3 absorption across the set range of inlet mass flow rates. This can be attributed to increase in the residence time of the reactants in the beds, caused by lower mixture velocity due to increased N_2 content. However, at too low mass flows and N_2/H_2 ratio = 2/1, H_2 conversion decreases due to low mixture velocity and mass transfer within the reactor. Overall, the NH_3 production rate for the N_2/H_2 ratio = 2/1 is the lowest, despite having high H_2 conversion, as the low H_2 partial pressures result in low reaction rates. With higher N_2/H_2 ratios, the partial pressure of N_2 increases across the reactor due to the excess N_2 flow. At higher \dot{m}_{in} operating at over-stoichiometric ratios can be more beneficial as the NH_3 production rate decreases less rapidly with increasing mass flow, and the reaction rate increases at over-stoichiometric ratios. Overall, these results indicate the presence of an optimal range of inlet mass flow rates for maximizing NH_3 production at each N_2/H_2 ratio. The identified optimal regions for $\text{N}_2/\text{H}_2 = 1/3$ and $\text{N}_2/\text{H}_2 = 1/1$ are marked with dashed lines in Figures 5.4a to 5.4c.



(a) NH_3 production rate as a function of inlet mass flow for $\text{N}_2/\text{H}_2 = 1/3$, $\text{N}_2/\text{H}_2 = 1/1$, $\text{N}_2/\text{H}_2 = 2/1$.



(b) H_2 conversion as a function of inlet mass flow for $\text{N}_2/\text{H}_2 = 1/3$, $\text{N}_2/\text{H}_2 = 1/1$, $\text{N}_2/\text{H}_2 = 2/1$.



(c) NH_3 absorbed fraction as a function of inlet mass flow for $\text{N}_2/\text{H}_2 = 1/3$, $\text{N}_2/\text{H}_2 = 1/1$, $\text{N}_2/\text{H}_2 = 2/1$.

Figure 5.4: Reactor performance characteristics as a function of inlet mass flow for $\text{N}_2/\text{H}_2 = 1/3$, $\text{N}_2/\text{H}_2 = 1/1$, $\text{N}_2/\text{H}_2 = 2/1$.

Previously, the reactor operation analysis was performed for a single layer of catalyst and sorbent. However, for a bigger system having such a small reactor is inefficient, as the H_2 conversion in a single pass is low ($<10\%$) and the system requires recycling of the unreacted species to increase the H_2 conversion. Moreover, having multiple layers of catalyst and sorbent was shown to increase both H_2 conversion and NH_3 production significantly [27]. Thus, to increase the conversion and eliminate the need for recycling, 14 single layer reactor models were connected in sequence to produce one reactor tube. Figure 5.5 presents the effective NH_3 production for a sequence of 14 reactors as a function of inlet mass flow. It can be seen that implementing 14 reactors in sequence significantly increases the effective NH_3 production, as all of the unreacted gases from the previous steps get converted again in the next reactor. It can be seen that the overall trend for NH_3 production for a reactor sequence is similar to that of a single layer. However, the peaks in the NH_3 production are more distinct and occur at higher flow rates, than for one layer cases. This is mainly due to overall increased NH_3 production rate caused by the increased number of catalyst and sorbent layers. As was described before $N_2/H_2 = 2/1$ yields overall poorer effective NH_3 production, compared to ratios of $1/3$ and $1/1$ and was not shown in this figure. The optimal mass flow rate range for maximizing the effective NH_3 production was determined to be in the range of $2.7 \cdot 10^{-5} \text{ kg/s}$ to $5.7 \cdot 10^{-5} \text{ kg/s}$ for the stoichiometric N_2/H_2 ratio and $5.1 \cdot 10^{-5} \text{ kg/s}$ to $7.5 \cdot 10^{-5} \text{ kg/s}$ for $N_2/H_2 = 1/1$.

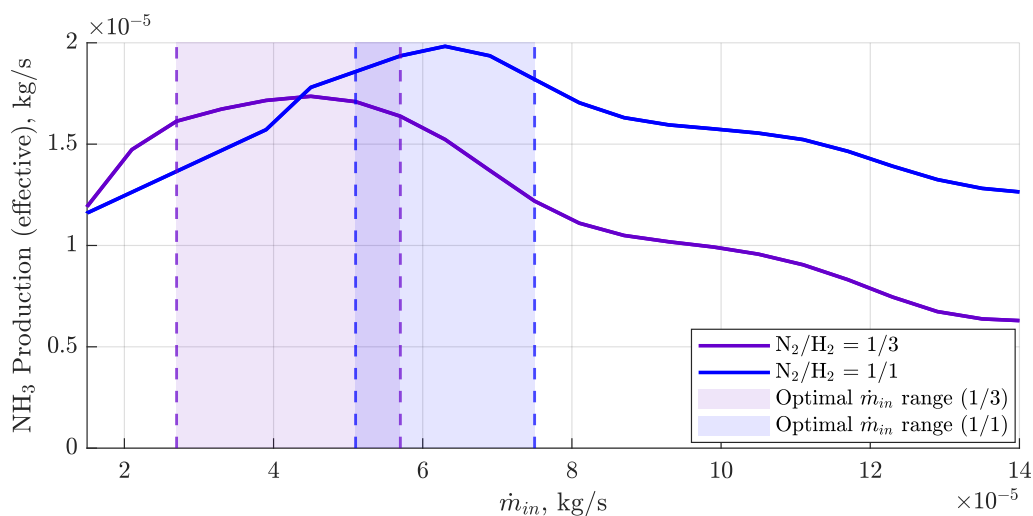


Figure 5.5: NH_3 production as a function of inlet mass flow for a reactor sequence.

Overall, the absorption-integrated NH_3 synthesis reactor demonstrates a faster dynamic response to the changes in inlet mass flow compared to the conventional reactor without absorption. However, unlike for conventional reactors, its efficient operation is limited in time due to sorbent saturation. While, on the other hand, the H_2 conversion in such reactor can be significantly increased by having multiple layers of catalyst and sorbent material in series by ensuring efficient NH_3 separation. Moreover, for each N_2/H_2 ratio there is a feasible inlet mass flow range where NH_3 production is maximized. All of this indicates, that NH_3 absorption integrated reactors can be potentially integrated with a highly-dynamic PEM electrolyzer as a H_2 source. However, the dependence of the NH_3 production rates on the inlet mass flows together with the existence of the optimal ranges of the inlet mass flows for maximizing the efficient NH_3 production, underscored the

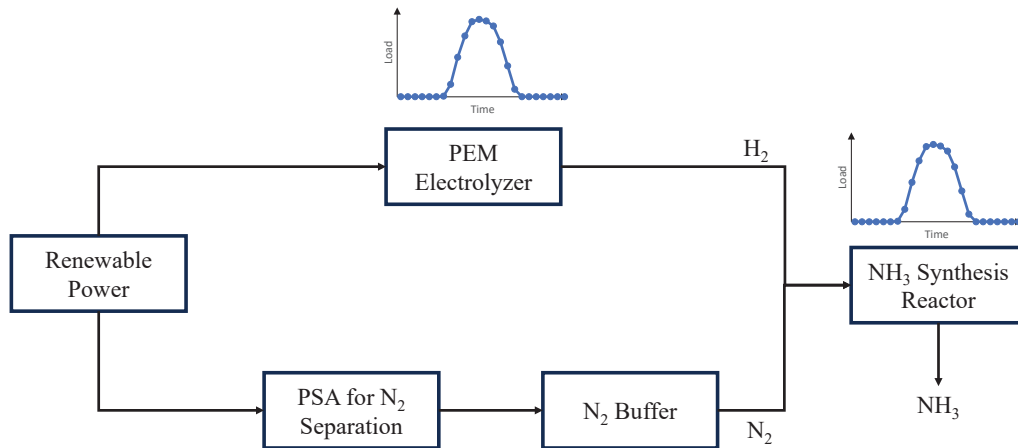
requirement for effective control strategies, aimed to maintain the reactor inlet parameters within its optimal performance range.

5.2 NH₃ Reactor Control Strategies Comparison

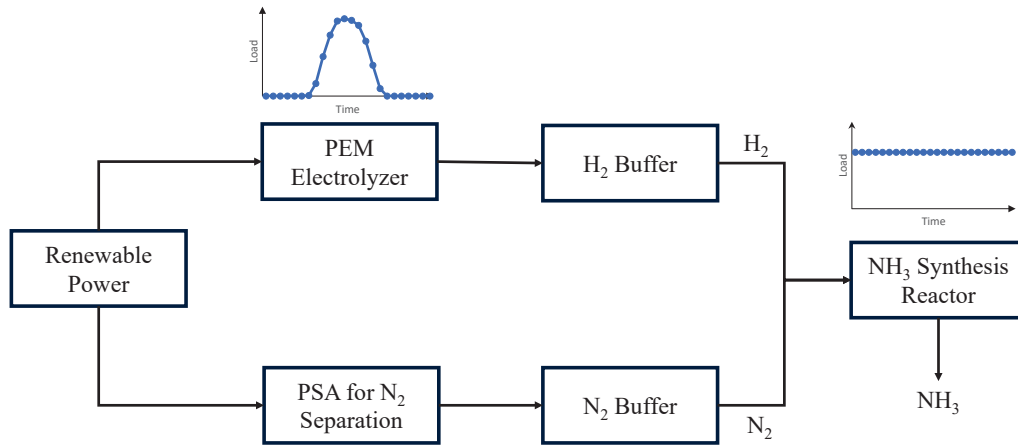
5.2.1 Effect of Control Strategies on NH₃ Production Dynamics

For power-to-ammonia systems coupled with an electrolyzer powered by renewable energy, two main operating strategies can be considered to handle the variability in power supply:

- Fully dynamic operation: both electrolyzer and NH₃ reactor operate under dynamically variable load (Figure 5.6a);
- Partially dynamic operation: the electrolyzer operates dynamically, but the NH₃ reactor is decoupled and runs at steady-state conditions, fed by hydrogen stored in a buffer tank (Figure 5.6b).



(a) Fully dynamic load concept of PtA operation



(b) Partially dynamic load concept of PtA

Figure 5.6: Power-to-Ammonia operating concepts

Since H_2 production is variable over time and depends directly on the input power, while the reactor performance efficiency strongly depends on the feed flow rate, maintaining optimal reactor operating conditions requires the implementation of an appropriate control strategy. To maximize NH_3 production, it is advantageous to operate the reactor within the optimal range of inlet mass flow rates. The control strategies proposed for this system are summarized in the Table 5.2

Table 5.2: Summary of control strategies evaluated in the system

Strategy	Description
Strategy 1	Single reactor operating across the full range of inlet mixture mass flows.
Strategy 2	Two reactors operating simultaneously; each operates only within its respective optimal range of inlet mass flows.
Strategy 3	All H_2 produced by the electrolyzer is first stored in a hydrogen tank. The stored H_2 is then fed into the reactor at a controlled rate, maintaining optimal NH_3 production conditions.
Strategy 4	Single reactor with adaptive inlet control, dynamically switching the N_2/H_2 ratio based on the inlet mixture flow rate.

In each scenario, NH_3 production is initiated (i.e., the reactor is in the "on" state) once H_2 production reaches a sufficient and stable rate. The reactor is shut down when the H_2 production rate drops below that threshold. Due to the integrated in-situ absorption bed, the reactor exhibits a fast dynamic response with minimal delay to variations in mass flow, allowing for improved flexibility under fluctuating hydrogen supply condition. To ensure continuous operation despite the sorbent saturation that limits the reactor's operating time, each reactor is paired with a secondary (backup) reactor. A switching control strategy, which can be seen in Figure 5.7, is implemented where reactors alternate between absorption and desorption phases every 30 minutes, while actual desorption process was not implemented. However, it is assumed that all NH_3 that was absorbed during this time period is desorbed from the sorbent during these 30 minutes. The reactors are expected to have fast dynamic response, as each one must switch between the "on" (absorption) and "off" (desorption) states up to 8 times to cover the full H_2 production profile. However, for the readability of the graphs, this switching behaviour was not included in the final plots presented below.

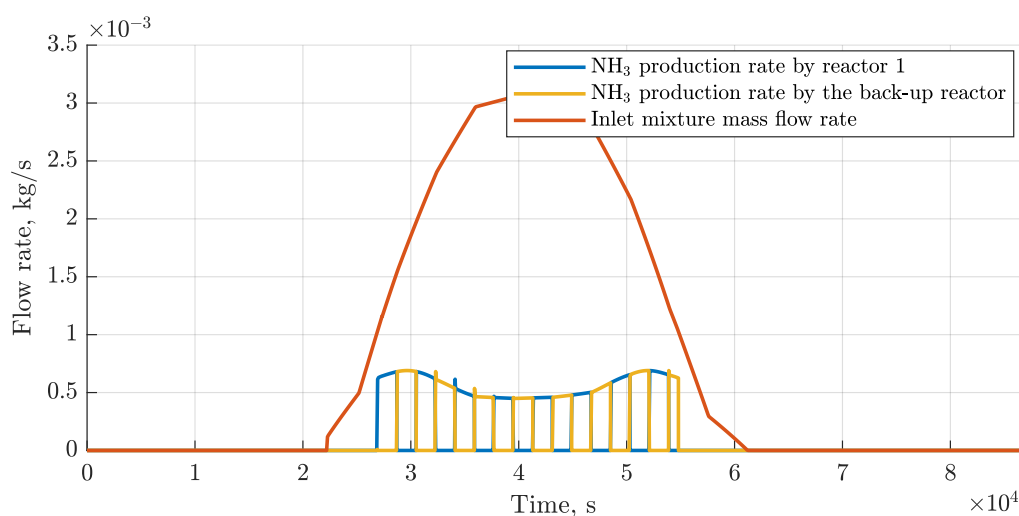


Figure 5.7: Switching logic between main and backup reactors to ensure continuous operation

Figure 5.8 illustrates the profiles of NH_3 production rate and inlet mixture mass flow over time for Control Strategy 1. In this strategy, H_2 is continuously supplied directly to the reactor without intermediate storage. Initially, the NH_3 production rate increases as the inlet mass flow enters the reactor's optimal operating range. However, as H_2 production continues to increase, the feed flow rate increases proportionally. This results in the feed flow rates being outside the optimal operating range, causing a decline in NH_3 production despite high H_2 availability. Consequently, during periods when H_2 production is at its peak, the reactor operates less efficiently, resulting in a generally low NH_3 production rate over the entire time profile.

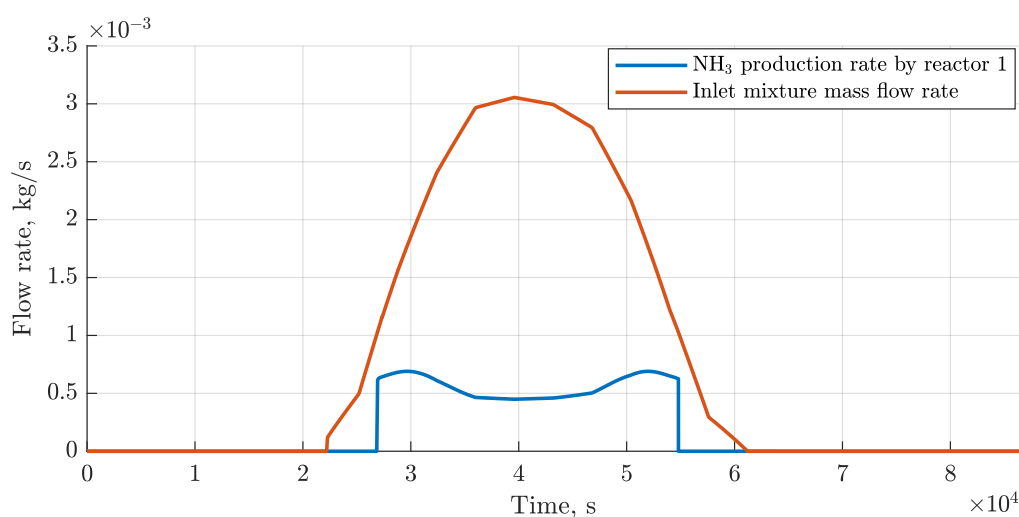


Figure 5.8: NH_3 production profile for control Strategy 1: Single reactor operating across the full range of inlet mixture mass flows.

The effective NH_3 production profile and feed mixture flow rate for Control Strategy 2 are presented in Figure 5.9. In this strategy, when H_2 production reaches its peak and the resulting feed flow rate exceeds the reactor's optimal operating range, a second reactor is

activated to operate in parallel with the first. This approach prevents a decline in NH_3 production during the period of high H_2 production by maintaining the inlet flow rate to each reactor within the optimal range, thereby enhancing overall production efficiency. As H_2 production begins to decrease, the second reactor is shut down, while the first reactor continues to operate within its optimal range.

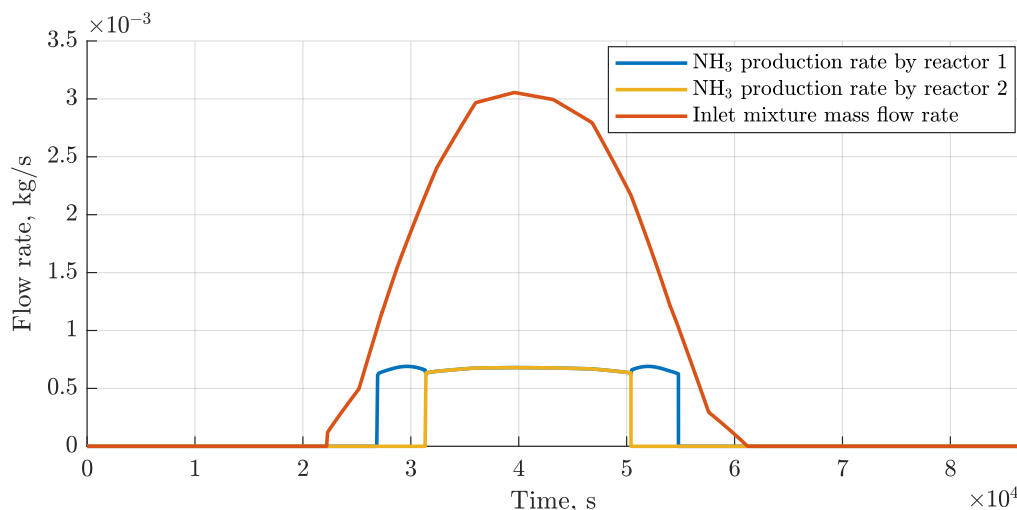


Figure 5.9: NH_3 production profile for control Strategy 2: Two reactors operating simultaneously during the peak \dot{m}_{in} .

Another approach to maximize NH_3 production involves the use of a H_2 buffer tank, which releases hydrogen at a constant, optimal flow rate. Figure 5.10 shows the resulting NH_3 production profile for this strategy. In this case, the flow into the reactor remains steady, while H_2 is produced dynamically, and the reactor is shut down once the buffer tank is depleted. This setup ensures that all the H_2 produced is effectively utilized in the reactor. Unlike for Strategy 2, this approach eliminates the need for additional reactors to maintain optimal operating conditions, for the peak in H_2 production, as the feed is continuously delivered at the most optimal mass flow rate.

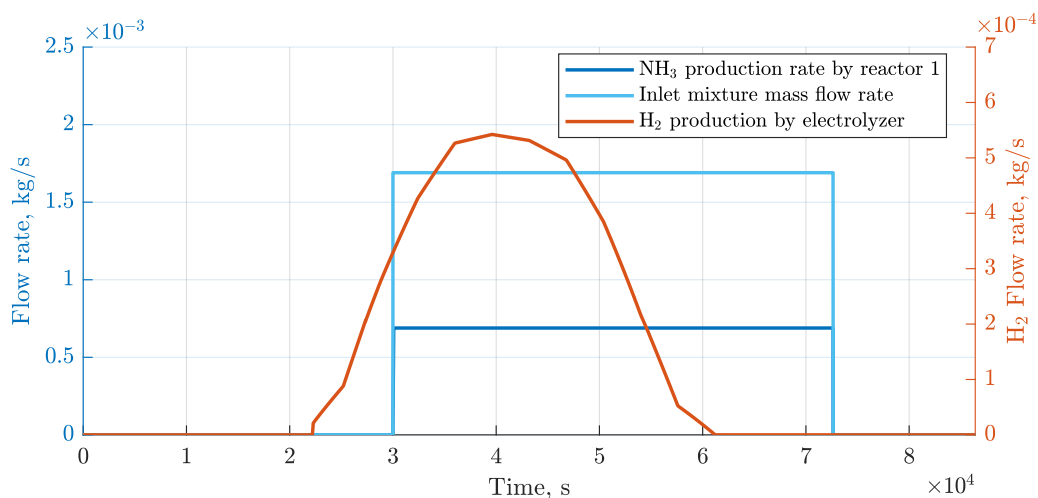


Figure 5.10: NH_3 production profile for control Strategy 3: Steady reactor load due to H_2 buffering.

As shown in Figure 5.5, operating the reactor at a stoichiometric N_2/H_2 ratio provides only a limited range of inlet mass flow rates that yield efficient NH_3 production. Consequently, when Control Strategy 1 is applied, the reactor operates inefficiently at high inlet mass flow rates, as the effective NH_3 production begins to decline. To enhance NH_3 production without adding new components, like in Strategy 2 and 3, the optimal operating range can be extended by switching to a N_2/H_2 ratio of 1/1 once the mass flow exceeds a certain threshold ($\dot{m}_{in} > 1.79 \cdot 10^{-3}$ kg/s). Figure 5.11 illustrates the NH_3 production rate for Control Strategy 4, where the total inlet mass flow is adjusted by varying the H_2 flow to maintain the target ratio. It can be observed that when NH_3 production begins to decline due to increasing mixture flow rate, the system switches to an over-stoichiometric feed ratio. This control logic allows the NH_3 production rate to rise briefly. However, even with this strategy, NH_3 production still decreases at peak H_2 supply, as the operating window remains too narrow to sustain optimal production across the full range of inlet flow rates. Nevertheless, compared to Strategy 1, the duration of suboptimal NH_3 production is significantly reduced, leading to an overall improvement in performance.

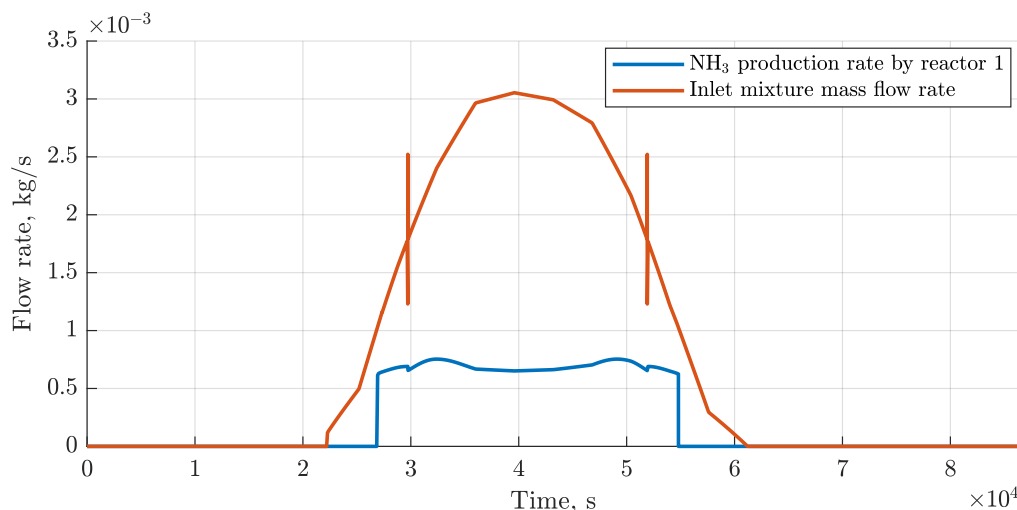


Figure 5.11: NH_3 production profile for control Strategy 4: Adaptive inlet N_2/H_2 ration control.

5.2.2 Comparison of the Reactor Control Strategies

Figure 5.12 presents the NH_3 production (in kg) over time for the four evaluated reactor control strategies. Strategy 3 exhibits the longest reactor operation period due to a steady and controlled H_2 input from the buffer tank. However, production begins later compared to the other strategies, as sufficient H_2 must first accumulate in the tank to sustain the desired flow rate to the reactor. In contrast, Strategies 1, 2, and 4 initiate ammonia production simultaneously, with similar total operation durations. From the plot, it is evident when in time the control logic changes occur in Strategies 2 and 4, marked by noticeable slope changes in the production curves compared to Strategy 1. The NH_3 mass increases approximately linearly over time for Strategies 2, 3, and 4, reflecting efficient and consistent operation within optimal flow conditions. In contrast, Strategy 1 shows a less linear growth, primarily due to prolonged operation outside the reactor's optimal mass flow range, resulting in reduced production rates. Overall, the implementation of control

strategies, particularly Strategies 2 and 3, leads to a substantial improvement in NH_3 yield compared to the baseline Strategy 1.

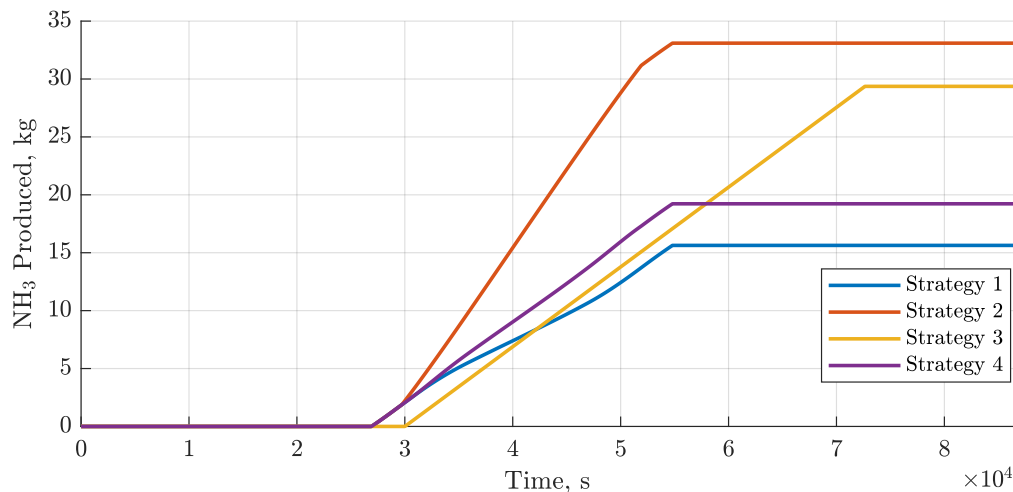


Figure 5.12: NH_3 produced over time for the four NH_3 reactor control strategies.

Table 5.3 compares the performance of the four NH_3 reactor control strategies for small-scale ammonia synthesis system in terms of daily effective NH_3 production, hydrogen conversion, and specific energy consumption (W , in kWh per kg of NH_3 produced). This energy consumption mainly accounts for the power input into the electrolyzer, power input required for compressors in the PSA system and their interstage cooling, and power input for preheating of the reactants. H_2 conversion is presented as a time-averaged value, since it depends on the variable inlet mass flow rate. Strategy 1, in which a single reactor operates without buffering or flow control, shows the lowest performance characteristics compared to other control strategies, with only 15.63 kg/day of NH_3 produced, 43% hydrogen conversion, and the highest energy consumption at 36.02 kWh/kg NH_3 . This is due to the reactor operating outside the optimal mass flow range under variable hydrogen supply, for the most part of the system operation time. In contrast, Strategy 2, which employs two reactors operating in parallel during peak H_2 production period, significantly improves system performance. The highest NH_3 output (33.1 kg/day) and with the lowest specific energy consumption of 17 kWh/kg NH_3 is achieved when this control strategy is employed, indicating effective utilization of H_2 . Strategy 4, with dynamically adjustable N_2/H_2 ratio, extends the reactor's operational range, allowing it to operate under optimal conditions for a longer time. This strategy mitigates inefficiencies of the first scenario, resulting in increased daily NH_3 output (19.22 kg/day) and significantly improved hydrogen conversion (70%). However, the overall NH_3 production rate remains lower than for Strategies 2 or 3, indicating its limited improvement capacity. Strategy 3, which uses a buffer tank to supply hydrogen at a constant optimal rate, achieves nearly comparable NH_3 output (29.37 kg/day) and hydrogen conversion (60%) to Strategy 2, with a slightly higher energy demand (19.32 kWh/kg). This approach avoids the need for multiple reactors or complex control strategies while maintaining near-optimal conditions, making it an energy-efficient and operationally simpler alternative.

In summary, Strategy 2 offers the best overall performance in terms of output and efficiency, but at the cost of system complexity and the need for secondary reactor. Strategy 3 provides a balance between performance and operational simplicity, while the use of adjustable feed ratio in Strategy 4 improves hydrogen utilization, but is less energy efficient, than Strategies 2 and 3. Strategy 1 alone is the least favourable, despite being the least operationally complex, due to poor hydrogen conversion, high energy consumption, and low NH_3 production rates.

Table 5.3: Comparison of the control strategies in terms of the system performance characteristics for small scale NH_3 production

Control Strategy	NH_3 production, kg/day	H_2 conversion, %	W, kWh/kg NH_3
Strategy 1	15.63	43	36.02
Strategy 2	33.1	61	17
Strategy 3	29.37	60	19.32
Strategy 4	19.22	70	29.35

5.3 Techno-Economic Analysis and Optimization

5.3.1 System Upscaling and Resource Distribution Analysis

The proposed control strategies are subsequently applied to upscale the system for a target production capacity of 300 kg of NH_3 per day. This production level was selected based on a commercially available solution developed by [55]. The upscaling process involved increasing the number of electrolyzer stacks, thereby proportionally increasing the total H_2 production rate. To accommodate the higher hydrogen supply and maintain reactor performance, the number of reactor tubes was also increased proportionally. This ensured that the flow rate per tube remained within the valid operating range of the FMU reactor model.

Understanding how energy is distributed among system components is essential for identifying potential areas for efficiency improvement and cost reduction. Figure 5.13 illustrates the power consumption distribution for Strategy 1 in percentage terms. The distribution is consistent across all four strategies, with variations of less than 1%. As shown in the Figure 5.13, the PEM electrolyzer accounts for nearly 90% of the total system energy consumption. This is expected, as electrolysis is a fundamentally energy-intensive step, requiring significant electrical power to split water into oxygen and hydrogen. This is primarily due to the high cell voltage required to overcome the thermodynamic and kinetic barriers of water splitting. Moreover, PEM systems also consume more energy compared to alkaline electrolyzers due to membrane resistance and generally have lower efficiency. In this study, an electrolyzer efficiency was assumed to be around 65–70% (based on the LHV). In contrast, the power required for nitrogen separation via PSA and its subsequent compression to the reactor's operating pressure is minimal, being less than 1% of the total consumption. This is primarily due to the system's operation under mild pressure conditions, which significantly reduces compression energy demands. The energy consumption of the PSA unit is mostly limited to compressing air and nitrogen to relatively low pressures. Strategy 3, which includes hydrogen buffering, requires additional energy

for hydrogen compression before storage. However, this adds only around 1.2% of the total system energy, and thus does not significantly alter the overall distribution. The heat exchanger, which preheats the H_2/N_2 gas mixture prior to entering the reactor, contributes up to 10% of total energy consumption. This is necessary because the feed gases enter at lower temperatures than the reactor's operating temperature. While reducing the reactor temperature could potentially enhance hydrogen conversion and reduce the energy required for the process, it would also significantly reduce reaction rates, making further temperature reduction operationally unfeasible.

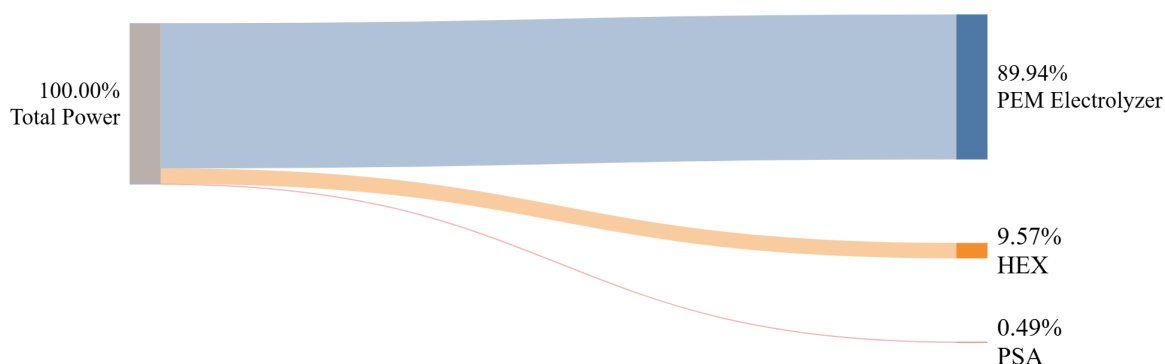


Figure 5.13: Sankey diagram of power consumption distribution

Figure 5.14 presents the distribution of capital costs across the main system components for each of the four control strategies. For Strategies 1, 2, and 4, the ammonia synthesis reactor represents the largest share of total system cost, contributing between 70% and 86%. This high cost can be attributed to the reactor's complex construction, catalyst and sorbent loading, and the need to scale with hydrogen production capacity. For these cases, the reactor is significantly more expensive than the PEM electrolyzer, which contributes between 5% and 20% of the total cost. In contrast, Strategy 3, which employs a hydrogen buffer tank to regulate flow, redistributes the system costs by shifting a portion of the expense toward energy storage and buffering infrastructure. Here, the hydrogen storage tank becomes the dominant cost component, accounting for approximately 65% of the total system cost. This is due to the high cost of pressurized storage infrastructure, especially at the scale required to buffer daily hydrogen production. Across all strategies, the PSA unit and heat exchanger represent a relatively small portion of the overall cost, each contributing less than 7%. This highlights the capital-intensive nature of both the reactor and hydrogen utilization components compared to auxiliary systems.

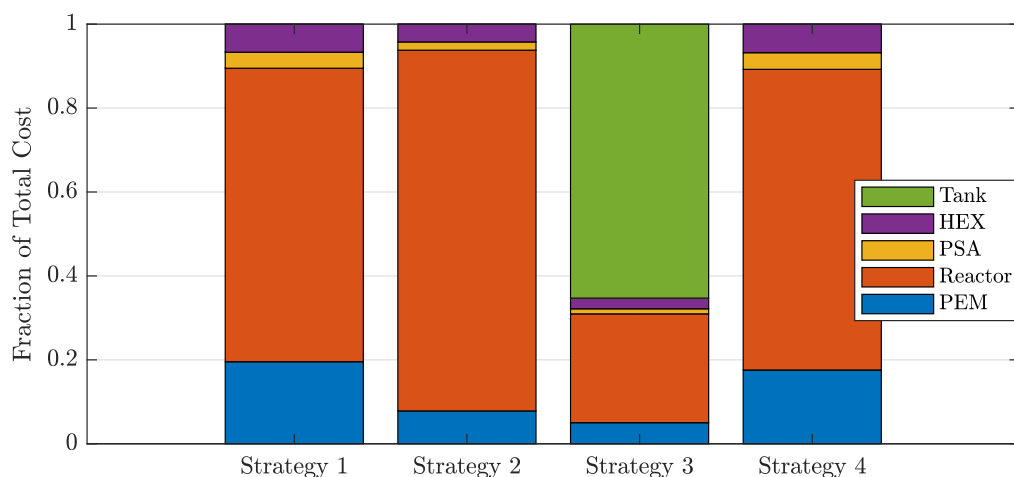


Figure 5.14: Component cost distribution per strategy

5.3.2 System Design Optimization

To identify the most optimal control strategy for the selected NH_3 production scale, a multi-objective optimization problem was formulated. The problem objective was to simultaneously minimize three key performance indicators over a 1-year project lifetime: levelized cost of ammonia (LCOA), power consumption, and total system cost.

Figure 5.15 presents a Pareto plot, illustrating the trade-offs between specific power consumption, LCOA, and total system cost for the four proposed control strategies. Among all of the strategies, Strategy 2 was found to be the most optimal solution, achieving the lowest values across all three optimization objectives. This is attributed to the dual-reactor operation with dynamic switching, which effectively balances the load, reduces peak demands, while efficiently utilizing H_2 . Consequently, Strategy 2 minimizes both operational and capital costs, making it the most Pareto-optimal solution.

In contrast, Strategy 1 is the least energy-efficient and more expensive to operate, as it has the highest power demand among all the proposed strategies. While its total system cost is moderate, the LCOA remains relatively high at €2.39/kg, which is still significantly higher than that of Strategy 2. Although Strategy 1 does not require costly components such as a hydrogen tank or additional reactors, its high energy consumption increases operating costs over time due to increased number of electrolyzer stacks required to meet the desired NH_3 production scale. This highlights a key limitation: the lack of expensive infrastructure does not compensate for the inefficiency in energy usage, making Strategy 1 less favourable overall. Strategy 3 is the least cost-effective overall. It has the highest LCOA (€2.71/kg) and total cost, due to the added cost of the hydrogen storage tank, which greatly contributes to the overall cost of the system. While it reduces specific power consumption to 19.32 kWh/kg compared to Strategy 1, the cost of implementing hydrogen buffering outweighs the efficiency gains. This indicates that partially steady reactor operation implementing the hydrogen storage is not economically viable without additional cost-reduction measures. This shows, that it is more expensive to implement a hydrogen buffer tank and use the reactor in a steady load, than having both electrolyzer and

a reactor operate dynamically for the chosen system lifetime. Strategy 4 introduced ratio switching to optimize hydrogen-to-nitrogen feed ratios dynamically, improving conversion efficiency. It demonstrated better performance than Strategy 1 in all metrics, reducing LCOA to €2.00/kg and energy consumption to 29.35 kWh/kg. However, the added system complexity and higher component cost did not surpass the overall performance of Strategy 2.

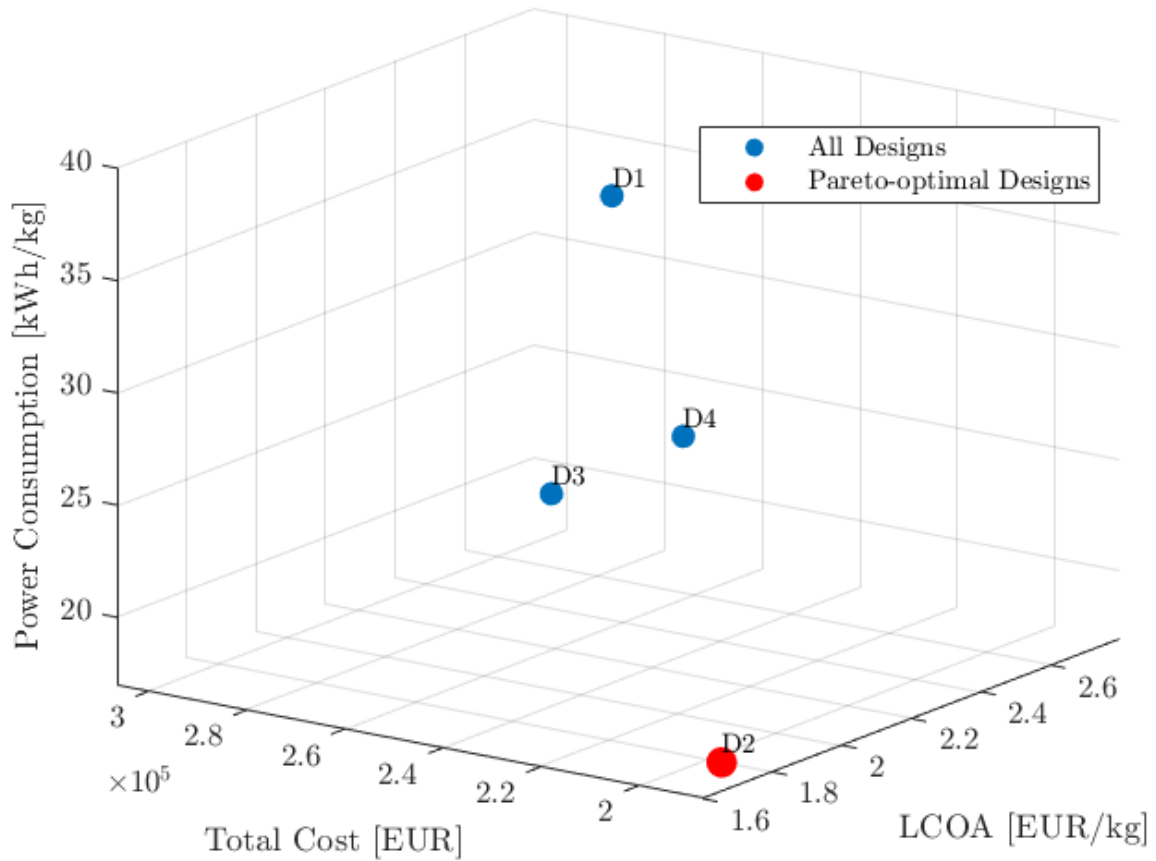


Figure 5.15: Pareto front for the proposed system designs. D1 - Control Strategy 1, D2 - Control Strategy 2, D3 - Control Strategy 3, D4 - Control Strategy 4.

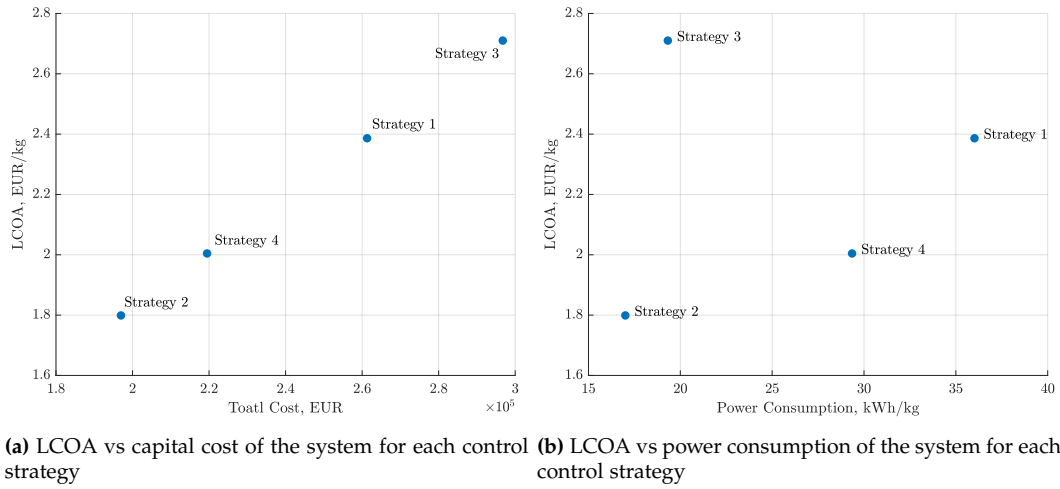


Figure 5.16: Comparison of LCOA, capital cost of the system and power consumption for the proposed system designs

Table 5.4 summarizes the main parameters a comparison of four control strategies for producing 300 kg of ammonia per day, based on three key metrics: specific energy consumption (W , in kWh/kg NH_3), total reactor volume required per reactor, and the levelized cost of ammonia (LCOA, in €/kg NH_3). While Strategy 2 requires two smaller reactors operating in parallel, its high ammonia production rate and efficient hydrogen utilization make it the most feasible option overall. However, if space constraints exist, Strategy 4 could be a more suitable alternative, as it requires a smaller total reactor volume than the combined reactor volume in Strategy 2 and has a similar LCOA.

Table 5.4: Parameters for producing 300 kg of NH_3 /day

Control Strategy	W , kWh/kg NH_3	Reactor Volume, m^3	LCOA, €/kg NH_3
Strategy 1	36.02	6.7	2.39
Strategy 2	17	3.34	1.8
Strategy 3	19.32	3.7	2.71
Strategy 4	29.35	5.39	2

5.4 Discussion of the Feasibility of Decentralized Green NH_3 Production

Green NH_3 production systems, such as the one proposed in this study, are designed to operate at a much smaller scale than the conventional Haber-Bosch process and are capable of operating without direct CO_2 emissions. In this study, a coupled modelling framework was employed by integrating an FMU-based reactor model, developed through CFD, into MATLAB/Simulink environment. This approach allows to couple the reactor model with the PEM electrolyzer model and other system components, as well as the implementation of the control strategies. The main characteristic of the proposed system is the integration of an absorption bed downstream of the catalyst zone. A key limitation of this modelling approach lies in the fact that the developed FMU model is steady-state and its outputs are fixed for a specific time point. Moreover, this type of model cannot directly capture

the fully transient dynamics of such reactor. This configuration enables the reactor to respond rapidly to changes in mass flow, making it well-suited for decentralized applications requiring flexibility and fast load-following capabilities. The efficiency of ammonia production in such absorption-enhanced systems is highly sensitive to reactor operating conditions and the control strategies implemented. While the novel reactor configuration enhances NH_3 yield and improves the system's dynamic performance, it also introduces considerable design complexity. In particular, the need for control strategies to ensure continuous reactor operation, as the reactor operation time is limited due to sorbent saturation. Furthermore, achieving high single-pass H_2 conversion under mild conditions necessitates the use of multiple consequent layers of catalyst and sorbent beds. This requirement increases the reactor length and the overall quantity of catalyst and sorbent materials needed, making the reactor one of the most expensive components of the system.

Green ammonia production systems are characterized by high electricity consumption, primarily due to the relatively low efficiency of hydrogen production via water electrolysis compared to hydrogen derived from steam methane reforming (SMR) of natural gas. While the ammonia synthesis loop in green systems operating under mild conditions may offer some energy-saving advantages, such as the use of electric compressors, reduced compression requirements, pressurized hydrogen output from electrolysis, and minimal purge losses due to high-purity feedstocks, these benefits are currently insufficient to offset the substantial energy demand of the electrolysis process. However, advances in electrolyzer technology and efficiency have the potential to significantly lower the total energy consumption of green ammonia systems, thereby enhancing both environmental sustainability and economic viability [9].

On the other hand, green ammonia systems currently remain economically uncompetitive compared to conventional Haber-Bosch process. This is primarily due to the high cost of electricity, especially from renewable sources, relative to the low cost of natural gas, as well as the significant capital investment required for electrolyzer stacks and novel reactor designs [56]. While the integration of an absorption-enhanced reactor improves reactor efficiency and H_2 conversion by removing NH_3 in situ, thereby potentially lowering specific energy consumption, connected with cryogenic NH_3 separation, the overall system cost remains highly sensitive to electricity prices, as the whole system is powered by electrical energy. Although ongoing advancements in PEM electrolyzer technology are expected to reduce costs over time, these systems are still expensive and represent a major portion of the total investment. In contrast, the Haber-Bosch process has benefited from over a century of technological refinement, economies of scale, and integration into global industrial infrastructure. Consequently, even the most optimized green ammonia systems today remain more costly per kilogram of NH_3 produced, particularly in Europe where electricity prices are significantly higher than those for natural gas [56]. Moreover, the intermittency of renewable energy sources necessitates additional infrastructure such as hydrogen storage and battery systems to enable continuous operation. These storage solutions further increase both capital and operational expenditures. Finally, the small scale of decentralized green ammonia plants, compared to the large scale of conventional plants, limits the potential for cost reduction through economies of scale.

Despite its promising dynamic performance, the system's overall energy consumption and low ammonia production scales make it currently less competitive than the conventional Haber-Bosch process. This is largely due to the high cost and energy requirements of the PEM electrolyzer. However, the cost of PEM electrolyzer stacks is expected to decrease significantly from €1071/kWh to around €243/kWh in 2030, potentially improving the system's economic viability [52]. Furthermore, future advances in electrolyzer efficiency may reduce both capital and operational costs. Moreover, as this process is electrically-driven and its operation costs significantly depend on the renewable electricity prices, further decrease in renewable electricity generation can improve the cost-competitiveness of the overall system. Nevertheless, the sorption-enhanced reactor remains more expensive than the electrolyzer, accounting for nearly 75% of the total cost of the system, and requires further optimization, particularly in terms of simplifying its design and reducing material requirements, while maintaining high NH_3 production rates under mild conditions.

Green ammonia systems may be particularly feasible for deployment in remote or off-grid areas where transportation costs for conventionally produced ammonia may exceed the local levelized cost of ammonia. When ammonia is consumed at or near the point of production, its transportation costs are minimized, enhancing the economic attractiveness of such systems. Additionally, the modularity of green ammonia plants allows for flexible scaling of production capacity by adding reactor-electrolyzer units, making them well-suited for decentralized and variable-demand applications. The mild operating conditions of the proposed system, characterized by lower pressures and temperatures, further contribute to feasibility of such systems by reducing energy demands associated with gas compression. However, it is important to acknowledge that the current techno-economic assessment is based on a simplified model that includes only the primary components: the ammonia reactor, PEM electrolyzer, compressors, and heat exchangers. For a comprehensive evaluation, future work should incorporate the desorption process for sorbent regeneration, which is essential for continuous operation in absorption-enhanced systems.

Although fully dynamic operation can potentially improve short-term performance of the system, it may lead to accelerated degradation rates of the plant components over time. For instance, fully dynamic operation of the PEM electrolyzer stack can lead to anode and cathode catalyst degradation and membrane thinning for high load cycling, which would affect the lifetime of the stack [57]. This needs to be taken into account when determining the lifetime of the system as PEM electrolyzer is one of the components, significantly impacting the cost of the overall system. The NH_3 synthesis reactor catalyst and sorbent materials are also subject to degradation. Dynamic operation involves rapid load changes, causing reactor bed temperatures to change more rapidly, affecting the reactor's durability [22]. Thermal cycling is a main risk associated with dynamic operation for the whole PtA system, potentially causing damage to the NH_3 synthesis catalysts. A key risk with sorption-enhanced NH_3 synthesis reactors is improving the stability of sorbent materials for operation at extended cycles [27]. The dynamic operation involves frequent cycles of ammonia absorption and subsequent regeneration (desorption), typically via temperature or pressure swings [28]. Frequent absorption-desorption switching and dynamic load can also potentially affect the degradation mechanisms of the sorbent materials, which would impact heavily the cost of the system in the long term. Over many such cycles, the sorbent material can experience structural stability issues caused by volume swings during the

absorption/desorption process, which can lead to a loss of efficiency [58]. This highlights a need for sorbents that are thermally stable over several absorption/desorption cycles [58]. Based on this, Strategy 3, which utilizes a buffer H₂ tank to maintain steady state load for the reactor, may offer long-term advantages by reducing frequent thermal and mechanical stresses on plant components. However, this comes with the cost of increased capital investments and energy demands for additional H₂ handling infrastructure.

Chapter 6

Conclusion and Future Work

This study contributes to ongoing research on decentralized green ammonia production by investigating and modelling of a novel sorption-enhanced NH_3 synthesis reactor into a system powered by intermittent renewable energy. The reactor's dynamic behaviour, integration challenges, control strategy development, and the current techno-economic feasibility of such systems were explored. The dynamic behaviour of the sorption-enhanced NH_3 reactor was investigated, with particular focus on how inlet mixture flow rates and N_2/H_2 feed ratios influence the reactor performance. Optimal ranges for these parameters were identified to maximize ammonia production, and based on this four control strategies were proposed. Among them, Strategy 2, which utilizes two reactors operating in parallel during periods of high hydrogen production, was found to be the most effective, achieving the highest ammonia output (33.1 kg/day). In general, operating the reactors fully dynamically was found to be more advantageous, than operating the reactor under a steady load, especially from the economical point of view for short-term application, as H_2 handling infrastructure being the main cost-driving component for the steady load case. However, the long-term effects of highly-dynamic operation on degradation mechanisms of both the PEM electrolyzer and NH_3 reactor, were not accounted for in this study and need to be further modelled and investigated, to accurately approximate the system's lifetime and its long-term economic feasibility.

Overall, the proposed sorption-enhanced green NH_3 production system integrated with PEM electrolysis offers several advantages. It demonstrates a fast dynamic response, which makes it particularly suitable for integration with intermittent renewable energy sources. Its operation at low pressure contributes to lower compressor requirements and thus reduced costs for compression. Moreover, the system produces zero direct CO_2 emissions during operation, supporting decarbonization goals. However, several challenges remain. The capital costs of the main components, especially the PEM electrolyzer and the complex reactor system, are currently high. The process also demands significant energy input due to the high energy requirements of water electrolysis. Additionally, the integration of a suitable and efficient desorption process for the absorbent remains a technical challenge that must be addressed in the future work.

In summary, the analysis of the upscaled green ammonia production system identifies two key components that require further development: the PEM electrolyzer and the absorption-integrated reactor. The electrolyzer currently accounts for nearly 90% of the system's total energy demand due to the energy-intensive nature of water splitting. Meanwhile, the reactor is the largest contributor to capital costs, primarily because of its design complexity and scale. Future research should therefore focus on improving the efficiency and durability of the electrolyzer to reduce energy demand and costs, as well as optimizing the reactor design to lower capital expenditure while maintaining high conversion

efficiency under mild operating conditions. Additionally, the integration of an effective desorption process is essential to ensure continuous and reliable system operation.

Several areas for future research were identified during the study. For instance, as the control strategies, developed in this study, involve simple switching logic, future work should explore more sophisticated control strategies, potentially using model predictive control or other advanced methods that can leverage a dynamic reactor model to better manage the coupling between the highly dynamic PEM electrolyzer and the reactor. These strategies should optimize not only the flow rate but also account for the state of the sorbent, temperature dynamics, and energy requirements for both ammonia desorption and absorbent regeneration under fluctuating power conditions. A more comprehensive evaluation should incorporate all essential process units, especially the energy-intensive sorbent regeneration, which was excluded in the current study. This would provide a more accurate understanding of the overall energy consumption and LCOA, particularly impacting strategies dependent on frequent regeneration. Future work should also include efforts to further optimize the design and operation of both the electrolyzer and the novel reactor. This includes investigating potential improvements in electrolyzer efficiency to reduce overall energy consumption and exploring reactor design modifications or alternative materials/configurations to lower capital costs and potentially improve conversion rates under mild conditions.

Bibliography

- [1] International Energy Agency. *Net Zero by 2050*. Tech. rep. Licence: CC BY 4.0. Paris: International Energy Agency, 2021. URL: <https://www.iea.org/reports/net-zero-by-2050>.
- [2] Carlos Arnaiz del Pozo and Schalk Cloete. "Techno-economic assessment of blue and green ammonia as energy carriers in a low-carbon future". In: *Energy Conversion and Management* 255 (2022), p. 115312. ISSN: 0196-8904. DOI: <https://doi.org/10.1016/j.enconman.2022.115312>. URL: <https://www.sciencedirect.com/science/article/pii/S019689042200108X>.
- [3] Jannik Burre et al. "Power-to-X: Between Electricity Storage, e-Production, and Demand Side Management". In: *Chemie Ingenieur Technik* 92.1-2 (2020), pp. 74–84. DOI: <https://doi.org/10.1002/cite.201900102>. eprint: <https://onlinelibrary.wiley.com/doi/pdf/10.1002/cite.201900102>. URL: <https://onlinelibrary.wiley.com/doi/abs/10.1002/cite.201900102>.
- [4] M. Stanley Whittingham. "Materials Challenges Facing Electrical Energy Storage". In: *MRS Bulletin* 33.4 (2008), 411–419. DOI: 10.1557/mrs2008.82.
- [5] Simone Mucci, Alexander Mitsos, and Dominik Bongartz. "Power-to-X processes based on PEM water electrolyzers: A review of process integration and flexible operation". In: *Computers & Chemical Engineering* 175 (2023), p. 108260. ISSN: 0098-1354. DOI: <https://doi.org/10.1016/j.compchemeng.2023.108260>. URL: <https://www.sciencedirect.com/science/article/pii/S0098135423001308>.
- [6] NIST Chemistry WebBook. *NIST Chemistry WebBook*. Accessed: 2024-12-09. 2024.
- [7] Mostafa El-Shafie, Shinji Kambara, and Yukio Hayakawa. "Hydrogen Production Technologies Overview". In: *Journal of Power and Energy Engineering* 07 (01 2019), pp. 107–154. ISSN: 2327-588X. DOI: 10.4236/jpee.2019.71007.
- [8] Us Department of Energy. *Potential Roles of Ammonia in a Hydrogen Economy A Study of Issues Related to the Use Ammonia for On-Board Vehicular Hydrogen Storage*. 2006.
- [9] Collin Smith, Alfred K. Hill, and Laura Torrente-Murciano. "Current and future role of Haber–Bosch ammonia in a carbon-free energy landscape". In: *Energy Environ. Sci.* 13 (2 2020), pp. 331–344. DOI: 10.1039/C9EE02873K. URL: <http://dx.doi.org/10.1039/C9EE02873K>.
- [10] Mostafa El-Shafie and Shinji Kambara. "Recent advances in ammonia synthesis technologies: Toward future zero carbon emissions". In: *International Journal of Hydrogen Energy* 48.30 (2023). ProfSpecial issue on the 4th International Symposium on Hydrogen Energy and Energy Technologies (HEET 2021), pp. 11237–11273. ISSN: 0360-3199. DOI: <https://doi.org/10.1016/j.ijhydene.2022.09.061>. URL: <https://www.sciencedirect.com/science/article/pii/S0360319922041763>.
- [11] Jimmy A. Faria. "Renaissance of ammonia synthesis for sustainable production of energy and fertilizers". In: *Current Opinion in Green and Sustainable Chemistry* 29 (2021), p. 100466. ISSN: 2452-2236. DOI: <https://doi.org/10.1016/j.cogsc.2021.100466>. URL: <https://www.sciencedirect.com/science/article/pii/S2452223621000225>.

- [12] Matthew J. Palys and Prodromos Daoutidis. "Power-to-X: A review and perspective". In: *Computers & Chemical Engineering* 165 (2022), p. 107948. ISSN: 0098-1354. DOI: <https://doi.org/10.1016/j.compchemeng.2022.107948>. URL: <https://www.sciencedirect.com/science/article/pii/S009813542200285X>.
- [13] Vincenzo Liso et al. "Modelling and Experimental Analysis of a Polymer Electrolyte Membrane Water Electrolysis Cell at Different Operating Temperatures". In: *Energies* 11.12 (2018). ISSN: 1996-1073. DOI: 10.3390/en11123273. URL: <https://www.mdpi.com/1996-1073/11/12/3273>.
- [14] IEA. *The Future of Hydrogen: Seizing Today's Opportunities*. Paris Cedex 16: OECD, 2019. DOI: 10.1787/1e0514c4-en. URL: <https://doi.org/10.1787/1e0514c4-en>.
- [15] Xiaojun Shen et al. "Experimental study on the external electrical thermal and dynamic power characteristics of alkaline water electrolyzer". In: *International Journal of Energy Research* 42.10 (2018), pp. 3244–3257. DOI: <https://doi.org/10.1002/er.4076>. eprint: <https://onlinelibrary.wiley.com/doi/pdf/10.1002/er.4076>. URL: <https://onlinelibrary.wiley.com/doi/abs/10.1002/er.4076>.
- [16] O. Schmidt et al. "Future cost and performance of water electrolysis: An expert elicitation study". In: *International Journal of Hydrogen Energy* 42.52 (2017), pp. 30470–30492. ISSN: 0360-3199. DOI: <https://doi.org/10.1016/j.ijhydene.2017.10.045>. URL: <https://www.sciencedirect.com/science/article/pii/S0360319917339435>.
- [17] Qi Feng et al. "A review of proton exchange membrane water electrolysis on degradation mechanisms and mitigation strategies". In: *Journal of Power Sources* 366 (2017), pp. 33–55. ISSN: 0378-7753. DOI: <https://doi.org/10.1016/j.jpowsour.2017.09.006>. URL: <https://www.sciencedirect.com/science/article/pii/S0378775317311631>.
- [18] Kevin H.R. Rouwenhorst et al. "Islanded ammonia power systems: Technology review & conceptual process design". In: *Renewable and Sustainable Energy Reviews* 114 (2019), p. 109339. ISSN: 1364-0321. DOI: <https://doi.org/10.1016/j.rser.2019.109339>. URL: <https://www.sciencedirect.com/science/article/pii/S1364032119305477>.
- [19] A.R Smith and J Klosek. "A review of air separation technologies and their integration with energy conversion processes". In: *Fuel Processing Technology* 70.2 (2001), pp. 115–134. ISSN: 0378-3820. DOI: [https://doi.org/10.1016/S0378-3820\(01\)00131-X](https://doi.org/10.1016/S0378-3820(01)00131-X). URL: <https://www.sciencedirect.com/science/article/pii/S037838200100131X>.
- [20] Shunchao Wang et al. "Scheduling power-to-ammonia plants considering uncertainty and periodicity of electricity prices". In: *Smart Energy* 11 (2023), p. 100113. ISSN: 2666-9552. DOI: <https://doi.org/10.1016/j.segy.2023.100113>. URL: <https://www.sciencedirect.com/science/article/pii/S2666955223000205>.
- [21] Deepak K. Ojha et al. "Integrated Ammonia Synthesis and Separation". In: *ACS Sustainable Chemistry and Engineering* 7 (23 Dec. 2019), pp. 18785–18792. ISSN: 21680485. DOI: 10.1021/acssuschemeng.9b03050.
- [22] Steffen Fahr et al. "Dynamic simulation of a highly load-flexible Haber–Bosch plant". In: *International Journal of Hydrogen Energy* 102 (2025), pp. 1231–1242. ISSN: 0360-3199. DOI: <https://doi.org/10.1016/j.ijhydene.2025.01.039>. URL: <https://www.sciencedirect.com/science/article/pii/S0360319925000473>.

- [23] Michael Reese et al. "Performance of a Small-Scale Haber Process". In: *Industrial & Engineering Chemistry Research* 55.13 (2016), pp. 3742–3750. DOI: 10.1021/acs.iecr.5b04909. eprint: <https://doi.org/10.1021/acs.iecr.5b04909>. URL: <https://doi.org/10.1021/acs.iecr.5b04909>.
- [24] Mahdi Malmali et al. "Converting Wind Energy to Ammonia at Lower Pressure". In: *ACS Sustainable Chemistry & Engineering* 6.1 (2018), pp. 827–834. DOI: 10.1021/acssuschemeng.7b03159. eprint: <https://doi.org/10.1021/acssuschemeng.7b03159>. URL: <https://doi.org/10.1021/acssuschemeng.7b03159>.
- [25] Matthew J. Kale et al. "Optimizing Ammonia Separation via Reactive Absorption for Sustainable Ammonia Synthesis". In: *ACS Applied Energy Materials* 3 (3 Mar. 2020), pp. 2576–2584. ISSN: 25740962. DOI: 10.1021/acsaem.9b02278.
- [26] Navid Erfani, Luqmanulhakim Baharudin, and Matthew Watson. "Recent advances and intensifications in Haber-Bosch ammonia synthesis process". In: *Chemical Engineering and Processing - Process Intensification* 204 (2024), p. 109962. ISSN: 0255-2701. DOI: <https://doi.org/10.1016/j.cep.2024.109962>. URL: <https://www.sciencedirect.com/science/article/pii/S0255270124003003>.
- [27] Collin Smith and Laura Torrente-Murciano. "Exceeding Single-Pass Equilibrium with Integrated Absorption Separation for Ammonia Synthesis Using Renewable Energy—Redefining the Haber-Bosch Loop". In: *Advanced Energy Materials* 11 (13 Apr. 2021). ISSN: 16146840. DOI: 10.1002/aenm.202003845.
- [28] Bosong Lin et al. *Perspective on Intensification of Haber-Bosch to Enable Ammonia Production under Milder Conditions*. July 2023. DOI: 10.1021/acssuschemeng.2c06711.
- [29] Zhixin Sun et al. "Modeling and simulation of dynamic characteristics of a green ammonia synthesis system". In: *Energy Conversion and Management* 300 (2024), p. 117893. ISSN: 0196-8904. DOI: <https://doi.org/10.1016/j.enconman.2023.117893>. URL: <https://www.sciencedirect.com/science/article/pii/S0196890423012396>.
- [30] Collin Smith et al. "Rates of Ammonia Absorption and Release in Calcium Chloride". In: *ACS Sustainable Chemistry & Engineering* 6.9 (2018), pp. 11827–11835. DOI: 10.1021/acssuschemeng.8b02108. eprint: <https://doi.org/10.1021/acssuschemeng.8b02108>. URL: <https://doi.org/10.1021/acssuschemeng.8b02108>.
- [31] Mahdi Malmali et al. "Ammonia Synthesis at Reduced Pressure via Reactive Separation". In: *Industrial & Engineering Chemistry Research* 55.33 (2016), pp. 8922–8932. DOI: 10.1021/acs.iecr.6b01880. eprint: <https://doi.org/10.1021/acs.iecr.6b01880>. URL: <https://doi.org/10.1021/acs.iecr.6b01880>.
- [32] Collin Smith and Laura Torrente-Murciano. "Low Temperature and Pressure Single-Vessel Integrated Ammonia Synthesis and Separation using Commercial KATALCO Catalysts: Green ammonia synthesis using renewable energy". In: *Johnson Matthey Technology Review* 66 (4 Oct. 2022), pp. 435–442. ISSN: 20565135. DOI: 10.1595/205651322X16577001040526.
- [33] G.L. An et al. "A review on the solid sorption mechanism and kinetic models of metal halide-ammonia working pairs". In: *Renewable and Sustainable Energy Reviews* 91 (2018), pp. 783–792. ISSN: 1364-0321. DOI: <https://doi.org/10.1016/j.rser.2018.04.032>. URL: <https://www.sciencedirect.com/science/article/pii/S1364032118302648>.

- [34] Matthew J. Palys et al. "Modeling and Optimal Design of Absorbent Enhanced Ammonia Synthesis". In: *Processes* 6.7 (2018). ISSN: 2227-9717. DOI: 10.3390/pr6070091. URL: <https://www.mdpi.com/2227-9717/6/7/91>.
- [35] Hossein Asgharian et al. "Exceeding equilibrium limitations: Enhanced temperature control for sustainable decentralized green ammonia production - a techno-economic analysis". In: *Energy Conversion and Management* 315 (2024), p. 118764. ISSN: 0196-8904. DOI: <https://doi.org/10.1016/j.enconman.2024.118764>. URL: <https://www.sciencedirect.com/science/article/pii/S0196890424007052>.
- [36] Matthew J. Palys et al. "A novel system for ammonia-based sustainable energy and agriculture: Concept and design optimization". In: *Chemical Engineering and Processing - Process Intensification* 140 (2019), pp. 11–21. ISSN: 0255-2701. DOI: <https://doi.org/10.1016/j.cep.2019.04.005>. URL: <https://www.sciencedirect.com/science/article/pii/S0255270118314430>.
- [37] M.A. Kibria, D.E. McManus, and S. Bhattacharya. "Options for net zero emissions hydrogen from Victorian lignite. Part 2: Ammonia production". In: *International Journal of Hydrogen Energy* 48.95 (2023), pp. 37166–37182. ISSN: 0360-3199. DOI: <https://doi.org/10.1016/j.ijhydene.2023.06.098>. URL: <https://www.sciencedirect.com/science/article/pii/S0360319923029579>.
- [38] Md Burhan Kabir Suhan et al. "Optimal design of ammonia synthesis reactor for a process industry". In: *Journal of King Saud University - Engineering Sciences* 34 (1 Jan. 2022), pp. 23–30. ISSN: 10183639. DOI: 10.1016/j.jksues.2020.08.004.
- [39] Ali Dashti et al. "Modeling and simulation of ammonia synthesis reactor". In: *Petroleum & Coal* 48.2 (2006), pp. 15–23.
- [40] Louis J. Gillespie and James A. Beattie. "The thermodynamic treatment of chemical equilibria in systems composed of real gases. I. An approximate equation for the mass action function applied to the existing data on the haber equilibrium". In: *Physical Review* 36.4 (1930). Cited by: 56, 743 – 753. DOI: 10.1103/PhysRev.36.743. URL: <https://www.scopus.com/inward/record.uri?eid=2-s2.0-0342883667&doi=10.1103%2fPhysRev.36.743&partnerID=40&md5=a23e8d826f849f8d238903007e067751>.
- [41] D. C. Dyson and J. M. Simon. "Kinetic Expression with Diffusion Correction for Ammonia Synthesis on Industrial Catalyst". In: *Industrial & Engineering Chemistry Fundamentals* 7.4 (1968), pp. 605–610. DOI: 10.1021/i160028a013. eprint: <https://doi.org/10.1021/i160028a013>. URL: <https://doi.org/10.1021/i160028a013>.
- [42] Elizaveta Taranets and Line Flansmose Olsen. *CFD Modelling and Optimization of Ammonia Synthesis-Absorption Integrated Reactor Under Mild Conditions*. 2024. URL: [oai:pure.atira.dk:studentproject/cba69774-b017-4878-b667-5412f445933b](https://pure.atira.dk/studentproject/cba69774-b017-4878-b667-5412f445933b).
- [43] Tianbao Gu et al. "Exploring decentralized ammonia synthesis for hydrogen storage and transport: A comprehensive CFD investigation with experimental validation and parametric study". In: *Energy Conversion and Management* 295 (Nov. 2023). ISSN: 01968904. DOI: 10.1016/j.enconman.2023.117604.
- [44] A. Mirvakili et al. "Two-dimensional mathematical modeling of an industrial ammonia synthesis reactor with CFD analysis". In: *Journal of the Taiwan Institute of Chemical Engineers* 121 (Apr. 2021), pp. 1–19. ISSN: 18761070. DOI: 10.1016/j.jtice.2021.03.032.

- [45] Inc. Ansys. *Ansys Fluent Theory Guide, Release 2022 R1*. 2021.
- [46] HySTrAm. *HySTrAm*. URL: <https://www.hystram.eu/>.
- [47] H K Versteeg and W Malalasekera. *An Introduction to Computational Fluid Dynamics Second Edition*. URL: www.pearsoned.co.uk/versteeg.
- [48] FMI Project. *Functional Mock-up Interface (FMI) 3.0.1 Documentation — FMI for Model Exchange*. Accessed: 2025-04-12. 2024. URL: https://fmi-standard.org/docs/3.0.1/#_fmi_for_model_exchange_me.
- [49] MathWorks. *PEM Electrolysis System*. Accessed: 2025-04-25. 2024. URL: <https://se.mathworks.com/help/simscape/ug/pem-electrolysis-system.html>.
- [50] Sandip Dutta, Sirivatch Shimpalee, and J.W. Van Zee. "Numerical prediction of mass-exchange between cathode and anode channels in a PEM fuel cell". In: *International Journal of Heat and Mass Transfer* 44.11 (2001), pp. 2029–2042. ISSN: 0017-9310. DOI: [https://doi.org/10.1016/S0017-9310\(00\)00257-X](https://doi.org/10.1016/S0017-9310(00)00257-X). URL: <https://www.sciencedirect.com/science/article/pii/S001793100000257X>.
- [51] The University of Manchester. *Chemical Engineering Plant Cost Index (CEPCI)*. Accessed: 2025-04-29. 2025. URL: <https://www.training.itservices.manchester.ac.uk/public/gced/CEPCI.html?reactors/CEPCI/index.html>.
- [52] Subramani Krishnan et al. "Present and future cost of alkaline and PEM electrolyser stacks". In: *International Journal of Hydrogen Energy* 48.83 (2023), pp. 32313–32330. ISSN: 0360-3199. DOI: <https://doi.org/10.1016/j.ijhydene.2023.05.031>. URL: <https://www.sciencedirect.com/science/article/pii/S0360319923022590>.
- [53] T. Cholewa et al. "Reaction kinetics for ammonia synthesis using ruthenium and iron based catalysts under low temperature and pressure conditions". In: *Sustainable Energy Fuels* 8 (10 2024), pp. 2245–2255. DOI: 10.1039/D4SE00254G. URL: <http://dx.doi.org/10.1039/D4SE00254G>.
- [54] Dale E Seborg et al. *Process Dynamics and Control Fourth Edition*.
- [55] FuelPositive. *Green Ammonia System*. Accessed: 2025-03-06. n.d. URL: <https://fuelpositive.com/green-ammonia-system/>.
- [56] Eurostat. *Energy Statistics - Eurostat*. <https://ec.europa.eu/eurostat/statistics-explained/index.php?title=Category:Energy>. Accessed: 2025-04-29. 2025. URL: <https://ec.europa.eu/eurostat/statistics-explained/index.php?title=Category:Energy>.
- [57] Na Li, Samuel Simon Araya, and Søren Knudsen Kær. "Investigating low and high load cycling tests as accelerated stress tests for proton exchange membrane water electrolysis". In: *Electrochimica Acta* 370 (2021), p. 137748. ISSN: 0013-4686. DOI: <https://doi.org/10.1016/j.electacta.2021.137748>. URL: <https://www.sciencedirect.com/science/article/pii/S0013468621000372>.
- [58] Aleksandra Zamljen and Blaž Likozar. "Catalytic Reactor-Utilized Ammonia Adsorption, Absorption, and Storage Materials: Mechanism, Nanostructure, and Ab Initio Design". In: *ACS Sustainable Chemistry & Engineering* 12.48 (2024), pp. 17417–17436. DOI: 10.1021/acssuschemeng.4c06100. eprint: <https://doi.org/10.1021/acssuschemeng.4c06100>. URL: <https://doi.org/10.1021/acssuschemeng.4c06100>.

- [59] Ismail B. Celik et al. "Procedure for Estimation and Reporting of Uncertainty Due to Discretization in CFD Applications". In: *Journal of Fluids Engineering* 130.7 (July 2008), p. 078001. ISSN: 0098-2202. DOI: 10.1115/1.2960953. eprint: https://asmedigitalcollection.asme.org/fluidsengineering/article-pdf/130/7/078001/5491455/078001_1.pdf. URL: <https://doi.org/10.1115/1.2960953>.

Appendix A

Meshing and GCI

Meshing is a critical step for a CFD model, influencing the accuracy, stability, and computational efficiency of the simulation. For the geometry of the ammonia synthesis reactor used in this study, a structured hexahedral mesh was developed which can be seen on the Figure A.1.

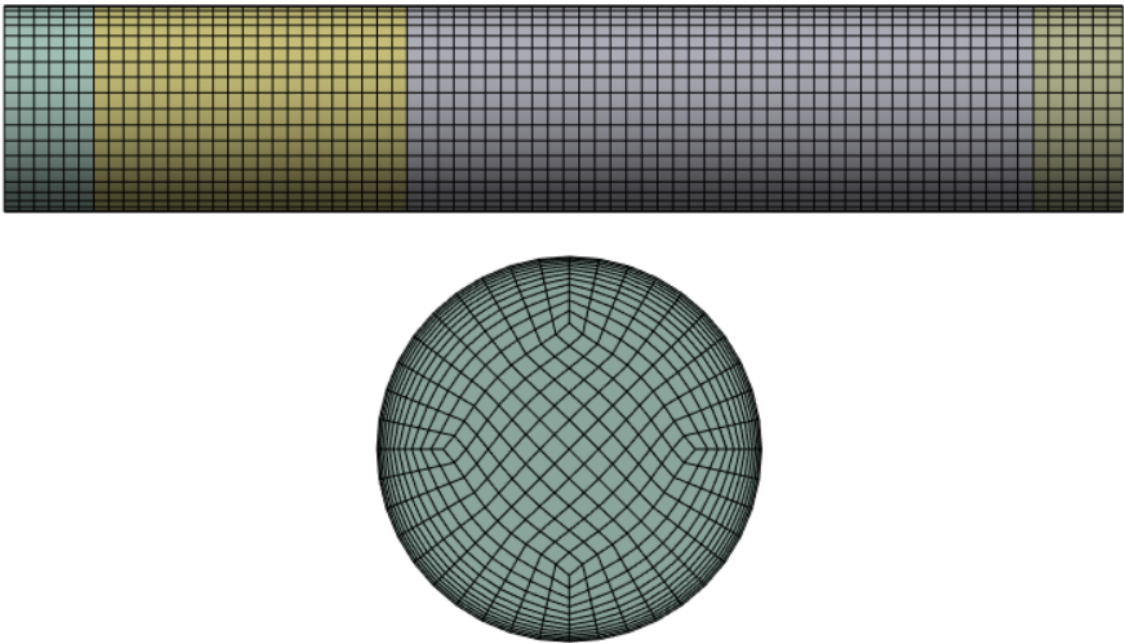


Figure A.1: Side and front views of the meshed reactor geometry

Three levels of mesh coarseness were generated, consisting of 14256, 42340, and 149688 elements, respectively. Table A.1 summarizes key mesh quality indicators including aspect ratio and skewness. All three meshes show acceptable average skewness values well below 0.5, and a decreasing average aspect ratio with finer meshes, indicating improved element quality [47].

Table A.1: Mesh Parameters

Parameter	Coarse Mesh	Medium Mesh	Fine Mesh
Elements	14256	42340	149688
Aspect ratio			
min	1.2333	1.3424	1.3761
max	29.167	17.5	10
average	9.8351	5.5127	3.0835
Skewness			
min	0.033806	0.012426	0.003864
max	0.41912	0.44404	0.46619
average	0.12468	0.094538	0.077315

To verify the mesh independence of the CFD results, a Grid Convergence Index (GCI) analysis was performed using the effective NH_3 production rate as the key variable ϕ . The mesh characteristic length h was estimated from the domain volume V and number of elements in the mesh N as Equation A.1 [59]:

$$h = \sqrt[3]{V_{\text{Domain}}/N} \quad (\text{A.1})$$

The solution differences between mesh levels were calculated as follows [59]:

$$\varepsilon_{cm} = \phi_{\text{coarse}} - \phi_{\text{medium}} \quad \varepsilon_{mf} = \phi_{\text{medium}} - \phi_{\text{fine}} \quad (\text{A.2})$$

Using these differences and the mesh refinement ratios $r_{cm} = h_{\text{coarse}}/h_{\text{medium}} > 1.3$ and $r_{mf} = h_{\text{medium}}/h_{\text{fine}} > 1.3$, the apparent order of convergence p was computed iteratively using Equation A.3 [59]:

$$p = \frac{1}{\ln(r_{mf})} \left| \ln \left| \frac{\varepsilon_{cm}}{\varepsilon_{mf}} \right| + \ln \left(\frac{r_{mf}^p - s}{r_{cm}^p - s} \right) \right| \quad (\text{A.3})$$

Here, $s = 1 \cdot \text{sign} \left(\frac{\varepsilon_{cm}}{\varepsilon_{mf}} \right)$ ensures consistency in error direction.

Based on the the calculated apparent order p , extrapolated solution estimates were determined as Equation A.4:

$$\phi_{mf}^{(ext)} = \frac{r_{mf}^p \phi_f - \phi_m}{r_{mf}^p - 1} \quad (\text{A.4})$$

The approximate relative error ($e_{mf}^{(a)}$) and extrapolated relative error ($e_{mf}^{(ext)}$) were calculated as Equations A.5:

$$e_{mf}^{(a)} = \left| \frac{\phi_f - \phi_m}{\phi_f} \right| \quad e_{mf}^{(ext)} = \left| \frac{\phi_{mf}^{(ext)} - \phi_f}{\phi_{mf}^{(ext)}} \right| \quad (\text{A.5})$$

Finally, the GCI parameter is calculated as Equation A.6:

$$GCI_{fine} = \frac{1.25 \cdot e_{mf}^{(a)}}{r_{mf}^p - 1} \quad (\text{A.6})$$

Figure A.2 illustrates the convergence of the effective NH_3 production rate with mesh refinement. The computed apparent order of convergence $p=5.03$ is well above the theoretical second-order accuracy typically expected for structured finite volume schemes, suggesting reliable convergence behaviour. The GCI values summarized in Table A.2 are 0.2471% for the medium mesh and 0.0297% for the fine mesh, both of which are below the threshold of 1%, indicating mesh-independent results. Given the good balance between accuracy and computational cost, the medium mesh (42340 elements) was used for all transient simulations throughout the study. The low GCI values and consistent extrapolated solution trends confirm that this choice maintains numerical accuracy while optimizing simulation time.

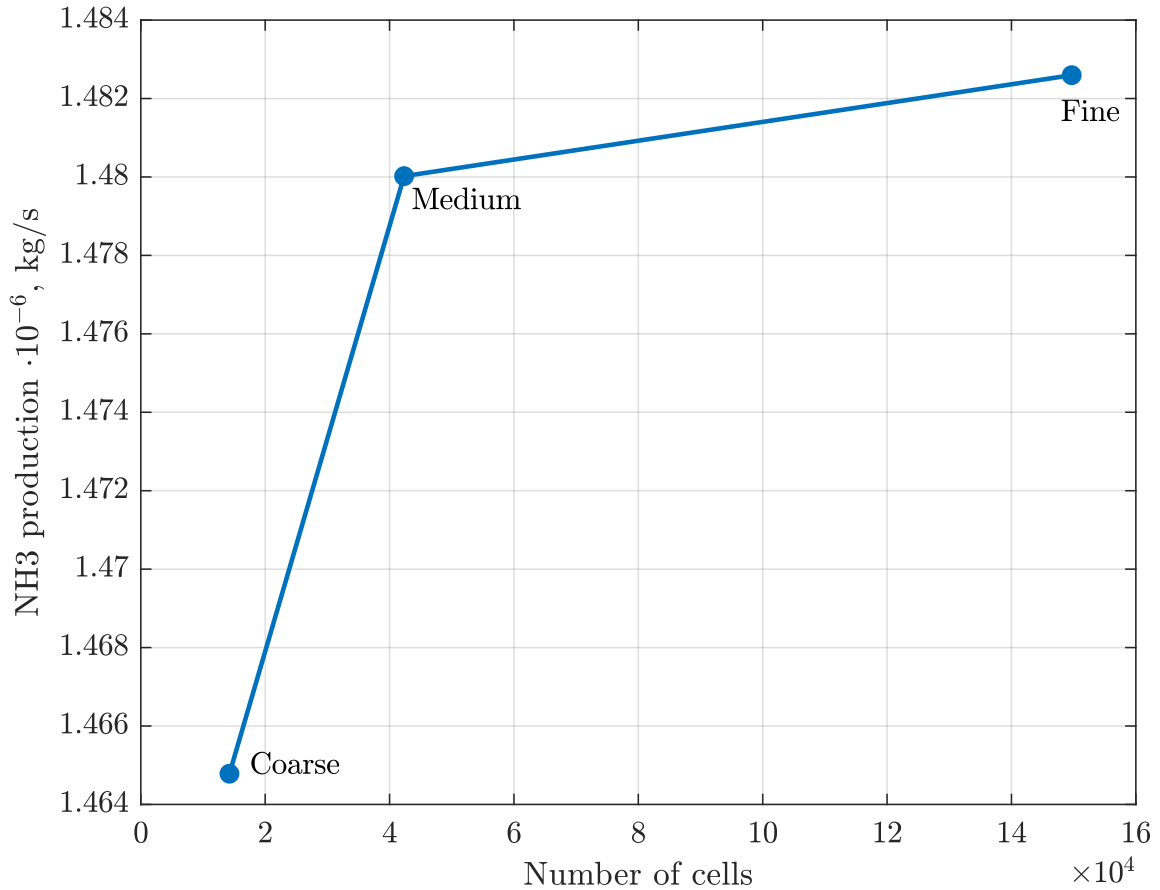


Figure A.2: Effective NH_3 production at a fixed time point as a function of number of cells in the mesh

Table A.2: Summary of GCI analysis for NH_3 production

Category	Parameter	Value
Mesh Size	Coarse mesh cells (N_c)	14256
	Medium mesh cells (N_m)	42340
	Fine mesh cells (N_f)	149688
Refinement Ratio	$r_{cm} = h_c/h_m$	1.4374
	$r_{mf} = h_m/h_f$	1.5234
Solution Values	ϕ_c (coarse) [kg/s]	$1.4648 \cdot 10^{-6}$
	ϕ_m (medium) [kg/s]	$1.4800 \cdot 10^{-6}$
	ϕ_f (fine) [kg/s]	$1.4826 \cdot 10^{-6}$
Extrapolated Solutions	$\phi_{cm}^{(ext)}$ [kg/s]	$3.1519 \cdot 10^{-7}$
	$\phi_{mf}^{(ext)}$ [kg/s]	$1.6019 \cdot 10^{-6}$
	Apparent order p	5.03
Relative Errors	$e_{cm}^{(a)}$	0.0103%
	$e_{cm}^{(ext)}$	$2.00 \cdot 10^{-3}\%$
	$e_{mf}^{(a)}$	0.0017%
	$e_{mf}^{(ext)}$	$2.37 \cdot 10^{-4}\%$
GCI	$\text{GCI}_{\text{medium}}$	0.2471%
	GCI_{fine}	0.0297%

Appendix B

User Defined Expressions in Ansys Fluent

```
1 "Absorbed_frac_NH3" "NH3Absorbed3/NH3produced"
2 "H2Conversion" "(MassAve(MassFraction(species = 'h2'),['inlet_body'])*
    MassFlow(['in'])) + MassAve(MassFraction(species = 'h2'),['outlet_body'])*
    MassFlow(['out']))/(MassAve(MassFraction(species = 'h2'),['inlet_body'])*
    MassFlow(['in']))"
3 "Ka" "10**(-2.691122 * log10(T*1[K^-1]) - 5.519265e-5 [K^-1] * T + 1.848863e
    -7 [K^-2] * T**2 + (2001.6 [K] / T) + 2.6899)"
4 "NH3Absorbed3" "-Sum(UserMassSource, ['absorption_bed'])"
5 "NH3produced" "NH3Absorbed3-MassAve(MassFraction(species = 'nh3'),['
    outlet_body'])*MassFlow(['out'])"
6 "P_NH3" "AbsolutePressure*1[kg^-1 m s^-2]/100000*MoleFraction(species = 'nh3')
    "
7 "P_atm" "(AbsolutePressure)/101325"
8 "P_eq1_SmithAbso" "1/(exp(42100/(R*1[J^-1 K mol]))*(1[K]/(T)-1/650)))**2"
9 "P_eq2_SmithAbso" "1/(exp(42100/(R*1[J^-1 K mol]))*(1 [K]/(T)-1/610)))**2"
10 "R_SmithAbso" "IF(MolarConcentration(species = 'nh3')*17.03061[kg kmol^-1]/dt
    >-1*R_SmithAbso_pre, R_SmithAbso_pre, -1*MolarConcentration(species = '
    nh3')*17.03061[kg kmol^-1]/dt)"
11 "R_SmithAbso_pre" "IF(MoleFraction(species = 'nh3')>0.001,-1[kg m^-3 s^-1]*(
    k_abs_1 + k_abs_2 + k_abs_3)*17.03061*600/60,0[kg m^-3 s^-1])"
12 "R_abs_heat" "-R_SmithAbso*46e6[J kmol^-1]/17.03061[kg kmol^-1]"
13 "S_H2" "2.01594 [kg kmol^-1]*r_H2"
14 "S_NH3" "17.03061 [kg kmol^-1]*r_NH3_transient"
15 "S_h" "r_NH3_transient*(46.22e6 [J/kmol])"
16 "Xa1" "IF(UDS(uds = 'uds-0')<0.13,UDS(uds = 'uds-0')/0.13, 1)"
17 "Xa2" "IF(UDS(uds = 'uds-1')<0.35,UDS(uds = 'uds-1')/0.35, 1)"
18 "Xa3" "IF(UDS(uds = 'uds-2')<0.35,UDS(uds = 'uds-2')/0.35, 1)"
19 "a_N2" "(0.93431737 + 0.3101804e-3[K^-1]*T + 0.29589610e-3 [Pa^-1]*P_atm -
    0.2707279e-6[K^-2]*T**2 + 0.4775207e-6 [Pa^-2]*P_atm**2)*P_atm*x_N2/1[Pa]
    "
20 "a_NH3" "(0.1438996 + 0.2028538e-2[K^-1]*T - 0.4487672e-3[Pa^-1]*P_atm -
    0.1142945e-5[K^-2]*T**2 + 0.2761216e-6[Pa^-2]*P_atm**2)*P_atm*x_NH3/1[Pa]
    "
21 "a_h2" "(exp(exp(-3.8402 [K^-0.125]*T**0.125 + 0.541)*1 [Pa^-1]*P_atm - (exp
    (-0.1263 [K^-0.5]*T**0.5-15.980))*1 [Pa^-2]*P_atm**2 + 300*exp(-0.01190 [
    K^-1]*T-5.941)*(exp(-P_atm/300 [Pa]))))*P_atm*x_H2/1[Pa]"
22 "k" "8.849*10**14* 1 [kmol m^-3 s^-1] * (1/3600)* exp(-170560 [K^-1] / (8.314
    * T))"
23 "k_abs_1" "3e-4*max(0,(P_NH3-0.05))*(1-Xa1)"
24 "k_abs_2" "2e-2*max(0,(P_NH3-P_eq1_SmithAbso))**4*(1-Xa2)**4"
25 "k_abs_3" "2.5e-2*max(0,(P_NH3-P_eq2_SmithAbso))**4*(1-Xa3)**6"
26 "r_H2" "-3*r_NH3_transient/2"
27 "r_NH3" "IF(MolarConcentration(species = 'h2') > 0.05 [kmol/m^3], max(0 [kmol
    m^-3 s^-1], 2*k* ((Ka**2 * a_N2 * (a_h2**3 / a_NH3**2)**0.5) - (a_NH3**2
    / a_h2**3)**(1-0.5))), 0 [kmol m^-3 s^-1])"
28 "r_NH3_transient" "IF(MolarConcentration(species = 'h2')/dt/1.5>r_NH3, r_NH3,
    MolarConcentration(species = 'h2')/dt/1.5)"
```

```

29 "r_abso1" "3e-4*max(0,(AbsolutePressure*1[kg^-1 m s^2]/100000*MoleFraction(
    species = 'nh3')-0.05))*(1-IF(UDS(uds = 'uds-0')<0.13,UDS(uds = 'uds-0')
    /0.13,1))/60*125.844*Density*1[s-1]"
30 "r_abso2" "2e-2*max(0,(AbsolutePressure*1[kg^-1 m s^2]/100000*MoleFraction(
    species = 'nh3')-P_eq1_SmithAbso))**4*(1-IF(UDS(uds = 'uds-1')<0.35,UDS(
    uds = 'uds-1')/0.35,1))**4/60*125.844*Density*1[s-1]"
31 "r_abso3" "2.5e-2*max(0,(AbsolutePressure*1[kg^-1 m s^2]/100000*MoleFraction(
    species = 'nh3')-P_eq2_SmithAbso))**4*(1-IF(UDS(uds = 'uds-2')<0.35,UDS(
    uds = 'uds-2')/0.35,1))**6/60*125.844*Density*1[s-1]"
32 "x_H2" "max(MoleFraction(species = 'h2'), 0.005)"
33 "x_N2" "max(MoleFraction(species = 'n2'), 0.005)"
34 "x_NH3" "max(MoleFraction(species = 'nh3'), 0.005)"

```